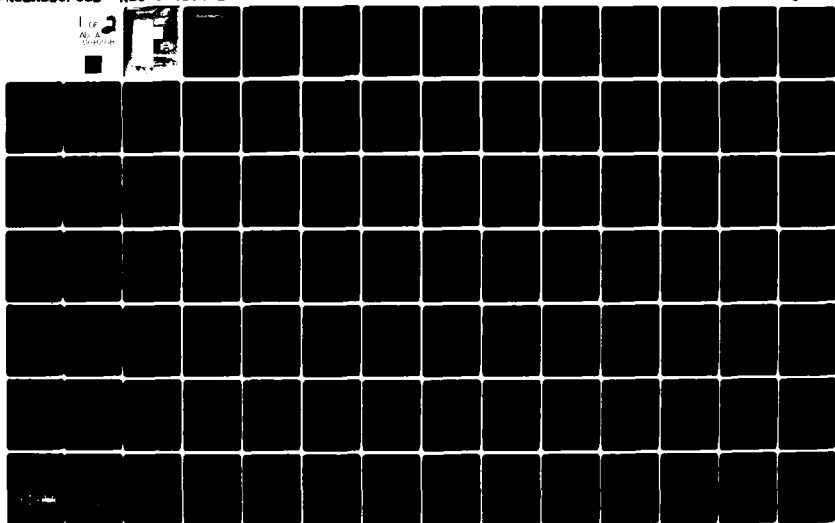


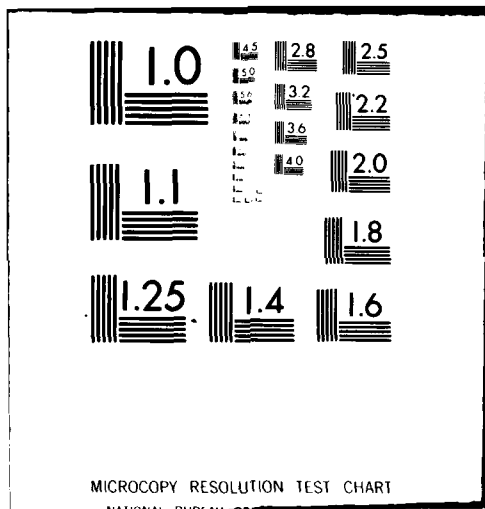
D-A088 208

UNITED TECHNOLOGIES RESEARCH CENTER EAST HARTFORD CONN F/6 13/8  
ANALYTICAL MODELING OF THE HOT ISOSTATIC PRESSING PROCESS. (U)  
JUL 80 B N CASSENTI, K J CHEVERTON F49620-78-C-0090  
R80-944374-13 AFOSR-TR-80-0592 NL

UNCLASSIFIED

1 Ce  
NL A  
DRAFT





# UNITED TECHNOLOGIES RESEARCH CENTER



East Hartford, Connecticut 06108

R80-944374-13

Analytical Modeling of the  
Hot Isostatic Pressing Process

Contract F49620-78-C-0090

REC'D  
SAC  
Aug 1 1980

A

REPORTED BY Brice N. Cassenti  
Brice N. Cassenti

APPROVED BY Allen F. Greiner  
Allen F. Greiner  
Assistant Manager of  
Engineering Operations

NO. OF PAGES \_\_\_\_\_

COPY NO. \_\_\_\_\_

Approved for public release;  
distribution unlimited.

the development of a constitutive model for powder metals. A model for powder metals subjected to an external hydrostatic pressure has been developed and compares well with experimental results. The exact form of the theory for a multi-axial stress state was determined by a series of mechanical tests. The constitutive model has been incorporated into the MARC\* nonlinear finite element computer program and analysis of an independent experiment using the modified code has been performed and verified the accuracy of the theory. Once the theory had been verified it was applied to the HIP of a disk and a sensitivity study was performed to determine an efficient modeling strategy. The results of the program are discussed in detail.

\*MARC Analysis Research Corporation

UNCLASSIFIED

## UNCLASSIFIED

SECURITY CLASSIFICATION OF THIS PAGE (When Data Entered)

REPORT DOCUMENTATION PAGE		READ INSTRUCTIONS BEFORE COMPLETING FORM
1. REPORT NUMBER <b>AFOSR TR-80-0592</b>	2. GOVT ACCESSION NO. <b>AD-A088 208</b>	3. RECIPIENT'S CATALOG NUMBER
4. TITLE (and Subtitle) ANALYTICAL MODELING OF THE HOT ISOSTATIC PRESSING PROCESS .		5. TYPE OF REPORT & PERIOD COVERED FINAL 15 July 1978 - 14 July 1980
7. AUTHOR(s) <b>BRICE N. CASSENTI</b>		6. PERFORMANCE DATA: REPORT NUMBER <b>R80-944374-13</b>
9. PERFORMING ORGANIZATION NAME AND ADDRESS UNITED TECHNOLOGIES CORPORATION UNITED TECHNOLOGIES RESEARCH CENTER EAST HARTFORD, CT 06108		10. PROGRAM ELEMENT, PROJECT, TASK AREA & WORK UNIT NUMBERS <b>2307B2 61102F</b>
11. CONTROLLING OFFICE NAME AND ADDRESS AIR FORCE OFFICE OF SCIENTIFIC RESEARCH/NA BLDG 410 BOLLING AIR FORCE BASE, DC 20332		12. REPORT DATE <b>July 1980</b>
14. MONITORING AGENCY NAME & ADDRESS (if different from Controlling Office)		13. NUMBER OF PAGES <b>134</b>
		15. SECURITY CLASS. (of this report) <b>UNCLASSIFIED</b>
		15a. DECLASSIFICATION/DOWNGRADING SCHEDULE
16. DISTRIBUTION STATEMENT (of this Report) Approved for public release; distribution unlimited		
17. DISTRIBUTION STATEMENT (of the abstract entered in Block 20, if different from Report)		
18. SUPPLEMENTARY NOTES		
19. KEY WORDS (Continue on reverse side if necessary and identify by block number) HOT ISOSTATIC PRESSING NONVOLUME PRESERVING PLASTICITY CREEP FINITE ELEMENTS		
20. ABSTRACT (Continue on reverse side if necessary and identify by block number) This report describes the results of a two-year investigation to develop a modeling strategy to predict the final shape of components manufactured by the Hot Isostatic Pressing (HIP) process. When a powder metal is subjected to the high pressures at high temperatures there is a permanent reduction in the macroscopic volume by approximately 30 percent. The volume reduction, which is not included in classical creep and plasticity theories, necessitates the modification of the classical theories. The major part of this report concerns		

R80-944374-13

## FOREWORD

The final report has been prepared for the Air Force Office of Scientific Research, United States Air Force, Contract F49620-78-C-0090 with Lt. Col. J. D. Morgan as the program monitor. The program manager for UTRC is Mr. A. F. Greiner. The principal investigators were Dr. K. J. Cheverton from 15 July 1978 to 1 January 1979, and Dr. B. N. Cassenti from 2 January 1979 to 14 July 1980.

Accession No.	
NAME	John D.
PLATE NO.	1
DATE RECEIVED	1968-10-10
DATE ISSUED	1968-10-10
RECEIVED BY	John D.
ISSUED BY	John D.
APPROVED BY	John D.
PART	1
A	

AIR FORCE OFFICE OF SCIENTIFIC RESEARCH (AFSC)  
NOTICE OF APPROVAL TO DDC  
This technical report has been reviewed and is  
approved for public release under AFN 190-12 (7b).  
Distribution is unlimited.  
A. D. BLOSE  
Technical Information Officer

R80-944374-13

Analytical Modeling of the  
Hot Isostatic Pressing Process

TABLE OF CONTENTS

	<u>Page</u>
SUMMARY . . . . .	1
RESULTS . . . . .	2
INTRODUCTION . . . . .	3
PROGRAM PLAN . . . . .	6
CONSTITUTIVE THEORY DEVELOPMENT . . . . .	11
Yield Surface Considerations. . . . .	13
Choice of Hardening Parameters. . . . .	17
Large Strain Flow Rule Considerations . . . . .	23
Time Dependent Deformation. . . . .	24
Microstructural Modeling to Develop Macroscopic Constitutive Laws .	28
CODE MODIFICATIONS. . . . .	33
General Considerations. . . . .	33
Plastic Iteration Procedure . . . . .	34
Time Effects Iteration Procedure. . . . .	37
Code Selection, Installation, and Testing . . . . .	38
Code Modifications. . . . .	39
MATERIAL PROPERTY DETERMINATION . . . . .	41
Partial HIP Tests . . . . .	41
Mechanical Tests. . . . .	44
Interpretation of Mechanical Test Results . . . . .	46

TABLE OF CONTENTS (Cont'd)

	<u>Page</u>
MODEL VERIFICATION. . . . .	52
Verification Criteria . . . . .	52
Spherical Inclusions. . . . .	52
Cylindrical Inclusions. . . . .	53
Yield Surface Considerations. . . . .	54
Plastic Analysis for Spherical Inclusions . . . . .	54
Verification Experiment Results . . . . .	54
HIP PROCESS SENSITIVITY STUDIES . . . . .	56
REFERENCES. . . . .	60
APPENDIX A - HARDENING PARAMETERS . . . . .	63
TABLES 1 THROUGH 8. . . . .	68
FIGURES 1 THROUGH 51. . . . .	76

R80-944374-13

Analytical Modeling of the  
Hot Isostatic Pressing Process

SUMMARY

A program to develop a finite element methodology for predicting the final shape of components manufactured by the Hot Isostatic Pressing (HIP) process has been conducted for the Air Force Office of Scientific Research. The major task in the program was the development of a constitutive model for compacting metal powders. The constitutive model extends classical plasticity and creep theories to include the large decrease in volume resulting from the HIP process. The constitutive model was added to the MARC\* finite element code and parameters required by the model were determined experimentally. The modified code was used to predict the results of a verification experiment and then applied to the prediction of the final shape of hot isostatic pressed components.

During the course of the program, several significant results were obtained. Plasticity and creep theories have been extended to include volumetric plastic deformations in order to satisfy the requirements applicable to the HIP process. The MARC code was modified to include the constitutive theory developed. Partially dense specimens were fabricated for the mechanical tests and analytical expressions relating final density to pressure, temperature and time for a HIP cycle are in good agreement with the experimental results. Mechanical test results indicated there was little volume change during compression testing, and the tension yield stress was significantly less than the compression yield stress. From the mechanical tests analytical expressions were developed relating the tension and compression yield stress to density and temperature. Analytical expressions were also developed describing the deviatoric, or volume preserving, creep strain components. An independent verification experiment was performed and the results of the experiment compared favorably with the numerical predictions using the modified finite element code. A parametric study using the modified code indicated the following effects should be included in modeling the HIP process: (1) all large strain effects except the unsymmetric stiffness term, (2) temperature gradients, and (3) deviatoric creep. Weight loadings should be included in long unsupported components and volumetric creep should be included in low external pressure, long time HIP of components. The effects of work hardening and the unsymmetric stiffness terms do not need to be included. At the point where the disk HIP analyses were terminated the comparison with the measured experimental results was good. The analysis was able to capture all of the characteristics of the disk HIP.

## RESULTS

The feasibility of modeling the shape of hot isostatic pressed components has been demonstrated as a result of this program. However, during the course of the program, several other significant results were obtained:

(1) A constitutive theory which includes the large volume reductions, approximately 30 percent, that result from the HIP process, has been developed. The theory extends classical, volume preserving, plasticity and creep theories, to include large volumetric deformations.

(2) The MARC code was modified to include the plasticity and creep theories developed in Task 1. The MARC code was selected for use in the program based on the results of the assessment of several finite element codes. Simple analytical tests verified the modifications.

(3) Analytical expressions have been developed to predict the powder density as a function of pressure, temperature and time and are in good agreement with the experimental results from partially dense test specimens fabricated from MERL 76.

(4) Compression test results indicated that there was little or no volume change occurring during compression testing. Tension testing resulted in very low values for the tension yield stress. This may be due to the presence of voids and the incomplete bonding at the metal powder particle interfaces. Additional testing indicated there was little or no contamination present that would produce low tension yield stresses. Simple analytical expressions were developed for the tension and compression yield stresses and agreed well with the experimental results.

(5) An independent verification experiment was designed and analyzed using the modified code. The experimental and analytical results were in agreement.

(6) A parametric study was performed to determine the relative importance of various modeling parameters in the HIP of components. An actual disk HIP was modeled and the results compared well with observations resulting from the HIP. The numerical model predicted a difference in the axial and radial contractions which was within 8 percent of the experimentally measured value.

## INTRODUCTION

The technology for fabrication of nickel base superalloy turbine engine components by powder metallurgy (PM) methods has advanced rapidly during the past five (5) years. The strong emphasis on PM is the result of advanced engine technology requirements for higher performance alloys which are more difficult to process (cast, forge) and hence, result in higher costs. Advanced PM technology for the production of near net shapes in superalloys offers the two-fold advantage of producing complex engine components from the most advanced alloys without the need for either castability or workability in the alloy and doing so at significantly lower cost than current technology. An Air Force Materials Laboratory's program, described in Ref. 1, has demonstrated the viability of the Hot Isostatic Pressing (HIP) process for the production of a complex turbine disk-shaft to near net shape at significant cost reduction when compared with the current method of production. For nickel-base turbine disks, with integral bolt flanges, over 60 percent of the final component cost is incurred in metal removal operations. Further, nearly 20 percent of the part cost is involved in procurement of raw material, as little as 10 percent of which ends up in the finished machined part. Thus, by improving the buy-to-fly ratio from 10 to 1 to 5 to 1, it is possible to save nearly 40 percent on component fabrication costs.

A substantial economic advantage for powder metallurgy materials can be achieved by direct hot isostatic pressing of components to near finished dimensions. The HIP of components to near finished dimensions would minimize the cost of machining, and save critical materials. The concept of HIP complex near-net shapes is simple. As is shown schematically in Figs. 1 and 2, a mold having the required configuration is filled with powder. The mold or container, is outgassed, sealed, placed in a HIP facility, raised to a temperature of over 2000 F and subjected to an external gas pressure of approximately 15,000 psi.

During the HIP process the volume occupied by the powder decreases by 30 to 35 percent. The rate of powder compaction occurs as a result of surface tension forces and plastic deformation and is a function of temperature and pressure. Ideally this shrinkage is isotropic, so that the final shape is a uniformly reduced replica of the initial container shape. In practice, the final shape can depart substantially from that ideal shape depending upon the techniques practiced. Because of this distortion and a current absence of systematically derived analytical tools to predict it, the full benefit of the HIP process has not been realized. Rather, HIP containers are fabricated larger than necessary to accommodate this distortion.

Many factors contribute to HIP distortion. Some arise from imperfect execution of steps in the HIP process such as nonuniform filling of the container, thin spots

in container material and incomplete outgassing of the container. The present discussion assumes a perfect fabrication process and is concerned with distortions intrinsic to the HIP process.

To determine the load transferred from the HIP container to the powder a constitutive model of the powder is required. This model should include irreversible compression and shear strength growth as functions of pressure, temperature and time. Volume reductions of 30 percent to 35 percent imply changes in linear dimensions of the container in excess of 10 percent. This in turn implies that the powder and container both experience large strains and displacements. Present research is based on an empirical approach and does not fully address these issues. To adequately model the HIP process a large-strain finite element analysis code possessing experimentally verified constitutive models for the container and the powder is needed.

The objective of this program was to develop a finite element methodology for predicting final size and shape of hot isostatically pressed axisymmetric powder metal structures. A constitutive model for the compaction of metal powders during the HIP process has been constructed and an experimental program was executed to provide data for and testing of this model. An existing nonlinear finite element code which models both container and powder deformations during the HIP operation has also been modified. This code was verified by comparing its predictions with the results obtained from a specially designed HIP experiment. Constitutive theory development for the container was modeled using standard elastic-plastic and creep theories. The material properties for the container material were developed under separate funding, and are described in Ref. 2. More specifically, the program consisted of the following five tasks:

- (1) Constitutive Model Development - The development of a finite strain elastic-plastic-creep model of metal powders compacting under the action of high temperature and pressure. The plasticity and creep theories are used to predict irreversible volume shrinkage for the powder.
- (2) Code Modifications - The modification of an existing finite element code to incorporate the developed constitutive model.
- (3) Material Property Determination - Metal powder filled glass containers have been subjected to HIP and powder densification determined as a function of pressure, temperature and time. Test specimens were fabricated from the samples and mechanical tests have been performed to determine the stress-strain behavior of partial dense HIP powders.

- (4) Verification Study - A partial HIP experiment has been designed and executed. The experiment was simulated using the modified code and the results compared well with those of the experiments.
- (5) HIP Process Sensitivities Studies - A disk previously subjected to HIP was selected and the associated HIP process was simulated using the modified code. In addition, the sensitivity of the predicted shrinkage to the analysis procedure has been determined and an efficient analysis methodology defined.

The following section discusses in detail the program plan. Each of the above five tasks are then discussed in the next five sections.

## PROGRAM PLAN

The objective of this program was to develop a finite element methodology for predicting the final size and shape of hot isostatically pressed axisymmetric powder metal structures. There are five main tasks, each of which is discussed in detail below.

Task 1: Constitutive Model Development

In this task a constitutive model which characterizes densification and deformation of metal powders during the HIP process was developed through the execution of the following subtasks.

Task 1.1 Yield Surface Determination

A yield surface for compacting metal powders must be developed. Existing yield surface functions were compared on the basis of their ability to model experimental data. A closed smooth yield surface which is quadratic in stress was selected. More general forms of the yield surface functions were not considered necessary since limited experimental data was developed and employed in the evaluation of candidate yield surfaces. The yield surface

$$\beta \left( \frac{I_1 + \alpha}{3} \right)^2 + J_2 = \sigma_o^2 / 3$$

was chosen. This yield surface admits unequal yielding in tension and compression through the use of the variable  $\alpha$ . The parameters in the yield surface were evaluated by fitting the function to results obtained from both the partial HIP experiments and the mechanical tests.

In the above equation,  $\alpha$ ,  $\beta$  and  $\sigma_o$  are functions of void volume fraction, plastic work, temperature and time.

Task 1.2.1 Deformation dependent hardening

Hardening was characterized by powder void volume fraction and plastic work performed. Hardening parameters were characterized as a function of HIP pressure and temperature by measuring the volume reduction of partial HIP test specimens. A large strain, finite element, elastic-plastic analysis of a microstructural model was performed to assess the usefulness of finite element idealizations of such microstructural compaction process models. Pressure versus volume shrinkage curves were obtained from the finite element analyses and compared with partial HIP experiments. Yielding of a partially compacted powder in

hydrostatic compression was assumed to follow experimentally derived pressure versus densification curves. The influence of volume shrinkage on yield stress in compression was determined from the mechanical tests.

Task 1.2.2 Time dependent hardening

The time dependent hardening of the yield surface was determined from the mechanical testing of specimens fabricated from partially densified HIP powder. For example, if  $\bar{\sigma}$  is a specimen yield strength in uniaxial tension, then for the yield surface assumed in Task 1.1

$$\sigma_o = \bar{\sigma} \sqrt{(1 + \beta^2/3)(1+\alpha/\bar{\sigma})}$$

The time dependence of  $\sigma_o$  was determined from the mechanical tests of specimens fabricated from partial HIP samples.

Task 1.3 Flow Rule Development

A HIP process large strain elastic-plastic flow theory was developed to relate increments of stress and strain. An associated flow rule based on the yield surface developed in Tasks 1.1 and 1.2 was used. The flow rule relates the Jaumann rate of Cauchy stress to the symmetric part of the velocity gradient.

Task 1.4 Creep Effects

A constitutive theory encompassing creep effects was developed and employed to evaluate the hypothesis that the dominant HIP process deformation mechanism is plastic flow.

Creep deformation was separated into volumetric and deviatoric components and laws for the components developed. The volumetric creep was assumed to follow a power law model fo the form

$$D_{kk}^c = -Ap^m$$

where  $D_{kk}^c$  is volumetric creep shrinkage rate,  $p$  is HIP pressure, and  $A$ , and  $m$  are the usual temperature dependent, power law parameters. The results of the partial HIP tests were used to assign numerical values to  $A$  and  $m$ . Although the HIP tests are not carried out at uniform temperature and pressure, volumetric

creep shrinkage rate can be computed from the results of fabricating partially dense HIP specimens subjected to the same maximum temperature and pressure for different lengths of times.

The deviatoric creep strains were modeled using a law of the form

$$\hat{D}_{ij}^c = \frac{3}{2} \frac{\hat{D}^c}{\sigma} S_{ij}$$

where the terms are defined in the section on Time Dependent Deformation. To develop material properties for this creep model a uniaxial law of the form

$$\hat{D}^c = B \sigma^{-k} t^m$$

was assumed. The temperature dependent constants can be evaluated from uniaxial creep data.

#### Task 2: Code Modifications

The HIP process constitutive theory must be incorporated into an existing finite element code. An upgraded level H-4 of the MARC nonlinear finite element code was employed. This level provides large strain finite element elastic-plastic and creep analysis capability using an updated Lagrangian formulation. Capabilities of the code which were used in this program are (1) large strain, updated Lagrangian formulation, (2) elastic-plastic and creep constitutive theories, (3) nonlinear boundary conditions, and (4) axisymmetric solid and shell elements. The axisymmetric solid elements are used to model the powder and the shell elements are used to model the container. The MARC code is constructed such that the constitutive theory is independent of element formulations. Thus, the element library in MARC does not require modification. The updated Lagrangian formulation provides the framework for computing all terms in the incremental stiffness matrices. Thus, the only portions of MARC that must be modified are:

- (1) The yield function
- (2) The incremental stress-strain calculations
- (3) The pseudo force load vector for creep analyses
- (4) The incremental strain calculations
- (5) The plasticity hardening rules
- (6) The routines which print stresses and strains.

The code modifications were verified by the analysis of simple one element test problems.

Task 3: Material Property Determination

The constitutive parameters must be evaluated through a series of HIP experiments and mechanical tests. Specifically the shape and expansion of the powder yield surface and the creep law parameters were determined as functions of HIP pressure, temperature and time. The experimental program consisted of two subtasks. In the first subtask samples of metal powder were subjected to partial HIP cycles. In the second subtask mechanical tests were performed on specimens fabricated from partially dense HIP powder samples. The experimental program used only one type and initial density of metal powder: that corresponding to the powder used in the HIP disk modeled in Task 5.

Task 3.1 Partial HIP Experiments

A matrix of partial HIP experiments was executed to determine plastic and creep volumetric strains as functions of HIP pressure, temperature and time. The experimental samples were cylindrical powder filled glass containers. Several HIP cycles were considered and the resulting powder densification measured.

Task 3.2 Mechanical Tests

Mechanical tests were conducted to determine the plasticity parameters identified in Task 1. Partially dense HIP samples were removed from the furnace and machined into specimens. Two types of tests were performed:

- (1) Compression tests were performed at the HIP temperature to identify one point on the yield surface and to examine plastic, hardening elastic, and relaxation response.
- (2) Tension tests were performed at HIP temperature to determine the symmetry of the yield surface.

Task 4: Constitutive Theory Verification

The constitutive model developed in Task 1 must be experimentally validated. Tests were designed and conducted to investigate regions of the theory not explored by the mechanical tests performed in Task 3. This investigation was accomplished by designing and considering two candidate tests. These candidate tests included spherical and cylindrical inclusions in a powder metal. One of the candidate tests was modeled numerically using the modified code of

Task 2. The results of the numerical modeling were examined to determine the most appropriate candidate test or tests. Several specimens were manufactured and tested. Only glass containers were used since they have negligible strength at HIP temperatures. The results of the tests were compared to the numerical results.

Task 5: HIP Process Sensitivity Study

A study must be conducted to assess the sensitivity of the HIP process constitutive and numerical models to parameter values and numerical techniques. A HIP geometry was selected for which documented initial and final dimensions exist, and an analysis performed. Finite element analysis of a simple geometry was performed to assess the affects of the following:

- (1) Inclusion of powder creep deformations
- (2) The assumption that rotations and deviatoric strains in the powder are small relative to volumetric strains
- (3) Temperature gradients in the powder
- (4) Pressure, temperature and time increment sizes and increment convergence criteria
- (5) The influence of various parameters.

Two finite element breakups of the disk were generated. The first breakup was relatively simple but sufficient to model overall container and powder response. Local deformations caused by container corners and container-powder interactions cannot be included in this model. Only variable (2) of the previous list are strongly dependent on container and powder interactions. The effects of the remaining variables were investigated independently using the simple finite element model and recommendations for the efficient modeling of the HIP process were made.

The second finite element breakup was more detailed and was used to investigate interactions between the powder and the container. The contributions of large rotations and shear strains to final predicted shape of the HIP container were investigated.

In Table 1 each of the tasks and subtasks are summarized.

The following sections describe in detail the results for each of the Tasks 1 through 5.

## CONSTITUTIVE THEORY DEVELOPMENT

Hot isostatic pressing (HIP) of metal powders is a complex process wherein the loose aggregate of metal powder particles is compacted into a coherent mass by the application of temperature and pressure. To achieve a specific shape a glass or metal container resembling the shape of the component to be manufactured is fabricated and filled with metal powder. The filled container is first vibrated to increase powder bulk density and is then evacuated and sealed. After heating in a preheat oven at approximately 2000 F, the container is transferred to a HIP furnace and is subjected to a pressure-temperature cycle. For nickel base superalloys temperature and pressure typically range up to 2200 F and 15,000 psi, respectively.

The HIP process performs two functions: (1) densification of the loose powder metal aggregate and (2) endowment of the densified powder with mechanical strength. The process by which this occurs can be described microstructurally as passing through the several stages (Refs. 3, 4, and 5):

- (1) Particle rearrangement, fragmentation and plastic flow
- (2) Formation of isolated pores
- (3) Sphericalization of the isolated pores
- (4) Closure of the spherical pores

Driving forces for these stages are the applied external HIP pressure and particle surface free energy of which the former is typically much larger. Although the mechanisms which are active during these stages of the process are not fully understood, it is generally accepted that the principle mechanisms are

- (1) Plastic deformation
- (2) Volume diffusion or Nabarro-Herring creep
- (3) Grain boundary diffusion or Coble creep
- (4) Power law or dislocation creep.

Recently Ashby (Ref. 6) developed the concept of deformation mechanism maps as a tool for delineating (1) regions in stress-temperature space where one or more of these mechanisms dominates and (2) regions where more than one mechanism is active. These maps have been applied by several authors (Refs. 3, 4, and 7) to the HIP process in an attempt to identify active mechanisms. The geometric model on which these studies are based is a hollow spherical shell of inner and outer radius  $R_1$  and  $R_2$ , respectively. The inner radius,  $R_1$ , is that of a typical isolated spherical pore and  $R_2$  is such that the density of the metal shell material averaged

over the shell and pore equals the macroscopically measured density of the partially densified powder. Wilkinson and Ashby (Ref. 3) using Torre's model (Ref. 8) and Green (Ref. 9) have considered the shrinkage of perfectly plastic hollow spheres subject to an external pressure as a means of gauging the effect of plastic deformation on densification. If  $P$  and  $\sigma_y$  are the applied external pressure and the at temperature yield strength of the powder, then the residual void fraction after plastic deformation will be equal to

$$v = \exp(-3P/2\sigma_y) \quad (1)$$

where

$$v = 1 - \rho_v/\rho_{solid} \quad (2)$$

$\rho_v$  is the density of the aggregate after plastic densification, and  $\rho_{solid}$  is the density of the fully compacted powder. At high temperatures (e.g., 2000 deg F) and 15,000 psi, HIP pressure can be up to three times greater than  $\sigma_y$  in which case  $v$ , from Eq. (1) is less than one percent. Although this analysis is appropriate for only powder aggregates with isolated pores (i.e., powders in the final state of compaction) it does indicate the possibility that much of the compaction process can be characterized using plasticity theory.

Two approaches to modeling powder deformation and strength growth in the HIP process are possible. The first is based on continuum mechanics principles wherein microstructural effects are averaged over the powder aggregate. The second approach is to consider microstructural processes explicitly. Since the objective of this program is to predict overall powder response in the HIP process, the latter approach is not sufficient by itself. Rather, it may be used to aid development of continuum constitutive models by supplementing experimental work.

The development of continuum constitutive models requires consideration of large strain effects since the initial void fraction is approximately 30 percent. This in turn implies that a 30 percent volume reduction is necessary to obtain full powder densification. Both time independent and time dependent models must be considered, though based upon the above equations, time independent plasticity effects can be expected to dominate. A finite strain plasticity theory requires: (1) specification of a yield surface to delineate regions of elastic and plastic response, (2) a hardening rule for the expansion of this yield surface and (3) a flow rule for relating stress and strain increments. This flow rule must be formulated using large strain, stress and strain rate measures. Time effects require the specification of a creep law.

### Yield Surface Considerations

In this section yield surface concepts pertinent to powder metals are discussed. Since, a priori, powder metals might be thought similar to soil like materials, soil mechanics yield surface theory is reviewed and the shortcomings identified. Next the requirements for compacting powder metal yield surfaces are discussed and previously published yield surfaces are reviewed. Last, the yield surface forms to be used are presented, and discussed in detail.

The metal powder is initially packed as a cohesionless granular material. The HIP container is evacuated, brought to a moderately high temperature and maintained at this temperature. Although some sintering by surface diffusion may occur at this point, the rates will generally be low, due to the initially small contact area between particles. Since the material is granular with no fluid phase, it is reasonable to expect that the Mohr-Coulomb type yield surfaces from soil and rock mechanics might be relevant to the incipient deformation. Figure 3 shows a cross section of the linear Mohr-Coulomb yield surface for a cohesionless material.

The yield surface is defined by the yield function

$$f(\sigma_{ij}) = \beta I_1 + \sqrt{J_2} - \sigma_o/\sqrt{3} = 0 \quad (3)$$

where  $I_1$  is the first stress invariant or three times the mean Cauchy stress  $\sigma_{kk}/3$  and  $\sigma_o$  is the yield stress. Also

$$J_2 = 1/2 S_{ij} S_{ij} \quad (4)$$

is the second invariant of the deviatoric stress  $S_{ij}$  defined by

$$S_{ij} = \sigma_{ij} - I_1 \delta_{ij}/3 \quad (5)$$

$\delta_{ij}$  being the usual Kronecker delta symbol. Note that when  $\beta$  is zero Eq. (3) reduces to the usual yield surface definition of metal plasticity

$$J_2 = \sigma_o^2/3 \quad (6)$$

In Eq. (3), it is assumed that the material is isotropic and flows at a Mises equivalent shear stress which is linearly dependent on mean stress. The linearity of this dependence is not a necessary feature of such pressure sensitive yield conditions, but is rather a mathematical convenience generally consistent with observations. More general relations, such as the parabolic Mohr-Coulomb model,

$$J_2 + \beta \frac{\sigma_0}{\sqrt{3}} I_1 - \sigma_0^2 / \sqrt{3} = 0 \quad (7)$$

can also be considered. For Mohr-Coulomb materials, admissible stress states are those on or within the region to the left of the yield surface curve (see Fig. 3). Within this region, the frictional forces between particles are sufficient to suppress large macroscopic deformations due to particle rearrangement; further, the macroscopic response is taken to be linear elastic. Of course, the elastic moduli governing deformation within this region are not those of the material matrix, but are suitably reduced due to the presence of interparticle void space.

At some fixed mean stress, as  $J_2$  is increased to its yield value, the frictional forces can no longer prevent particles from sliding over each other. Permanent macroscopic shape changes then occur as particles ride over one another and establish new contacts with adjacent particles. For soil like materials it is experimentally observed that this new configuration is not as densely packed as the initial state, and some volume increase is observed. This particle rearrangement occurs rapidly enough that the deformation can be idealized as instantaneous plasticity. An important feature of plastic deformation accommodated by frictional processes is illustrated schematically in Fig. 3. That is, the plastic strain vector,  $E^P$  in Fig. 3, is generally nonassociative: it is not expressible as the gradient with respect to stress,  $N$  in Fig. 3, of the yield function. A consequence of such non-normal flow rules is that the incremental stress-strain matrix is non-symmetric as shown in Appendix A of Ref. 10.

In summary, the effect of standard Mohr-Coulomb type yield surface is to (1) close the yield surface in principal stress space along the positive hydrostatic direction and (2) to predict volumetric plastic expansion as shown in Appendix B of Ref. 10. While this is clearly a proper material limitation to impose for soils, it is a limitation which is not encountered during the HIP process. This is because material points experience a monotonic increase in hydrostatic pressure, corresponding to leftward movement along the  $I_1$  axis in Fig. 3, followed by a period of constant pressure, and then depressurization. For such a load history, Mohr-Coulomb theory predicts no inelastic volume change. But, in fact, inelastic behavior is macroscopically observed as pressure is increased. A new mechanism of plastic deformation takes place due to dislocation motion within the particles. That dislocation motion should occur within the particles is not surprising, since the micro-stress distribution within particles is highly nonuniform due to uneven traction distributions at interparticle contacts.

Once particles begin to deform due to contact loading, it can be expected that many additional deformation mechanisms may be operative as well. For example, some particles may break free of the restraining frictional forces and reorient themselves, but when averaged over volumes containing many particles, the macroscopic deformation corresponding to a macroscopic hydrostatic pressure would be a uniform volumetric decrease. Indeed, any deviatoric deformation arising from a spherically symmetric stress state would be in conflict with the presumed macroscopic isotropy of the metal powder.

Thus, to use a Mohr-Coulomb type theory to model the HIP process, the yield surface must be modified to admit (1) yield in compression and (2) permanent volumetric shrinkage. This can be achieved by closing the yield surface along the negative hydrostatic axis as in Fig. 4. Such an approach has been adopted by Suh (Ref. 11) starting from a linear Mohr-Coulomb yield condition.

Another approach is to postulate the definition of a yield surface based on heuristic arguments. Since powder particle orientation is random, the powder aggregate should initially respond isotropically. Thus the yield function must also be an isotropic function and depend on only the stress through its invariants. Also, yielding must occur under hydrostatic pressure and that the yield function must approach that of a metal as densification progresses. Since invariant  $I_1$  is a linear multiple of the hydrostatic component of stress, and yield surfaces for metals are usually defined in terms of invariant  $J_2$ , a convenient form for the yield surface is

$$f = f(I_1, J_2, h_\alpha) = 0 \quad (8)$$

Further, since all first and second order invariants of stress are expressible in terms of  $I_1$ , and  $J_2$ , and the third invariants of  $\sigma_{ij}$  and  $s_{ij}$  have no physical interpretation, Eq. (8) appears quite general. The parameters  $h_\alpha$  depend on the deformations, and represent, for example,  $\alpha$ ,  $\beta$  and  $\sigma_0$  in Eq. (3).

The yield surface in stress space should also be initially closed and then tend to an open ended cylinder about the hydrostatic axis as the powder compacts and sinters. Yielding in hydrostatic compression is clearly needed to model the HIP process. Further yielding in hydrostatic tension is also to be expected since a partial HIP specimen resembles a metal with voids and, as shown by Needleman (Ref. 12), hydrostatic yield dependence permits macroscopic modeling of void growth and coalescence.

Assume that a HIP powder metal has unequal responses in tension and compression, and that the yield surface has no sharp corners. A simple yield function satisfying the above assumptions is

$$\beta^2 \left( \frac{I_1 + \alpha}{3} \right)^2 + J_2 = \sigma_o^2 / 3 \quad (9)$$

A yield function of the form of Eq. (9) has previously been proposed by Green in Ref. 9, Shima and Oyane in Ref. 13, and Kuhn and Downey in Ref. 14. Equation (9) is an ellipse in  $I_1$ ,  $\sqrt{J_2}$  space (Fig. 5), with deformation dependent parameters,  $\alpha$ ,  $\beta$  and  $\sigma_o$ . The yield surface is plotted in principal stress space with  $\sigma_3$  zero in Fig. 6, for the case  $\alpha = 0$ .

Note that as  $\beta$  approaches zero, the Mises yield condition is recovered. In Fig. 3, yield surface Eq. (9) has been plotted with the linear and parabolic Mohr-Coulomb yield surfaces for the case of  $\beta$  equal to one, and  $\alpha$  equal to zero. It should be noted that Eq. (9) predicts a closed yield surface which is smooth where it intersects the hydrostatic axis. Also assuming small strains and an associated flow rule, Eq. (9) implies that, unlike Mohr-Coulomb theories, pure shear stress induces no plastic volumetric change, as shown in Appendix C of Ref. 10.

A large strain theory of plasticity based on Eq. (9) can be developed by decomposing the symmetric part of the velocity gradient tensor,  $D_{ij}$  into elastic and plastic parts, or

$$D_{ij} = \frac{1}{2} \left( \frac{\partial v_i}{\partial x_j} + \frac{\partial v_j}{\partial x_i} \right) = D_{ij}^e + D_{ij}^p \quad (10)$$

The plastic deformation rate  $D_{ij}^p$  is assumed to be given by an associated flow rule

$$D_{ij}^p = \lambda \frac{\partial f}{\partial \sigma_{ij}} \quad (11)$$

where  $\lambda$  is a scalar function greater than zero.

Equations (8) and (11) can be used to solve for the scalar  $\lambda$ . Assume that the parameters  $h_\alpha$  depend on the deformation measures  $n_\alpha$ , or

$$h_\alpha = h_\alpha(n_\alpha) \quad (12)$$

then

$$\lambda = -[\dot{\sigma}_{ij} \frac{\partial f}{\partial \sigma_{ij}}] / [k_\beta (\partial f / \partial h_\alpha) (\partial h_\alpha / \partial \eta_\beta)] \quad (13)$$

where the  $\eta_\beta$  have been chosen so that

$$\dot{\eta}_\beta = \lambda k_\beta (\sigma_{ij}) \quad (14)$$

and

$$(\cdot) = \partial(\cdot) / \partial t \quad (15)$$

A complete discussion of the yield surface considerations for a symmetric yield surface appears in Appendix D of Ref. 10. The choice of the parameters  $\eta_\alpha$  is described in the following section.

#### Choice of Hardening Parameters

In this section, strain hardening of a compacting metal powder is discussed and parameters to characterize hardening are identified. This is necessary to complete the specification of the plastic deformation. Initially, the yield surface of the powder aggregate will be small. During the compaction and sintering process yield strength will grow and the yield surface will expand. Compaction alone will cause growth of the yield surface along only the  $I_1$  axis (Fig. 5) with a theoretical limit corresponding to full densification. Yield stress in shear will be less affected by compaction. Additionally, yield strength will grow in all directions of stress space with increased sintering time. Thus, there exists a time dependent hardening phenomenon unique to powder metallurgy. Since plastic deformations are assumed to occur instantaneously, time enters the plasticity theory as a parameter defining yield surface size at the time of plastic deformation.

The process of strain-hardening in triaxial pressure will primarily be a geometric effect on the microscopic scale. There could also be a contribution to the apparent macroscopic hardening due to real strain hardening of the particles as they experience large plastic shearing deformations. Such an effect could raise the effective yield strength  $\bar{\sigma}$  of the metal particles. The separate contributions of matrix hardening and void reduction can be determined from systematic experiments using different initial volume fractions.

Initially, powder particles contact each other at isolated points. As pressure is applied, the contact areas and the powder stiffness increase. The macroscopic result is strain hardening of the powder due to macroscopic shrinkage. In the limit the powder is completely compacted and the response to further pressure increments is elastic dilation; the plastic bulk modulus has become infinite.

An obvious choice for a deformation measure,  $\eta_1$ , is the void volume fraction defined in Eq. (2). The void volume fraction is a measure of the macroscopic shrinkage and should reflect an increase in stiffness due to an increase in contact area between the individual particles, or

$$\eta_1 = v \quad (16a)$$

The void volume fraction does not represent any permanent changes that occur during plastic deformation. If as in classical plasticity theory the effective plastic strain is used this would not represent all of the permanent deformations since permanent volume changes would not be represented. A third deformation measure, the plastic volume change would then be required.

Rather than use the permanent volume change and the effective plastic strain as two independent deformation measures, a single measure, the plastic work, would be sufficient to represent both effects. Therefore, let

$$\eta_2 = w^p = \int_0^t \sigma_{ij} D_{ij}^p dt \quad (16b)$$

In classical volume preserving plasticity theory using either the plastic work or the effective plastic strain produces exactly the same result. The plastic work, or equivalently the inelastic energy dissipation has been used previously to describe nonlinear material response, for example, in Refs. 15 and 16.

The quantities  $k_\alpha$ , Eq. (14) can now be determined from  $\eta_\alpha$  as

$$k_1 \approx \frac{2}{3} (1-v) \beta^2 (I_1 + \alpha) \quad (17a)$$

and

$$k_2 = \frac{2}{3} \sigma_0^2 \quad (17b)$$

as shown in Appendix A.

Parks, Ref. 17, has pointed out an interesting connection between the plastic work, the void volume fraction, and the effective plastic strain in the solid material. Note that the rate of work done macroscopically on the entire specimen must equal the rate of work done on the solid powder particles, or

$$\int_V \dot{W}^P dV = \int_V \frac{s_{ij}^{solid}}{d_{ij}} \frac{p_{ij}^{solid}}{d_{ij}} dV_{solid} \quad (18)$$

where  $d_{ij} = D_{ij} - 1/3 D_{kk} \sigma_{ij}$

Equation (18) can be equivalently written as

$$\dot{W}^P = (1-v) \bar{\sigma}_{solid} \bar{\epsilon}_{solid}^P \quad (19)$$

where

$\sigma_{solid}$  is the equivalent tensile stress in the solid material, and  
 $\epsilon_{solid}^P$  is the equivalent tensile strain in the solid material.

If the stress-strain relationship for the solid material (i.e.,  $\bar{\sigma}_{solid}$  vs.  $\bar{\epsilon}_{solid}^P$ ) is known then the plastic work can be determined as a function of void volume fraction and equivalent plastic strain in the solid material.

It is now possible to describe the symmetric part of the velocity gradient tensor,  $D_{ij}^A$  in terms of the stress rate, for small strains, using Hooke's Law for the elastic response and Eq. (11) for the plastic response in the form

$$\dot{\sigma}_{ij} = L_{ijkl}^{e.p} D_{kl} = L_{ijkl}^{e.p} \dot{\epsilon}_{kl} \quad (20)$$

where for small strains

$$D_{kl} = \dot{\epsilon}_{kl} \quad (21)$$

In general the yield function is of the form

$$f(\sigma_{ij}, h_\alpha) = 0 \quad (22)$$

where elastic deformations occur when  $f < 0$  and plastic deformations occur when  $f = 0$  and where  $h_\alpha$  are parameters in the yield surface dependent on deformation history measures  $\eta_\beta$ , or

$$h_\alpha = h_\alpha(\eta_\beta)$$

Assume that the plastic deformations are given by an associated flow rule

$$\dot{\epsilon}_{ij}^p = \lambda \frac{\partial f}{\partial \sigma_{ij}} \quad (23)$$

Using Hooke's law for the elastic deformations

$$\dot{\epsilon}_{ij}^e = \frac{1}{E} (1+\nu) \dot{\sigma}_{ij} - \nu \sigma_{kk} \delta_{ij} \quad (24)$$

the total strain rate can be written

$$\dot{\epsilon}_{ij} = \dot{\epsilon}_{ij}^e + \dot{\epsilon}_{ij}^p \quad (25)$$

Equations (20) through (25) can be solved to give

$$\begin{aligned} L_{ijkl}^{e,p} &= \frac{E}{1+\nu} \left\{ \begin{array}{l} \delta_{ik} \delta_{jl} - \frac{\frac{\partial f}{\partial \sigma_{ij}} \frac{\partial f}{\partial \sigma_{kl}}}{\frac{\partial f}{\partial \sigma_{mn}} \frac{\partial f}{\partial \sigma_{mn}} - \left(\frac{1+\nu}{E}\right) H} \\ \delta_{ij} - \frac{\frac{\partial f}{\partial \sigma_{mm}} \frac{\partial f}{\partial \sigma_{ij}}}{\frac{\partial f}{\partial \sigma_{mn}} \frac{\partial f}{\partial \sigma_{mn}} - \left(\frac{1+\nu}{E}\right) H} \\ \delta_{kl} - \frac{\frac{\partial f}{\partial \sigma_{nn}} \frac{\partial f}{\partial \sigma_{kl}}}{\frac{\partial f}{\partial \sigma_{mn}} \frac{\partial f}{\partial \sigma_{mn}} - \left(\frac{1+\nu}{E}\right) H} \end{array} \right\} \\ &+ \left( \frac{\nu}{E} \right) \left[ \frac{\frac{1-2\nu}{E} + \left( \frac{\nu}{E} \right)}{\frac{\partial f}{\partial \sigma_{mm}} \frac{\partial f}{\partial \sigma_{nn}}} \right] \end{aligned} \quad (26)$$

where

$$H = \frac{\partial f}{\partial h_\alpha} \frac{\partial f}{\partial \eta_\beta} k_\beta \quad (27)$$

and

$$\dot{\eta}_\beta = \lambda k_\beta \quad (28)$$

The following yield functions were under consideration to describe the yield surface of a powder metal:

$$\text{I. } f(\sigma_{ij}, h_\alpha) = \beta^2 \left( \frac{I_1}{3} \right)^2 + J_2 - \frac{\sigma_o^2}{3} \quad (29)$$

where

$$h_1 = \sigma_o(v, w^P)$$

$$h_2 = \beta(v, w^P)$$

$$\text{II. } f(\sigma_{ij}, h_\alpha) = \beta^2 \left( \frac{I_1 + \alpha}{3} \right)^2 + J_2 - \frac{\sigma_o^2}{3} \quad (30)$$

where

$$h_1 = \sigma_o(v, w^P)$$

$$h_2 = \beta(v, w^P)$$

$$h_3 = \alpha(v, w^P)$$

$$\text{III. } f(\sigma_{ij}, h_\alpha) = \begin{cases} \beta_1^2 \left( \frac{I_1}{3} \right)^2 + J_2 - \frac{\sigma_o^2}{3} = 0, & I_1 \geq 0 \\ \beta_2^2 \left( \frac{I_1}{3} \right)^2 + J_2 - \frac{\sigma_o^2}{3} = 0, & I_1 \leq 0 \end{cases} \quad (31)$$

where

$$h_1 = \sigma_o(v, w^P)$$

$$h_2 = \beta_1(v, w^P)$$

$$h_3 = \beta_2(v, w^P)$$

and

$v$  is the void volume fraction

$w^P$  is the plastic work

The yield function of Eq. (29) exhibits identical yield stresses in tension and compression and, after application of the associated flow rule, will produce a volume change under compressive loading. Experimental evidence described in the section on Material Property Determination indicates (1) the yield stress

is significantly smaller in tension than in compression, and (2) there is little change in volume during uniaxial compression. Therefore Eq. (29) is not a suitable representation. The yield function of Eq. (31) can be adjusted to produce different yield stresses in tension and compression but would exhibit a volume change in uniaxial compression. Equation (30) can be adjusted to produce different yield stresses in tension than compression and can be adjusted to produce zero volume change in uniaxial compression. Therefore, Eq. (30) will be used to describe the yield surface of powder metals.

Applying Eq. (30) to Eqs. (26, 27, and 28),

$$\frac{\partial f}{\partial \sigma_{ij}} = \frac{2}{3} \beta^2 \left( \frac{I_1 + \alpha}{3} \right) \delta_{ij} + s_{ij} \quad (32)$$

where  $s_{ij}$  = deviatoric stress tensor

$$\frac{\partial f}{\partial \sigma_{mm}} = 2\beta^2 \left( \frac{I_1 + \alpha}{3} \right) \quad (33)$$

$$\frac{\partial f}{\partial h_1} = \frac{\partial f}{\partial \sigma_o} = - \frac{2\sigma_o}{3} \quad (34)$$

$$\frac{\partial f}{\partial h_2} = \frac{\partial f}{\partial \beta} = 2\beta \left( \frac{I_1 + \alpha}{3} \right)^2 \quad (35)$$

$$\frac{\partial f}{\partial h_3} = \frac{\partial f}{\partial \alpha} = \frac{2}{3} \beta^2 \left( \frac{I_1 + \alpha}{3} \right) \quad (36)$$

$$k_1 = 2(1-v) \beta^2 \left( \frac{I_1 + \alpha}{3} \right) \quad (37)$$

and

$$k_2 = \frac{2}{3} \left[ \sigma_o^2 - \alpha \beta^2 \left( \frac{I_1 + \alpha}{3} \right) \right] \quad (38)$$

The quantities  $\frac{\partial h}{\partial \eta_i}$  are hardening parameters which are determined from the mechanical test results and described in the section on Material Property Determination.

#### Large Strain Flow Rule Considerations

The macroscopic deformations during HIP can be large with volume reductions approaching 30 percent. Consequently, a rigorous finite deformation formulation of the process is required. It should be noted that a finite deformation analysis need be employed only if a material point undergoes a large volume change or if a material line element undergoes a large orientation change. In the present case, it may be expected that only the former effect is sufficiently large to mandate the finite deformation analysis. However, the possibility of large rotations will be included in the following discussion.

Two approaches to problems involving finite deformation are: (1) refer all continuum variables to a fixed initial reference configuration, or (2) continuously update the reference configuration to the current (most recent) configuration. The finite element implementation of these methods for large plastic deformation has been discussed by Hibbit, Marcal and Rice (Ref. 18) and McMeeking and Rice (Ref. 19). The updated Lagrangian formulation of McMeeking and Rice, though fully equivalent to that of Hibbit et al., is superior. The formulation of McMeeking and Rice is computationally simpler, there are fewer terms in the stiffness matrix computation and the yield condition is simpler to express.

Following McMeeking and Rice, note that, with the current deformed state as the reference configuration, all stress measures coincide:  $\sigma_{ij} = S_{ij} = \tau_{ij} = \epsilon_{ij}$  where the stresses are, respectively, Cauchy (true), second Piola-Kirchhoff, Kirchhoff, and first Piola-Kirchhoff stress measures. However, the rates associated with these stress measures do not coincide. A stress rate which is useful for expressing large deformation constitutive laws is the Jaumann, or co-rotational rate (Ref. 20). The Jaumann rate of Cauchy stress is

$$\dot{\sigma}_{ij} = \sigma_{ij} - \sigma_{ip} \Omega_{pj} + \Omega_{ip} \sigma_{pj} \quad (39)$$

where  $\dot{\sigma}_{ij}$  is the material time rate of Cauchy stress  $\sigma_{ij}$  and

$$\Omega_{ij} = \frac{1}{2} (\partial v_i / \partial x_j - \partial v_j / \partial x_i)$$

The constitutive law of interest is of the form

$$\nabla \sigma_{ij} = L_{ijkl} D_{kl} \quad (40)$$

where  $L$  denotes the rate moduli,  $D_{ij}$  is the symmetric part of the velocity gradient tensor.

$L_{ijkl}$  is developed in Ref. 21 for large strains as

$$L_{ijkl} = L_{ijkl}^{e,p} - \frac{1}{2} \left[ \delta_{ik}\sigma_{jl} + \delta_{jk}\sigma_{il} + \delta_{il}\sigma_{jk} + \delta_{jl}\sigma_{ik} \right] + \sigma_{ij}\delta_{kl} \quad (41)$$

and  $L_{ijkl}^{e,p}$  is the small strain elastic-plastic stiffness in Eq. (20). The tensor  $L_{ijkl}$  is not symmetric due to the presence of the last term, or

$$L_{ijkl} \neq L_{klij}$$

For a hydrostatic pressure

$$\sigma_{ij} = P\delta_{ij} \quad (42)$$

the tensor is symmetric and since this should be the primary part of the loading during the HIP process, the last term should produce a nearly symmetric stiffness. It, therefore, was decided to separate the last term into symmetric and unsymmetric parts, and add the symmetric part to the stiffness matrix and transfer the unsymmetric part of the loading side of the governing equations.

#### Time Dependent Deformation

In the HIP process two time effects are present: the strength growth of the metal powder as bonds between contacting particles grow and time dependent deformation as voids shrink. Powder strength growth was modeled as the time dependent expansion of the plastic yield surface.

In the small strain theory of metals it is assumed that the total strain  $\epsilon_{ij}$  can be represented as

$$\epsilon_{ij} = \epsilon_{ij}^e + \epsilon_{ij}^p + \epsilon_{ij}^c \quad (43)$$

where  $\epsilon_{ij}^e$ ,  $\epsilon_{ij}^p$  and  $\epsilon_{ij}^c$  are the elastic, plastic and creep parts of the strain, respectively. The elastic strain is time independent and recoverable, the plastic strain is time independent and irrecoverable, and the creep strain is time dependent and irrecoverable. Typically, creep deformations in metals are significant when absolute temperatures are greater than one half of metal melting point. Also, creep deformations are volume preserving. Creep laws for constant uniaxial stress are usually expressed as

$$\dot{\epsilon}^c = f(\sigma, t, T) \quad (44)$$

where  $\dot{\epsilon}^c = d\epsilon^c/dt$  is the rate of uniaxial creep strain and  $\sigma$ ,  $t$  and  $T$  are uniaxial stress, time and temperature, respectively. An example of Eq. (28) is the Norton - Bailey power law (Ref. 22):

$$\dot{\epsilon}^c = A(T)\sigma^m t^k \quad (45)$$

If the creep rate is steady the creep strains can be written as

$$\epsilon^c = B(T)\sigma^n \quad (46)$$

where  $A$ ,  $B$ ,  $m$  and  $n$  are determined by fitting the function to experimental creep strain data. Experimental data is usually in the form of creep strain as a function of time for a fixed stress and temperature.

To obtain creep strain rates for multiaxial stress states it is customary to generalize uniaxial creep laws in a manner analogous to the derivation of the Prandtl-Reuss equations of classical plasticity (Ref. 22) giving

$$\dot{\epsilon}_{ij}^c = \frac{3}{2} \frac{\dot{\epsilon}^c}{\bar{\sigma}} S_{ij} \quad (47)$$

where

$$\dot{\epsilon}^c = \sqrt{\frac{2}{3} \dot{\epsilon}_{ij}^c \dot{\epsilon}_{ij}^c}, \bar{\sigma} = \sqrt{\frac{3}{2} S_{ij} S_{ij}} \quad (48)$$

are the equivalent creep strain rate and equivalent stress, respectively, and are assumed related according to

$$\dot{\epsilon}^c = f(\bar{\sigma}, t, T) \quad (49)$$

In the HIP process temperatures are between 80 and 90 percent of the powder metal melting point. Therefore, creep deformation is possible as voids in the compacting powder shrink. However, it is difficult to observe such creep in a HIP test because of the time necessary to pressurize and depressurize the HIP facility. Standard HIP practice utilizes a monotonic increase in pressure and temperature over a period which may be as long as an hour, followed by a two or three hour hold at pressure and temperature. In the partial HIP experiments specimens differing only by the time they are maintained at temperature and pressure were fabricated. Time dependent volumetric shrinkage can be computed by comparing the amount of densification. Thus a volumetric creep strain law can be experimentally derived. A possible expression for this law is

$$D_{kk}^c = -A P^m t^k \quad (50)$$

while for a steady creep

$$D_{kk}^c = B P^n$$

which is analogous to Eq. (45). Here  $D_{kk}^c$  is the trace of the creep component of the velocity gradient  $D_{ij}^c$ ,  $P$  is the HIP pressure and  $t$ , time.

To derive a creep law for the deviatoric component  $\hat{D}_{ij}^c$  of the creep strain velocity gradient a law of the form

$$\hat{D}_{ij}^c = \Lambda \partial f / \partial S_{ij} \quad (51)$$

is postulated where, parallel to the small strain theory,  $f$  is the yield function for the compacting metal powder. If the classical Mises yield function is used, Eq. (51) reduces to

$$\hat{D}_{ij}^c = \Lambda S_{ij}$$

This may be rewritten as

$$D_{ij}^c = \frac{3}{2} \frac{\hat{D}_{ij}^c}{\bar{\sigma}} S_{ij} \quad (52)$$

where analogous to Eq. (47)

$$\overline{\hat{D}^c} = \sqrt{\frac{2}{3}} \overline{\hat{D}_{ij}^c \hat{D}_{ij}^c}, \quad \bar{\sigma} = \frac{\sqrt{3}}{2} S_{ij} S_{ij} \quad (53)$$

To complete this creep law a relationship of the form of Eq. (46) is chosen

$$\overline{\hat{D}^c} = B\sigma^n \quad (54)$$

where steady state creep is assumed. The constants B and n are temperature and void volume fraction dependent. They can be determined directly from relaxation tests of partially dense specimens, and are fully described in the section on Material Property Determination.

The dominant creep mechanism can be determined by examining creep deformation maps presented by Ashby in Ref. 6. The map for nickel is the most appropriate map since nickel based superalloys are being modeled. The creep deformation map, from Ref. 6, for nickel is reproduced in Fig. 8 with experimental points outlining the partial HIP experiments with MERL 76. The major creep mechanism for HIP operating conditions appears to be dislocation creep if it is assumed that the pressure is approximately equal to the tensile stress. Steady state dislocation creep is generally described by Eq. (46) with the temperature dependent function represented by an activation energy. Equation (46) can be rewritten as

$$\dot{\epsilon}_{creep} = \frac{1}{t_0} e^{-\frac{T_0}{T}} \left( \frac{\sigma}{\sigma_0} \right)^N \quad (55)$$

where  $\dot{\epsilon}$  creep is the uniaxial creep rate,  
 $\sigma$  is the uniaxial stress  
 $T$  is the absolute temperature  
 $\sigma_0$  can be assigned an arbitrary value  
 $t_0$ ,  $T_0$  and N are material constants

From Wilkinson and Ashby, Ref. 23, the relative density is given by

$$\dot{\rho} = k \left[ \frac{1}{t_0} e^{-\frac{T_0}{T}} \right] \left[ \frac{k}{N} \left( \frac{P}{\sigma_0} \right) \right]^N \left\{ \frac{\rho(1-\rho)}{[1-(1-\rho)^{1/N}]^N} \right\} \quad (56)$$

where  $\rho = 1-v$  is the relative density, and  $k$  is  $\frac{3}{2}$  for final densification and 2 for intermediate densification. The relative density after plastic deformation,  $\rho_0$ , is used as the initial condition in Eq. (56) and is calculated using the equations (61) and (62). The constants  $t_0$ ,  $T_0$  and  $N$  are determined from partial HIP experiments.

#### Microstructural Modeling to Develop Macroscopic Constitutive Laws

In general, experimental difficulties associated with instrumentation and facility capabilities preclude experimental determination of all material properties needed in the constitutive theory. For example, it will not be possible to probe the entire yield surface of a partially dense HIP powder. Thus, analytical and numerical microstructural models of the HIP process are needed to augment the understanding of the constitutive theory. This section reviews previous analysis of metal microstructural effects and discusses additional analyses performed to further define the constitutive theory.

Voids in plastically deforming metals have been modeled by several authors. Gurson (Ref. 24) has developed approximate yield surfaces for materials with microscopic voids. The principal interest in Gurson's studies was in assessing ductile fracture of polycrystalline materials containing voids or impurities which nucleate holes that microscopically grow and coalesce into a macroscopic fracture event. For porous metals, Green (Ref. 9) has assumed a yield function of the form of Eq. (9) with  $\alpha$  equal to zero, and has evaluated the dependence of  $\beta$  and  $\sigma_0$  on void volume ratio by modeling an isolated spherical void in a metal matrix under external hydrostatic pressure. Finite element elastic-plastic modeling of the growth of voids contained within unit cells of homogeneous material has been performed by Needleman (Ref. 12). Mullins, et al. (Ref. 25), have performed a small stain, finite element, elastic-plastic, hardening analysis of a spherical pore under remote hydrostatic pressure and have obtained results similar to Green for void shrinkage as a function of pressure. The previous analyses considered isolated voids.

Time dependent microstructural effects have been less extensively modeled. Many authors (Refs. 3-7, 26 and 27) have postulated the presence of microstructural creep mechanisms in both HIP and pressureless sintering but no definitive conclusions on the importance of these mechanisms have been reached. The most systematic approach to understanding microstructural mechanisms has been the deformation maps of Ashby (Ref. 6) discussed earlier. However, Ashby's work was directed toward determining when different mechanisms are active rather than quantifying the effect of these mechanisms on powder densification. Finite element modeling of void growth caused by steady-state creep deformation has been modeled by Burke (Ref. 28). In Burke's analysis steady-state creep was assumed, the geometry was a uniformly spaced distribution of spherical voids corresponding to a void fraction of 5 percent, and the loading was remote uniaxial tension.

The above plastic and creep analyses were concerned only with imbedded voids, but during the HIP process the initial response of the powder metal, when it is the weakest, contributes significantly to final deformations. Models based on imbedded voids will be accurate in the final stages of densification but do not correctly represent the initial stages of densification. During the initial stages models based on the contact between spherical particles should be more accurate.

Finite element modeling of regular arrays of spherical particles, illustrated in Fig. 9, was performed to determine the macroscopic response during the initial stages of compaction. The finite element modeling is fully described in Ref. 29, and resulted in the conclusion that the initial stages of compaction can be simply modeled as isolated equal size spheres in contact. When the effects of the spheres containing a common central sphere began to interact, the numerical simulations became unstable and the analyses were terminated.

The finite element predictions were compared with results from elastic and plastic theories of contact (Refs. 30-33). When substantial plasticity is present, the pressure distribution over the contact surface is approximately uniform and is given by

$$P = C\sigma_y \quad (57)$$

where  $\sigma_y$  is the yield stress of the powder particle, and

$$C \approx 2.75 \quad (58)$$

Equation (57) was used to describe the initial stages of plastic densification and from Ref. 29 resulted in the following relationship

$$(P/\sigma_y)^{2/3} = C [(\rho/\rho_i)^2 - 1]/\tan^2 \theta \quad (59)$$

where  $\rho = 1-v$  is the relative density,

$$\cos \theta = \frac{\rho_i}{4} + \sqrt{\left(\frac{\rho_i}{2}\right)\left(\frac{1+\rho_i}{8}\right)} , \text{ and} \quad (60)$$

$\rho_i$  is the initial relative density.

Equation (59) compares well with the finite element results as illustrated in Fig. 10. The initial slope of Eq. (59) appears to accurately describe the initial stages of densification while the finite element results appear to approach the final densification model of Eq. (1). These two relationships can be connected by taking

$$\frac{P}{\sigma_y} = \frac{2}{3} \left[ -\ln\left(\frac{v}{v_i}\right) - \left(1 - \frac{v}{v_i}\right)^2 \ln v_i + a \left(\frac{v}{v_i}\right) \left(1 - \frac{v}{v_i}\right) \right] \quad (61)$$

which satisfies the condition

$$v = v_i \text{ at } P = 0$$

and has the same initial slope as Eq. (59) if

$$a = \frac{C v_i}{(1-v_i) \tan^2 \theta} - 1 \quad (62)$$

Equation (61) is also plotted in Fig. 10 and shows excellent agreement with the finite element modeling.

The plastic work and current void volume fraction are being used as parameters for the mechanical response of partially densified powder metals. The plastic work, void volume fraction path during a HIP cycle, where the powder metal is subjected to a pure hydrostatic pressure, can be found from

$$\dot{W}^P = \sigma_{ij} D_{ij}^P \quad (64)$$

where  $W^P$  is the plastic work

$\sigma_{ij}$  is the Cauchy Stress

$$D_{ij} = 1/2 (v_{i,j} + v_{j,i})$$

$v_{i,j}$  is the velocity gradient, and

$$(') = d(\ )/dt$$

For a hydrostatic pressure

$$\sigma_{ij} = -P \delta_{ij} \quad (65)$$

and

$$\dot{W}^P = -P D_{kk}^P \quad (66)$$

From Appendix A, Eq. (A.23)

$$D_{kk}^P \approx \frac{\dot{v}}{1-v}$$

where  $v$  is the void volume fraction

Then Eq. (66) becomes

$$\dot{W}^P = \frac{-\dot{P}\dot{v}}{1-v} \quad (67)$$

or

$$W^P = - \int_{v_i}^{v_f} \frac{P(v)dv}{1-v} \quad (68)$$

which is the plastic work performed between void volume fractions  $v_i$  and  $v_f$ , where

$v_i$  is the initial void volume fraction, and  
 $v_f$  is the final void volume fraction.

Equation (61) can now be substituted into Eq. (68) to find the plastic work as

$$\frac{W^P}{\sigma_y} = \frac{2}{3} \left[ f(1-v_f) - f(1-v_i) \right] + n_0 \ln \left( \frac{1-v_f}{1-v_i} \right) + \frac{n_2}{v_i^2} \left[ \ln \left( \frac{1-v_f}{1-v_i} \right) - (v_i - v_f) - \frac{1}{2} (v_i^2 - v_f^2) \right] + \frac{n_1}{v_i} \left[ \ln \left( \frac{1-v_f}{1-v_i} \right) - (v_i - v_f) \right] \quad (69)$$

where

$$n_2 = a - 1nv_i$$

$$n_1 = a + 2 \ln v_i$$

$$n_0 = -1nv_i$$

$$f(x) = \sum_{k=1}^{\infty} \frac{x^k}{k^2}$$

The function  $f(x)$  is presented in Table 2.

In general the effects of plasticity and creep will be separated in order to describe the material properties. A yield function of the form of Eq. (9) was preferred. Two deformation measures, the void volume fraction and the plastic work, were used to represent the dependence of the parameters in the yield function. Under these assumptions the small strain elastic-plastic stress-strain law is given by Eqs. (20), (22) and (26). The effects of large strains, using the Cauchy stress, are included in Eq. (41). A nonsymmetric stiffness matrix results and the nonsymmetric terms are transferred to the loading side of the equilibrium equations. The effects of creep have been divided into two parts, the volumetric and deviatoric. Power law creep models have been assumed.

Based on the finite element models of compacting spheres expressions, Eq. (61), relating void volume fraction, or relative density, and pressure, for a powder metal subjected to pure hydrostatic compression have been derived. In addition, the plastic work done while the powder metal is subjected to a pure hydrostatic pressure has also been derived.

## CODE MODIFICATIONS

### General Considerations

A numerical simulation of the constitutive model is required to utilize the model in the analysis and prediction of HIP processes. The numerical simulation is also employed in both the formulation and evaluation of the constitutive model.

There are several available finite element codes that have the large strain capability required to model the HIP process. For example, the MARC finite element code (Ref. 34), can be applied to a wide variety of nonlinear solid mechanics problems. However, none of the available codes presently contains a constitutive theory that would adequately model the HIP process.

The necessity for modeling large strains arises from the 30 percent volume reduction typically experienced during the HIP process. A finite strain elastic-plastic constitutive model of the HIP process was formulated in terms of the Jaumann rate of Cauchy stress  $\sigma_{ij}$  and the symmetric part of the velocity gradient,  $D_{ij}$ . Additionally, the simplicity of an updated Lagrangian finite element formulation of the constitutive modeled is preferred. Level H-4 of the MARC nonlinear finite element code uses the McMeeking and Rice (Ref. 19) form of this finite element formulation and permits use of constitutive models of the form Eq. (20). This code was modified to permit the modeling of the HIP process.

In order to numerically evaluate the response of the material each of the response types was separated. One common approach in small strain deformations (see Ref. 34) is to divide the strain rate into its elastic, plastic, creep and thermal parts. The total strain rate could then be expressed as:

$$\dot{\epsilon}_{ij} = \dot{\epsilon}_{ij}^{el} + \dot{\epsilon}_{ij}^{pl} + \dot{\epsilon}_{ij}^{cr} + \dot{\epsilon}_{ij}^{th} \quad (70)$$

where  $\dot{\epsilon}_{ij}$  is the total strain rate,

$\dot{\epsilon}_{ij}^{el}$  is the elastic strain rate,

$\dot{\epsilon}_{ij}^{pl}$  is the plastic strain rate,

$\dot{\epsilon}_{ij}^{cr}$  is the creep (or time dependent) strain rate, and

$\dot{\epsilon}_{ij}^{th}$  is the thermal strain rate.

In Fig. 11 the elastic and plastic strain components are presented for a uniaxial stress-strain case. Note that in Fig. 11 a second strain rate decomposition can be considered in place of Eq. (70). For the second possibility, considering just the elastic and plastic components of the strain rate, Eq. (70) would become

$$\dot{\epsilon}_{ij} = \dot{\epsilon}_{ij}^{el1} + \dot{\epsilon}_{ij}^{elpl} \quad (71)$$

A small strain numerical iterative procedure based on Eq. (71) for the evaluation of the elastic-plastic response will be presented in the next section. A parallel development based on analogous additive decomposition of the stretching tensor is straightforward.

The finite element code should contain the appropriate element types to describe the deformation of the powder metal during HIP. In the MARC H.4 large strain version, all of the solid elements can be used in an updated Lagrangian formulation, including three, four and eight node isoparametric axisymmetric ring elements.

The following sections will consider in more detail: (1) iteration schemes for the solution of the resulting nonlinear system of equations and (2) the changes to the constitutive portion of the MARC code.

#### Plastic Iteraction Procedure

Consider the case of a small strain elastic-plastic response of a typical structure. Sufficiently large applied loads will result in permanent or plastic deformation. A procedure for calculating the response of the structure undergoing plastic deformation is required. A method analogous to that presented in Ref. 32 will be discussed.

To evaluate the response of the structure, the loading history may be divided into a number of incrementally applied loading steps. Each of these load increments can then be applied sequentially to the structure. An iterative scheme is then required to calculate the response of the structure to each individual load increment.

At the beginning of a new load increment it may be assumed that the strain will change in a manner analogous to the previous increment. As an initial estimate all of the strain change is then assumed to be elastic. The change in the stresses can then be calculated using Hooke's Law or

$$\Delta\sigma_{ij} = L_{ijkl}^e \Delta\varepsilon_{kl} \quad (72)$$

where  $\Delta\sigma_{ij}$  is the incremental stress vector

$\Delta\varepsilon_{kl}$  is the incremental total strain vector, and

$L_{ijkl}^e$  is the matrix of elastic constants.

If the resulting total stress is within the yield surface, the matrix of material constants,  $L_{ijkl}$  is simply given by

$$L_{ijkl} = L_{ijkl}^e \quad (73)$$

If the resulting total stress is outside the yield surface weighted material constants and stiffness matrices will have to be calculated. It should be noted at this point that if a load increment is exceedingly large and if there is a sudden change in the type of loading, care must be taken in order to iterate to the correct solution.

If the resulting total stress is outside the yield surface, the fraction of the stress increment that remains elastic must be determined. This corresponds to  $\Delta\varepsilon_{ij}^{el}$  in Fig. 11. If the yield surface in stress space is considered to be given by

$$f(\sigma_{ij}) = 0,$$

then the appropriate  $m$  in

$$f(\sigma_{ij}^{i-1} + m\Delta\sigma_{ij}) = 0 \quad (74)$$

may be determined where  $\sigma_{ij}^{i-1}$  is the stress tensor from the previous increment. The mean material matrix is calculated from

$$L_{ijkl}^e = m L_{ijkl}^e + (1-m) L_{ijkl}^{e-p} \quad (75)$$

where  $L_{ijkl}^{e-p}$  is the tensor relating  $\dot{\sigma}_{ij}$  and  $\dot{\epsilon}_{kl}$  in Eq. (20).

Once the tensor  $L_{ijkl}$  has been determined, standard finite element solutions can be applied to find the incremental changes in the displacements, strains and loads. For example, if the strains are given by

$$\{\Delta\epsilon\} = [\beta] \{\Delta u\} \quad (76)$$

where  $\{\Delta u\}$  is the vector of incremental nodal displacements, and  $[\beta]$  is the matrix relating the vector of element strains  $\{\Delta\epsilon\}$  to the nodal displacements, the stiffness matrix can be found from

$$[K] = \int_V [\beta]^T [D] [\beta] dV. \quad (77)$$

The incremental nodal displacements and strains can be evaluated by solving for  $\Delta u$  in

$$[K] \{\Delta u\} = \{\Delta P\} + \{P-I\} \quad (78)$$

and then applying Eq. (76).

The term  $\Delta P$  in Eq. (77) is the applied incremental load. The term  $\{P-I\}$  is defined as the residual load correction and is added to Eq. (77) to insure the total external loads,  $\{P\}$ , and the total internal reactions,  $\{I\}$ , remain balanced over all the load increments. The relation

$$\{P\} - \{I\} = \{0\} \quad (79)$$

where

$$I = \int_V [\beta]^T [\sigma] dV \quad (80)$$

continues to hold throughout the loading history.

One iteration cycle is completed each time the stiffness matrix is formed and the resulting equations solved. At the end of each cycle the resulting solution must be tested for convergence. This is accomplished, by considering the ratio

$$r = \frac{\Delta E^N - \Delta E^{N-1}}{\Delta E^N} \quad (81)$$

where  $\Delta E^{N-1}$  is the change in energy summed over all elements on the previous cycle and  $\Delta E^N$  is the change for the present cycle.

An accurate solution will usually result if  $r$  is maintained less than 0.1 for elastic-plastic problems.

If the solution has satisfied the convergence, the stresses and strains can be updated and a new load increment added. If the solution has not converged then a new guess for the strains, based on the latest cycle, must be input and the calculation procedure repeated. When the solution has not converged after a given number of cycles, the program should exit from the load incrementing loop.

Figure 12 is a flow chart illustrating the small strain elastic-plastic iteration procedure.

For finite strain plasticity the stiffness matrix has the additional terms presented in Eq. (41).

#### Time Effects Iteration Procedure

The metal particles will creep to fill the void space when subjected to high temperature and pressure. The reduction of void space will depend on the time that the powder is subjected to the high temperature, high pressure conditions. The creep strain rate will depend in general on the stress, the accumulated creep strain, the temperature and time. To illustrate the incrementing procedure assume that the creep strain rate is normal to the Mises yield surface in stress space, then the creep strain rate is given by Eq. (47).

For a specific time increment the incremental creep strain will be

$$\Delta \epsilon_{ij}^{cr} = \dot{\epsilon}_{ij}^{cr} \Delta t. \quad (82)$$

The incremental displacements are

$$[K] [\Delta u] = [\Delta P] + [P-I] + [\Delta P^*] \quad (83)$$

where

$$\{\Delta P^*\} = \int \{B\}^T \{C\} \{\Delta \epsilon^c\} dV \quad (84)$$

is the pseudo-creep load and  $\{\Delta \epsilon^c\}$  is the vector of element creep strain. The strain increment can be calculated from Eq. (76) and the strains, creep strains, stresses and displacements can be updated.

A convergence test on the stresses should be performed. If the algorithm has not converged a shorter time step should be used and the calculations repeated. If the criterion has been satisfied then the time step can be increased. Figure 13 is a flow chart illustrating the small strain creep iteration procedure.

#### Code Selection, Installation, and Testing

In addition to the MARC computer code, selected for use in the program, several other codes were examined. Table 3 lists each of the codes considered. The code selected should be able to simulate the response of the powder metal and the container. The response will be assumed to be axisymmetric and therefore axisymmetric continuum and axisymmetric shell elements should be included in the element library. Four of the eight computer programs listed do not contain axisymmetric shell elements and are therefore unsuitable. These four codes are: HONDO, FIPAX, PLANS, and NON-NISA. The HONDO code contains a very general constitutive routine that could be utilized for the non-volume preserving plasticity theory. However, HONDO does dynamic problems only and would not be a cost effective approach. Both the ANSYS and ADINA codes do not have the capability to perform large strain calculations and would require extensive modifications. The NEPSAP code can perform large strain calculations but uses a total Lagrangian formulation. For reasons states previously, an updated Lagrangian formulation is preferred.

The MARC H.4 large strain code was obtained and installed. The initial test case modeled a rigid plastic hardening tensile specimen subjected to a uniaxial stress state. The MARC code successfully simulated the large strain response of the tensile specimen. Figure 14 shows that at displacements as high a 70 percent of the original specimen length the code results were nearly identical to the theoretical values.

### Code Modifications

To analyze the powder plastic flow the plasticity theory described previously must be incorporated in the MARC code. The MARC code applies the algorithm of Rice and Tracey, in Ref. 35, in the subroutine THRUS. Therefore, one approach would be to modify THRUS to include nonvolume preserving plasticity. The MARC program also contains user subroutines which the general user writes to incorporate special features of his analytical model. One of these user subroutines, HYPELA, can be used for hypoelastic material properties (i.e., nonlinear elastic material properties). Subroutine HYPELA has for input the initial strain increment, and the stress state from the previous increment. The increment number can be brought in through a COMMON block. A third approach using the user subroutines appropriate to a specialized form of viscoplasticity can also be used.

Incorporating the nonvolume preserving plasticity theory into the MARC code through the user subroutine HYPELA requires writing only the one subroutine while modifications to THRUS would also require modifications to several connected subroutines. Therefore, the first step was to try HYPELA using the problem illustrated in Fig. 14 as a test case. The test was successful with the predictions being identical to the results presented in Fig. 14.

The nonvolume plastic flow equations were incorporated as modifications to the MARC code through the user subroutine HYPELA. A flow chart of the modifications is shown in Fig. 15. The first attempts at integrating the plastic flow equations were modifications of the algorithm developed by Rice and Tracey (Ref. 35). These attempts were only partially successful and a direct integration using Runge-Kutta was employed. Adapting a method described by Parks (Ref. 36), the Runge-Kutta integration strain increments are a fraction of the total strain step, where the fraction is specified by the user. If the final stress state drifts more than a user specified distance from the yield surface, the strain increments are reduced in size an amount again specified by the user. If the strain increments decrease below a user specified fraction of the total strain step, a correction to the final stress state is made by bringing the stress back to the yield surface along the normal to the yield surface, and the appropriate modification is made to the elastic-plastic moduli.

The MARC code modifications were run independent of the MARC code for several simple test cases, two of which are illustrated in Figs. 16 through 18. They show excellent agreement with the theoretical solution using approximately one percent total strain steps in the integration algorithm. In Figs. 16 and 17, the material response when subjected to a uniform pressure is illustrated. Figure 16 presents the pressure as a function of the density and shows only minor variations between the numerical and theoretical response. The void volume fraction as a function of strain compares exactly as illustrated in Fig. 17. The stress state did vary from hydrostatic but the error in the second invariant of the deviatoric stress tensor,

$J_2$ , was always less  $0.3 \times 10^{-4}$  of the square of the initial particle yield stress  $\sigma_y$  in Eq. (61). The uniaxial compression test case as illustrated in Fig. 18 was exactly on the theoretical variation with the void volume fraction remaining constant to four places. Both of the above cases were run with and without correcting the final stress state with the same results to four significant figures.

The code modifications were then added to the MARC finite element code and tested on the same two sample cases. The agreement between theoretical and the numerical code predictions was excellent although somewhat smaller strain steps were required for numerical stability. The unsymmetric part of the stiffness moduli were added to the MARC code and effects of creep were included through the user subroutines CRPLAW and VS WELL. This approach for including creep is not entirely adequate but the inadequacies can be easily removed in the new version of MARC released in June 1980.

#### MATERIAL PROPERTY DETERMINATION

To predict the mechanical response of metal powder subjected to the HIP process it is necessary to know the mechanical properties of the metal during the HIP cycle. These mechanical properties can be obtained by removing test specimens from the HIP facility at various stages in a HIP cycle. The partial HIP samples would represent the powder at various stages for a pressure-temperature history. A complete description of the mechanical properties can then be obtained by postulating yield surfaces, flow rules, hardening laws and creep properties and comparing these predictions to the results of mechanical tests on the partial HIP samples.

#### Partial HIP Tests

The UTRC HIP facility has been utilized to process powder metals through temperature-pressure-time profiles closely paralleling the procedure used to fabricate full size turbine disks to near net shape. Figure 19 shows a representative temperature-time history detailing the mode of consolidation being used to fabricate full size disks. Two distinct phases of thermal history should be noted.

In the first phase (preheat) the metal powder is preheated for 3 hr at temperatures rising from 1500 F to 2000 F and then held at 2000 F for 8 hr. All of the preheat cycle is done at 1 atm pressure. During the preheat phase some sintering occurs and the powder acquires sufficient strength to be handled. In the second phase, the preheated powder sample is transferred to the HIP unit. During the first hour, the temperature and pressure are raised to 2135 F and 5000 psi, respectively. During the next 1-1/2 hr the pressure continues to rise to the full 15,000 psi. The pressure, 15,000 psi, and temperature, 3125 F, are then maintained for 3 hrs, to complete the densification.

UTRC facilities allow several partial HIP samples to be preheated simultaneously. Since the powder is initially weak a container is required to retain the powder shape for temperatures exceeding 2000 F. Therefore, during the preheat cycle the powder is encapsulated in quartz. During the preheat the density changed from 60 to 65 percent of full density initially to 65 to 70 percent of full density upon completion of the cycle. All specimens were preheated at 2000 F and 1 atm for 12 hr.

After the completion of the preheat cycle the samples have the quartz container removed and a glass container substituted. At HIP temperatures the inside surface of the glass container fuses with the outer powder metal particles and forms a gas tight seal about the powder metal. The glass has no strength or

stiffness. Consequently, a uniform hydrostatic stress is transmitted to the powder metal. The glass container with the preheated or sintered powder metal is next placed in the HIP facility and subjected to a specified temperature, pressure time cycle.

In Fig. 20, a specimen is shown in different stages of a partial HIP cycle. The specimen is shown encapsulated in quartz before the preheat cycle. A sintered or preheated bar is shown in glass before HIP, and a partially densified bar is shown with the end removed for density measurements.

A 100 lb lot of MERL 76 powder, blend 61578, was obtained and samples were subjected to sieve and chemical analyses. A comparison of the results of the blend chemical and sieve analyses with a blend used in other programs showed the two blends to be essentially identical.

The first three partial HIP experiments attempted to find a pressure at 2135 F, the standard MERL 76 HIP temperature, which induced less than full powder densification. MERL 76 powder was encapsulated in stainless steel tubes with 0.75 in. and 0.06 in. external diameter and wall thickness, respectively. After the filled tubes were outgassed to remove air, their ends were crimped and welded shut. The tubes were then sintered in a furnace for 12 hr at 2000 F and allowed to cool to room temperature. Subsequently, each tube was reheated to 1200 F, loaded into the HIP unit which was also at 1200 F, and subjected to a pressure temperature cycle. The pressure-temperature cycle for specimen 3 is shown in Fig. 21. Maximum HIP pressures for specimens 1, 2 and 3 were 5000 psi, 2500 psi and 1000 psi, respectively. Specimen 1 was held at peak pressure for 20 min while specimens 2 and 3 experienced peak pressure for only ten minutes. In all three experiments the powder was completely compacted.

It can be concluded that densification occurs so rapidly at 2135 F that HIP pressure and time cannot be controlled accurately enough to partially densify MERL 76. Therefore, present experiments are directed towards partially densifying powder in the 1600 F to 2000 F temperature range. The results obtained must then be extrapolated to predict densification rates at 2135 F.

Experiments 4, 5 and 6 investigated the short time response of powder to pressure. From these tests, it was observed that between 1600 F and 1800 F little short term densification occurs at 1000 psi. These first six tests indicated that between 1600 F and 2000 F and between 1000 psi and 15,000 psi partially densified specimens would result.

The next set of tests was performed at 1800 F and various pressure, with the maximum temperature and pressure acting for 10 minutes only. These tests were successful in producing partially dense samples. The test regime was expanded to include 1600 F, 1900 F and 2000 F at appropriate pressures and again the time at maximum temperature and pressure was held to 10 min. Finally, a set of

experiments at various times was performed to determine the effects of creep. Table 4 is a listing of each of the partial HIP experiments completed.

Some understanding of the compaction process can be obtained by applying the full density range plastic compaction model, Eq. (61) in the Section of Microstructural Modeling. In order to apply the model the yield stress of the powder particle material must be known. This data does not exist and therefore the short time partial HIP data has to be reduced to determine the yield stress. For each of the temperatures, 1600 F, 1800 F, and 2000 F, the yield stress was estimated and Eq. (61) was applied to determine the relative density for various applied pressures. Figure 22 presents the results of the calculations and demonstrates good agreement for the yield stresses given by

$$\sigma_y = \left( 1.1 \times 10^9 \text{ ksi} \right) e^{-\frac{T}{120.7 R}} \quad (84)$$

Equation 84 results in yield stresses that are somewhat low for superalloys. Three facts could account for this: (1) the yield stress for the pre-HIP powder metal is generally lower than for the fully consolidated powder, (2) the strain rate during a partial HIP cycle is relatively slow and therefore produces a somewhat lower effective yield stress, and (3) the creep rates at high temperatures are relatively high, producing an apparently lower yield stress.

The effects of creep on the density can be examined by applying Eq. (56), which was derived by Wilkinson and Ashby in Ref. 23. The relative density after plastic deformation,  $\rho_o$ , is used as the initial condition in Eq. (56) and is calculated using (61). The relative density before any plastic deformation was taken as

$$\rho_i = 0.70$$

and the condition

$$\rho = \rho_o$$

was applied at

$$t = 10 \text{ min.},$$

which is the minimum time the partial HIP specimens were maintained at maximum temperature and pressure.

An analyses of the densities for the partial HIP experiments performed indicates the constants in Eq. (56) are given by

$$\begin{aligned} N &\approx 2 \\ t_o &\approx 2 \times 10^{-13} \text{ min} \\ T_o &\approx 73000 \text{ R} \end{aligned}$$

when

$$\sigma_0 = 15 \text{ ksi}$$

In Fig. 23, the calculated relative density is compared to their experimental values with fair agreement.

Photomicrographs of two partially dense HIP rods at 1800 F are shown in Fig. 24. The majority of the particles have remained nearly spherical, while a few particles appear to be severely deformed.

#### Mechanical Tests

The major objectives of the mechanical tests are: (1) to determine the yield surface, (2) to measure the elastic properties of partial HIP metal powders, (3) to examine hardening flow rules, and (4) to determine the creep properties of the partial HIP samples. After the partially dense HIP material is removed from the furnace it must be machined into test specimens. The mechanical tests of these specimens should be performed at the HIP temperature, which is relatively high. The oxidation rates become excessive because of the large surface area due to the voids and the high temperature. Therefore, it is necessary to perform the mechanical tests in an inert environment.

To determine the shape of the yield surface several types of mechanical tests are required. Each type of test produces one point on the yield surface. There is one point on the surface that is known: the hydrostatic pressure of the HIP process. A compression test performed at temperature will provide a second point on the yield surface and will also provide some information on the elastic, hardening and plastic flow of the material. Tension tests performed at temperature, when compared to a compression test performed at temperature, will determine the symmetry of the yield surface. In addition, creep tension tests at the HIP temperature are desirable to determine accurately the creep properties of the partially dense metal powder. In Fig. 25, a compression, tension and creep specimen of powder metal is illustrated. Two partial HIP bars are required to construct all the test specimens illustrated in Fig. 25. The compression tests are the most important tests to be performed since they produce a hydrostatic pressure which is the predominant loading feature during a HIP cycle. Two deformation measures will be used to characterize the yield surface; the void volume fraction and the plastic (nonrecoverable) work. Therefore, the measurement of the axial length change is not sufficient to determine the mechanical response and a measurement of the volume will also be required. The final volume of a compression specimen can be measured after a completed test but this does not provide a complete description of the path to the final state.

Thirty compression tests were performed. Three of these tests were used to size the compression specimens and determine the test conditions. The remaining tests were all completed in a similar manner. Figure 26 illustrates the typical output. The specimens consisted of a right circular cylinder 0.5 in. long by 0.2 in. in diameter. Each specimen was placed in a furnace in an inert gas and brought up to the temperature at which the specimen was hot isostatically pressed. At temperature the specimen was subjected to compression crosshead displacement rate of 0.0025 in./min and the load was recorded. After the load leveled out, the cross-head rate was doubled to 0.005 in./min and after the load again leveled out, the crosshead displacement was fixed and the load recorded as a function of time.

Measurement of the dimensions of the compression specimens before and after testing, and a summary of the data is given in Table 5. The average values for the height, diameter, and volume changes are presented in Table 5 along with the standard deviations. From the last column in Table 6 it can be seen that over all the samples there was a significant decrease in the height and a significant increase in the diameter, while there was essentially no change in the volume.

A total of 14 tensile tests were completed and resulted in significantly lower yield stress values than the compression tests, especially at 2000 F. Table 7 is a summary of the compressive and tensile yield stress values calculated from the mechanical tests. The low tensile yield stresses could be a result of the presence of voids which would be adjacent to the particle interfaces. Tensile stresses, which are amplified at the void, would tend to separate the particles producing a smaller apparent yield than compression stresses which would tend to close the voids. The tensile test results were so low that it was determined to be impractical to perform the creep tests. Instead, use was made of the relaxation tests, performed during the compression testing, to determine the creep properties.

Additionally, three room temperature tensile tests were performed to determine if the MERL 76 material was contaminated. Table 8 summarizes the results. Note that three room temperature values were obtained 144, 102 and 138 ksi, with corresponding ultimate stresses of 168, 156 and 164 ksi, respectively. Fully densified MERL 76 generally yields at 145 ksi at room temperature indicating that partially densified specimens are representative of the fully densified material. Even though the value of 102 ksi is relatively low, it appears that the low yield stress of partially densified materials at high temperatures cannot be explained by contamination of the particle surfaces. Contamination would have reduced the strength to values well below the fully densified yield strength for MERL 76.

In Table 7, two compression tests demonstrated abnormally high values. Two of these tests were repeated with essentially the same results. An explanation for the high values should be found as higher yield stresses are desirable and this result may be related to the relatively low tensile stresses. Microscopic examinations did not yield any results that would indicate why these two specimens had high yield stresses or why the tensile specimens had low yield stresses.

Examination of the fracture surfaces of tensile samples using a scanning electron microscope has indicated that the partially dense specimens are not contaminated. The tensile specimens fractured at room temperature showed no evidence of oxidation of the particle surfaces and showed no evidence of any foreign material. The specimens fractured at 1800 F did show evidence of oxidation but this apparently occurred after the specimen was fractured, since there is no evidence of any oxidation in all room temperature partially dense material. Thus, the most probable explanation for the low yield stress at high temperatures is due to the presence of voids which will amplify the stresses present at the bonded particle interface. Ceramic inclusions significantly reduce the fatigue strength of hot isostatic pressed material as the temperature is increased, voids should act in a manner similar to the ceramic inclusions.

The uncertainty associated with the tensile test results necessitated the use of the experimental observation that the volume was conserved during compression. A comparison of the results of this observation with the results predicted by a symmetric yield surface,  $\alpha$  equal to zero in Eq. (9), is a test of the sensitivity of the assumption. Figure 27 displays either the analytical radial to axial strain rate ratio, or the experimental final ratio of radial strain to axial strain. Although there is scatter, Fig. 27 shows that assuming no volume change under uniaxial compression is a better assumption than assuming a symmetric yield surface.

#### Interpretation of Mechanical Test Results

The mechanical tests indicated that there is little or no volume change in compression. Coupling this fact with the hydrostatic pressure yield stress,  $P_y$ , and the compressive yield stress  $\sigma_c$  will determine all of the yield parameters in Eq. (9) as

$$\alpha = \sigma_c \quad (85)$$

$$\beta^2 = \frac{3}{q^2} \quad (86)$$

$$\sigma_o = \sigma_c \quad (87)$$

where

$$q = \frac{3 P_y}{\sigma_c} - 1 \quad (88)$$

The experimental results for the tensile yield stress,  $\sigma_T$ , were not reliable but can be determined from Eq. (9) as

$$\sigma_T = \left( \frac{q^2 - 1}{q^2 + 1} \right) \sigma_c \quad (89)$$

Normalizing the compressive yield stress data,  $\sigma_c$ , with respect to the initial powder particle yield stress,  $\sigma_y$  shows that this ratio is approximately a linear function of relative density as shown in Fig. 28, or

$$\frac{\sigma_c}{\sigma_y} = b \left( \frac{v_i - v}{1 - v_i} \right) \quad (90)$$

where

$P_y$  is evaluated from Eq. (61) by setting  $P$  equal to  $P_y$ ,

$v$  is void volume fraction

$v_i$  is initial void volume fraction, and

$b$  can be determined by requiring the tensile yield stress to vanish at the initial void volume fraction, or

$$\sigma_T = 0 \text{ at } v = v_i$$

From Eqs. (88) and (89), the above condition on  $b$  is

$$\lim_{v \rightarrow v_i} \frac{P_y}{\sigma_c} = \frac{2}{3} \quad (92)$$

Then from Eqs. (61) and (90)

$$b = \frac{C}{\tan^2 \theta} \quad (93)$$

where  $C$  and  $\theta$  are given by Eqs. (58) and (60) respectively.

The temperature,  $T$ , and strain rate,  $\dot{\epsilon}$ , dependence have been included in the initial particle yield stress,  $\sigma_y$ . A good fit occurs when

$$\sigma_y = \sigma_{y_0} e^{-\frac{T}{T_0}} \left[ 1 + \alpha \ln \left( \frac{\dot{\epsilon}}{\dot{\epsilon}_0} \right) \right] \quad (94)$$

for uniaxial stress conditions.

A good fit to the specimens partially densified in the HIP facility occurs if

$$\dot{\epsilon} \approx 0.00315/\text{min.}$$

The parameters in Eq. (94) are

$$\alpha_{y_0} = 1.074 \times 10^{10} \text{ ksi}$$

$$T_0 = 120.7 \text{ deg R}$$

$$\alpha = 0.03403, \text{ and}$$

$$\dot{\epsilon}_0 = 8.148 \times 10^8/\text{min}$$

Equations (85) through (94), are the plastic formulation included in the code, and are compared to the experimental measurements in Figs. 22, 28, and 29. The agreement is good if the volumetric creep under hydrostatic pressure is included, (Fig. 22). Volumetric creep will move points subject to HIP for more than 10 min (the solid symbols in Fig. 22) to the right of the line representing instantaneous plastic deformation.

All of the hardening quantities,  $\frac{\partial h}{\partial \eta}$  in Eq. (26), the elastic-plastic moduli,  $L_{ijkl}^{e-p}$  can now be determined

$$\frac{\partial h_1}{\partial \eta_1} = \frac{\partial \sigma_0}{\partial v} = - \left( \frac{b}{1-v_i} \right) \sigma_y \quad (95)$$

$$\frac{\partial h_2}{\partial \eta_1} = \frac{\partial \beta}{\partial v} = \frac{3 \sqrt{3}}{q^2 \sigma_c^2} \left( \sigma_c \frac{\partial P_y}{\partial v} - P_y \frac{\partial h_1}{\partial \eta_1} \right) \quad (96)$$

$$\frac{\partial h_3}{\partial \eta_1} = \frac{\partial \alpha}{\partial v} = - \left( \frac{b}{1-v_i} \right) \sigma_y \quad (97)$$

where

$$\frac{\partial P_y}{\partial v} = \frac{2}{3} \sigma_y \left[ -\frac{1}{v} + \frac{2}{v_i} \left( 1 - \frac{v}{v_i} \right) \ln v_i + \frac{av}{v_i^2} \right] \quad (98)$$

and  $a$  is defined in Eq. (62)

Although little work hardening was observed during the compression tests, it may have an influence on the final deformations, and therefore an approximate hardening law of the form of Eq. (99) below was assumed.

$$\sigma_c = b \left( \frac{v-v_i}{1-v_i} \right) \sigma_y \left[ 1 - a_1 e^{-a_2 w^P} \right] \quad (99)$$

where  $w^P$  is the plastic work,  $a_1$ ,  $a_2$  are constant work hardening parameters, and assuming Eq. (99) to hold

$$\frac{\partial h_2}{\partial \eta_2} = \frac{\partial \sigma_o}{\partial w^P} = b \left( \frac{v-v_i}{1-v_i} \right) \sigma_y a_2 a_i e^{-a_2 w^P} \quad (100)$$

$$\frac{\partial h_2}{\partial \eta_2} = \frac{\partial \beta}{\partial w^P} = \left( \frac{3\sqrt{3}}{q^2 \sigma_c} \right) p_y \frac{\partial h_1}{\partial \eta_2} \quad (101)$$

$$\frac{\partial h_3}{\partial \eta_2} = \frac{\partial \alpha}{\partial w^P} = b \left( \frac{v-v_i}{1-v_i} \right) \sigma_y a_1 a_2 e^{-a_2 w^P} \quad (102)$$

From the uniaxial compression tests it was noted that the compressive yield stress seems to level off at about 1.4 times the initial compressive yield stress and therefore the constant  $a_1$  is given by

$$a_1 = 0.286 \quad (103)$$

The constant  $a_2$  was found to vary with temperature approximately by the relation

$$\frac{1}{a_2} = \begin{cases} a_2 \left( \frac{T_c - T}{\Delta T_o} \right) & T \leq T_c \\ 0 & T \geq T_c \end{cases} \quad (104)$$

where  $\alpha_2 = 9090$  psi  
 $T_c = 2020$  F  
 $\Delta T_o = 420$  F

In Fig. 30 the analytical values of  $a_2$  are compared with the spread in experimental values. The large scatter in the parameter  $a_2$  with relative density made it difficult to obtain a relationship describing the parameter  $a_2$  as a function of relative density.

The elastic constants are required to complete the formulation but only Young's modulus can be derived from the compression test data. The Young's Modulus, E, was assumed to be a linear function of void volume fraction, v, and an exponential function of temperature, T, given below

$$E = E_1 e^{-\frac{T-T_0}{T_1}} \left( \frac{v_i - v}{v_i} \right) \quad (105)$$

where  $v_i$  is the initial void volume fraction, and  $E_1$ ,  $T_0$  and  $T_1$  were chosen to provide a good fit to the data, as

$$E_1 = 1.5 \times 10^6 \text{ psi}$$

$$T_0 = 1900 \text{ F}$$

$$T_1 = 163 \text{ F}$$

Figure 31 compares the analytical expression with the resulting mechanical test data. The comparison is within the experimental error. Since it was not possible to measure radial deflections during the testing it was assumed that the bulk modulus for the solid material,  $K_o$ , was not a function of temperature, and can be found from Eq. (105) as

$$K_o = \frac{E_1 e^{-\frac{T-T_0}{T_1}}}{3(1-2v)} = 7.88 \times 10^6 \text{ psi} \quad (106)$$

where  $v$  is Poisson's ratio.

For  $K_o$  to be a constant function of temperature, Poisson's ratio must be given by

$$v = \frac{1}{2} \left\{ 1 - \frac{E_1}{3 K_o} e^{-\frac{T-T_0}{T_1}} \right\} \quad (107)$$

if it assumed that  $v$  is 0.3 at 1600 F for all void volume fractions. Poisson's ratio is shown as a function of temperature in Fig. 32 using Eq. (107) and can be seen to approach 0.5 at temperatures near normal HIP operating conditions. In Appendix A the bulk modulus is derived as a function of Young's modulus, Poisson's ratio and void volume fraction, Eq. (A.16) by considering the elastic response of a spherical void within a large sphere as

$$K = \left[ \frac{E}{3(1-2v)} \right] / \left[ 1 + \frac{v}{2} \left( \frac{1+v}{1-2v} \right) \right] \quad (108)$$

where  $E$  and  $v$  are given by Eqs. (105) and (107). Figure 33 presents the bulk modulus as a function of void volume fraction and temperature and demonstrates a large variation with temperature and void volume fraction.

Only the deviatoric creep properties need to be defined, the volumetric creep has been discussed in this section. The deviatoric creep can be found from the results of the compression tests, since the volume of the specimens has been observed to be conserved. A good fit to the data was obtained by taking the deviatoric creep strain rate to be given by

$$\dot{\epsilon}^d = \frac{1}{t_0} \left( \frac{\sigma}{\sigma_0} \right)^n \quad (109)$$

$$\begin{aligned} \text{where } n &= 2 - \frac{v}{v_i} \\ t_0 &= a_0 e^{-\frac{T_0}{T}} e^{\gamma \rho} \\ a_0 &= 1.36 \times 10^{-3} \text{ sec} \\ T_0 &= 115000R, \text{ and} \\ \gamma &= 44.3 \end{aligned}$$

if  $\sigma_0$  is assigned the value 15 ksi. In Fig. 34 the time constant,  $t_0$ , is plotted as a function of density for various temperatures and is compared to the experimentally derived values. Note that the time constant changes an order of magnitude with a change of 5 percent in the relative density. In Fig. 35 the analytical approximation for the creep exponent compares favorably with the experimentally determined values.

At a relative density of 0.85 the volumetric and deviatoric creep strain rates are the same order of magnitude, but at the initial or final relative density the rates will differ by about three orders of magnitude.

## MODEL VERIFICATION

### Verification Criteria

The constitutive theory developed and supported by the mechanical tests of partial HIP samples were validated through a series of experiments. The validation test results were correlated with results of the numerical simulation of the experiment. Although a one-dimensional axisymmetric validation configuration would provide conditions analogous to those experienced in the actual HIP process.

The validation tests were designed to avoid duplication of the uniform hydrostatic stress state of the partial HIP tests. The experiments must therefore result in a nonvanishing shear stress within the sintered material. A nonhydrostatic stress state can be achieved with the application of the uniform external pressure if the material has nonhomogenous properties. This may be achieved by imbedding in the metal powder a different material, for example, steel or fully compacted powder spheres or cylinders. Such an experimental configuration will produce a nonhydrostatic stress state and will make use of existing hardware and techniques. Microscopic examinations could be used to determine the density as a function of position or in the case of buried steel spheres metal foil could be placed tangent to a sphere and the resulting displacements measured and compared to the predicted displacements.

An additional validation experiment could subject a partially dense bar to uniaxial compression. The bar could then be subjected to second HIP and the density measured. This test would follow a loading path not previously investigated and the final density could be used as a measure of the accuracy or limitations of the theory. This validation test though was deemed impractical because the scatter in the partial HIP experiments would require a large number of these tests to be performed to produce the same variation in stress state that would result from a much smaller number of experiments using spherical or cylindrical inclusions. Therefore, only the verification experiments based on spherical or cylindrical inclusions were considered.

### Spherical Inclusions

As an approximation to a spherical inclusion in a partially compacted powder consider the case of a rigid sphere buried in an infinite isotropic elastic solid. The compacting powder will have two elastic parameters, for example, Young's modulus and Poisson's ratio, which will be functions of position and will depend upon the stress history at the particular point in the powder. In turn the stress history will be a function of the loading and the boundary conditions. Appendix G of Ref. 10 presents the solution for the spatial stress distributions about a rigid sphere imbedded in an isotropic homogenous elastic solid of infinite extent and subjected to a hydrostatic pressure. Figure 36 presents a plot of the second invariant of the deviatoric stress tensor as a function of position from the center of a 0.5 in.

dia sphere. The radial change in the second invariant will result in every radial point exhibiting a different stress history and producing a different final density. Note from Fig. 36 that most of the variation will occur in a distance 0.25 in. from the surface of the sphere. Accurate measurements of density as a function of position would be required to validate the constitutive model with this experiment. The powder metal particle size is on the order of .002 to .007 in., and 0.25 in. variation should be more than sufficient to get an accurate representation of the density.

Initially the spheres may be buried in a very weak powder and it will be necessary to consider the effects of the sphere weight on the powder. A simple calculation (i.e., multiplying the fractional increase in weight density by the diameter of the sphere) shows the effect should produce a stress on the order of 1/30 psi or 1/500 of an atmosphere. This is relatively small compared to the applied pressures, and can be neglected.

#### Cylindrical Inclusions

Consider the case of a rigid cylindrical rod buried on an infinite homogenous elastic powder in a plane strain situation. The powder itself will have no resultant axial motion near the rod if it is bonded to the rigid rod. Appendix H, of Ref. 10, is a derivation of the response of a rigid cylindrical rod imbedded in a homogenous, isotropic elastic metal powder. Figure 37 presents a plot of the second invariant of the deviatoric stress as a function of position from the center of a 0.5 in. dia rod. The variation with position is a function of the square of the distance from the center of the rod. The maximum value obtained for the second invariant of the deviatoric stress is less for the cylinder than for the sphere. Most of the effects of the cylindrical inclusion will be negligible after a distance of about 0.5 in. from the center of the cylindrical rod.

Weight effects are more important for the cylindrical inclusions and are now on the order of 0.6 psi or about 1/20 atm. The effects of the weight should still be negligible when compared to the applied pressures.

The cylindrical inclusion problem in itself is not one-dimensional. At the ends of the rod a two-dimensional stress state exists because of the shear stresses set up between the powder metal and the initially rough rod. The resulting two-dimensional, axisymmetric stress distribution can be analyzed using the modified finite element program.

Note that if the solutions are extended to elastic spheres and rods, the stress distribution in the powder will depend only on the bulk modulus of the imbedded material. Therefore, if the imbedded material becomes fluid, it would respond in essentially the same manner as the solid material.

### Yield Surface Considerations

Consider the yield function Eq. (9) with  $\alpha$  equal to zero and  $\beta$  equal to one. Figure 38 presents the location of the yield point of the various mechanical tests on the yield surface, and includes the variation of the spherical and cylindrical inclusions near the yield surface. The region in which the validation experiment will lie is near the pure hydrostatic stress state where component manufacturing occurs. In addition, the spherical inclusions present more variation and are readily available in the form of ball bearings. For these reasons, and because the displacements could be measured by placing thin metal foil tangent to the sphere, the spherical inclusion was preferred.

### Plastic Analysis for Spherical Inclusions

Before proceeding with the verification experiments a finite element model of the experiment was analyzed using the modified MARC code. The model consisted of 7 axisymmetric elements illustrated in Fig. 39. Constraints were set to insure only spherically symmetric radial displacement would result. The steel sphere was modeled as rigid, and therefore the radial displacements were fixed in the powder at the surface of the steel sphere. The analysis considered only the plastic deformations that would result in raising the external pressure to 15 ksi. In Fig. 40, the model resulted in predictions that the void volume fraction decreased near the sphere or the density is highest near the sphere, and by an applied external pressure of 15 ksi all points in the specimen are more than 90 percent of full density. From Fig. 41 the predicted radial displacements can be seen to be nearly a linear function of the radial distance from the center of the sphere at sufficiently large distances, indicating that foil tangent to the sphere will appear flat at large distances from the sphere center. The deflections of the foil can be easily calculated using the radial displacements and are presented as a function of the distance from the center of the foil, as shown in Fig. 42. At about 8 ksi the edge of the foil should be nearly flat. These conditions had been run during the partial HIP tests and produced a relative density of about 0.85, which agrees with the predicted results presented in Fig. 40.

### Verification Results

The specimen design consists of a steel sphere imbedded in a sintered rod. A layer of nickel foil is placed tangent to the sphere. One, two, or three sphere and nickel foil configurations are placed within the sintered bar. Figure 43 illustrates a typical configuration. The first verification experiment consisted of a test to insure the configuration would HIP properly and was successfully completed.

Two sintered bars were hot isostatic pressed, based on the above success and the finite element results for a maximum of 10 min at 1800 F and 8 psi. These bars contained a total of five 0.25 in. diameter spheres. The first specimen

contained two spheres. When the specimen was divided in two axially it was apparent that the first sphere had slipped, as it was not centered on the original cut. The second sphere though was good, although the tapped hole was approximately 0.001 in. too deep and therefore the sphere contacted the foil directly. The foil displacements were measured where there was no contact and the experimental results were compared to numerical predictions, as shown in Fig. 44. The agreement was good but a range of only 0.002 in. of displacement could be measured out of a total of 0.009 in. and therefore there was no basis for verification of the theory. A second sintered bar containing three spheres was hot isostatic pressed under the same conditions. Two of these, spheres 3 and 4, appeared to have been pressed properly the last, sphere 5, had broken at the nickel foil. The experimental results for sphere 3 are compared to the analytical predictions in Fig. 45. Now the experimental range is 0.005 in. from the center of the foil. The lack of agreement near the center may be due to either the relative elasticity of the sphere and powder including thermal effects, which were not modeled, or due to the weight of the sphere. The rapid decrease in error with position indicates the error may be due to the elastic effects. The experimental results for sphere 4 are presented in Fig. 46, and compared to the analytical predictions. Again the fast variation at the foil center can be seen. The experimental results then agree with the numerical predictions for a short distance and rapidly fall off. For this particular sphere there was no contact between the powder and the foil on one side and no displacement measurements were taken. The side where measurements were taken may have initially only contacted out to 0.150 in. from the foil center producing the experimental results in Fig. 46. It should be pointed that the exact location of foil is accounted for in the theoretical results in Figs. 44 through 46 and therefore these curves are not the same.

The results of the verification experiments indicate that the plasticity theory developed can account for most of the short time response of powder metals. However additional experiments are required to fully verify the theory.

### HIP PROCESS SENSITIVITY STUDIES

The objective of this task is to develop a finite element methodology for the efficient modeling of shape changes in the HIP process. In this section the finite element analysis of the HIP process is described, variables in the analysis are identified, and the analysis for determining critical parameters and variables are reviewed.

The formulation of a finite element analysis requires the specification of a finite element mesh, material properties, external loads histories and boundary conditions. Additionally, since both material and geometric nonlinearities will be present, the finite element analysis must be incremental. Consequently an incrementing procedure must be established.

The geometry of a HIP configuration consists of a metal container which encapsulates a metal powder. For the applications considered in this program the geometry will be axisymmetric. The container is modeled with axisymmetric thin shell elements and the powder with axisymmetric ring elements. The MARC code possesses both ring and shell elements. The axisymmetric ring elements are the three node triangular element and the four and eight node isoparametric quadrilateral elements. For the thin shell element model of the container a two node axisymmetric membrane and bending element is used. The axisymmetric solid elements can be generated using the MARC two-dimensional mesh generator. The thin shells must be generated manually.

The container elastic, plastic and creep material properties are modeled using the finite strain analogs of the classical, incompressible plasticity and creep theories. Thus the container material is characterized in terms of its uniaxial plastic and creep response at HIP temperatures. These data have been developed separately from the this program, in Ref. 2. The powder constitutive model has been developed in this program.

In the HIP process three load types are present; gravity, the externally applied increasing pressure field and temperature loads. All three loads should be modeled. Experimental evidence from the HIP of full scale disks has shown that gravitational loads produce gross distortion of the HIP containers not adequately supported around their base. The pressure load applied to the internal surface of the container is the principal driving force for powder consolidation. Finally, the effects of possible inhomogeneous temperature distributions must be considered since container and powder material properties are temperature dependent. Thus the effects of temperature gradients should be investigated.

Displacement boundary conditions must be specified to complete the definition of the HIP configuration to be modeled. The boundary conditions which model the HIP container support are simply no motion in the vertical direction at the container base. The evolving boundary conditions between the container and powder are not presently understood. Initially the powder is free to move relative to the container except on the container lower horizontal surfaces where

the powder weight may be assumed to inhibit motion. As the temperature in the container and powder increase, differences in container and powder thermal expansion will result in either (1) a gap between the container sides and top, and the powder or (2) compressive stresses being exerted on the powder by the container. Irrespective of which of these conditions holds, it has been experimentally observed that at the end of the HIP process the container and powder are fused together. If there is an initial gap between the powder and container, the interior surfaces of the container walls and top are initially unsupported. The pressure loads are carried by the container alone causing the container walls to deform before contacting the powder. This nonuniform deformation in the container could contribute to nonuniformities in the final HIP geometry. Thus the closing of any gaps between the powder and container should be modeled using the gap element technology in the MARC code. If the container is always in contact with the powder, an approximation to the container-powder interface would be complete bonding for the entire HIP cycle. Such an approximation can be implemented by specification of multi-point constraints. In the analyses to follow it will be assumed that no gaps have formed.

After the input data for the HIP analysis were assembled an incremental analysis was performed. Thus increment sizes and increment convergence criteria were established. Increment size is controlled by the rate at which changes in material properties and geometry occur. Typically material properties change faster than the geometry so that it is unnecessary to account for geometry changes at every increment. The frequency with which the deforming geometry should be updated must be determined. Presently the MARC code does not allow for changing the frequency with which the geometry is updated.

An examination of the sensitivity of HIP finite element analysis will be now discussed. Parameters which were examined include:

1. Inclusion of powder creep deformations
2. The assumption that large strains are important
3. Temperature gradients in the powder
4. The effects of weight
5. Increment size and convergence criteria.

The two element parametric model, Fig. 47, was used to determine an efficient modeling strategy. The basic case consisted of a pressure loading only and produced a photographic reduction, (i.e., a proportional change in all the measurements.) A 50 F linear temperature difference was applied with the top of the model 25 F higher

than the mean of 1800 F and the bottom 25 F lower. There was no radial variation. At 15 ksi the bottom had a permanent radial displacement of 0.190 in. inward while the top moved 0.225 in. inward. This is a significant variation over a diameter of 4 in. Instrumentation can produce errors in temperature of this order and therefore the temperature distribution will have to be accurately controlled and modeled. The unsymmetric part of the stiffness moduli were then added to the case with a temperature variation and the displacement predictions changed by less than 0.5 percent. This was found to be generally true and it appears that this effect can be neglected. Although the model used should be relatively insensitive to the effects of weight, the addition of gravitational forces did produce a slight additional permanent radial displacement at the bottom, and further study with more sensitive structures should be considered. When the large strain terms in the numerical analysis were deleted, inaccurate results were produced; the permanent radial displacements were over predicted by six percent, a large error for an actual disk even though the modeled structure is relatively simple. Last, the effects of creep were added and at 2135 F the creep rate was high enough for the displacements to increase by  $1.5 \times 10^{-6}$  in. in 3 sec. due to the weight alone, about 0.5 psi, and therefore during an actual HIP the effects of creep must be accurately included. The effects of work hardening were not studied since the effect was judged to be slight and the errors in measurement too large.

To complete this task two additional models were developed: (1) a 65 element model of the F100 11th stage compressor disk with 44 container shell elements and 21 quadrilateral elements to represent the powder, Fig. 48, and (2) a model of the inside corner of the F100 disk with 10 quadrilateral elements and 14 shell elements to study the distortions at corners, Fig. 48.

The axisymmetric shell elements chosen to represent the container in the disk and corner models did not accurately represent the effects of large strains. However, these elements were able to bring the analysis to about half the initial void volume fraction. Currently there are no operational shell elements in the MARC code capable of modeling the HIP process. The MARC Analysis Research Corporation indicates more accurate elements should be available in the near future.

The corner model, of Fig. 48, showed that the displacements are considerably different for the finer mesh than the coarse model of the entire disk. The corner model had an initial void volume fraction of 0.340 upon termination of the analysis the void volume fraction varied from 0.009 far from the corner to 0.238 for the element in the corner. A significant variation that would not be predicted by the full disk model.

The full disk analysis began with the powder having an initial density of 0.340 and upon termination of the analysis the central element in Fig. 48, had a void volume fraction of 0.194 while element 1, an outer element, had a void volume fraction

of 0.315. In Fig. 49, the displaced shape, with the displacements amplified, readily shows the effects of weight loading. The displacements predicted were used to derive general expressions for the final positions  $(r, z)$  in terms of the initial positions  $(R, Z)$ . From Figs. 50 and 51 the initial and final positions were related by

$$r = 0.9919R + 0.00508 \quad (110)$$

and

$$z = 0.9798z + 0.0144 \quad (111)$$

Equation (110), and the finite element results, predict a growing of the radius of the inside hole and a shrinking of the outer radii, which was experimentally observed. Equations (110) and (111) predict contractions that are larger axially than radially which was also observed. At the point where analysis was terminated the difference in contraction ratios (i.e., one minus either of the coefficients of  $R$  and  $Z$ ) divided by the axial contraction ratio, 0.599, compares well with the value, 0.648, obtained from Ref. 2. All of these facts indicate that the analysis is proceeding correctly and that an accurate model of the HIP powder response has been generated.

REFERENCES

1. Anon: Manufacturing Methods for Superalloy Powder Production and Consolidation (1973). Air Force Contract F33615-73-C-5040.
2. Cheverton, K. J.: Analysis of Container Shape Change During Hot Isostatic Pressing. UTRC Report R79-217590, September, 1979.
3. Wilkinson, D. S. and M. F. Ashby: The Development of Pressure Sintering Maps. Sintering and Catalysis Materials Science Research, Vol. 10, G. C. Kuczynski, Ed., Plenum Press, p. 473-492 (1975).
4. Notis, M. R., R. H. Smoak and V. Krishnamachari: Interpretation of Hot Pressing Kinetics by Densification Mapping Techniques, *Ibid.*, p. 493-507.
5. Ramquist L.: Theories of Hot Pressing, Powder Metallurgy, Vol. 9, No. 17, p. 1-25 (1966).
6. Ashby, M. F.: A first Report on Deformation-Mechanism Maps. *Acta Metallurgica*, Vol. 20, p. 887-897 (1972).
7. Notis, M. R.: Pressure Sintering and Creep Deformation - A Joint Modeling Approach. *Powder Metallurgy International*, Vol. 6, No. 2, p. 82-84 (1974).
8. Torre, C.: Berg-Huttermann, Montash, Montan. Hochschule Loeben, Vol. 93 p. 62 (1948).
9. Green, R. J.: A Plasticity Theory for Porous Solids. *International Journal for Mechanical Sciences*, Vol. 14, p. 215-224 (1972).
10. Cassenti, B.N.: Interim Report on the Modeling of the Hot Isostatic Pressing Process. AFOSR-TR-79-1236, September, 1979,
11. Suh, N. P.: A Yield Criterion for Plastic, Frictional, Work-Hardening Granular Materials. *International Journal of Powder Metallurgy*, Vol. 5, p. 69-87 (1969).
12. Needleman, A.: Void Growth in an Elastic Plastic Medium, *Journal of Applied Mechanics*, Vol. 39, p. 964-970 (1972).
13. Shima, S. and M. Oyane: Plasticity Theory for Porous Metals, *International Journal of Mechanical Science*, Vol. 18, p. 285-291 (1976).
14. Kuhn, H. A. and C. L. Downey: Deformation Characteristics and Plasticity Theory of Sintered Powder Materials, *Internal Journal of Powder Metallurgy*, Vol. 7, p. 15-25 (1971).

REFERENCES (Cont'd)

15. Bodner, S. R. and Y. Partom: Constitutive Equations for Elastic-Visco Plastic Strain Hardening Materials. *Journal of Applied Mechanics, Transactions of the ASME*, June 1975, p. 385-389.
16. Corapcioglu, Y. and T. Uz: Constitutive Equations for Plastic Deformation of Porous Materials. *Powder Technology*, Vol. 21, 1978, p. 269-274.
17. Parks, D. M.: "Finite Deformation Plasticity Formulation for Compacting Metal Powders". *Communication to B. N. Cassenti*, dated March 25, 1979.
18. Hibbitt, H. D., P. V. Marcal and J. R. Rice: A Finite Element Formulation for Problems of Large Strain and Large Displacement, *International Journal of Solids and Structures*, Vol. 6, p. 1069-1086 (1970).
19. McMeeking, R. M. and J. R. Rice: Finite-Element Formulations for Problems of Large Elastic-Plastic Deformation. *International Journal of Solids and Structures*, Vol. 10, p. 321-339 (1974).
20. Prager, W.: *Introduction to Mechanics of Continua*, Ginn and Co., Boston (1961).
21. Nagtegaal, J. C. and J. E. deJong: Some Computational Aspects of Elastic-Plastic Large Strain Analysis. MARC Analysis Research Corporation, Palo Alto, California.
22. Penny, R. K. and D. L. Marriott: Design for Creep. McGraw Hill Book Co., New York (1971).
23. Wilkinson, D. S. and M. F. Ashby: Pressure Sintering by Power Law Creep. *Acta Metallurgica*, Vol. 23, 11/75, pp. 1277-1285.
24. Gurson, A. L.: Continuum Theory of Ductile Rupture by Void Nucleation and Growth: Part 1. Yield Criteria and Flow Rules for Porous Ductile Media. ERDA Contract E(11-1)-3084 Technical Report No. 39 (1975).
25. Mullins, M., M. Gadala and M. A. Dokainish: Effects of Void Separation and Strain Hardening on Porous Material Plasticity in Applications of Computer Methods in Engineering, Vol. 1, University of Southern California Press, p. 455-460 (1977).
26. Kuczynski, G. C.: Fundamentals of Sintering Theory in Powder Metallurgy for High Performance Applications. J. J. Burke and V. Weiss Editors, Syracuse University Press, p. 101-117 (1972).

REFERENCES (Cont'd)

27. Johnson, D. L.: Recent Developments in the Analysis of Sintering Kinetics, *Ibid*, p. 139-149.
28. Burke, M. A.: Applications of the Finite Element Method to the Study of Plastic Instabilities in Tension. Ph.D. Dissertation, Stamford University (1977).
29. Cassenti, B. N.: The Manufacture of Disks by the Hot Isostatic Pressing Process, AIAA Paper No. 80-1111. AIAA/SAE/ASME 16th Joint Propulsion Conference, June 30 - July 2, 1980, Hartford, Connecticut.
30. Lubkin, J. L.: Contact Problems. In Handbook of Engineering Mechanics, W. Flugge, editor, McGraw Hill, 1962.
31. Waterhouse, R. B.: Fretting Corrosion. Pergamon 1972.
32. Johnson, K. L.: An Experimental Determination of the Contact Stresses between Plastically Deformed Cylinders and Spheres. In Engineering Plasticity. J. Heyman and F. A. Leckie Editor, Cambridge University Press, p. 341-361, 1968.
33. Francis, H. A.: Phenomenological Analysis of Plastic Spherical Indentation. ASME Journal of Engineering Materials and Technology. p. 272-81, 1976.
34. Anonymous: MARC:CDC Nonlinear Finite Element Computer Program, Vols. 1-3, Control Data Corporation (1977).
35. Rice, J. R., and D. M. Tracey: Computational Fracture Mechanics. In the Proceedings of the Symposium on Numerical and Computer Methods in Structural Mechanics, Urbana, Illinois, 1971, edited by S. J. Fenuchs, pp. 585-623, Academic Press, New York, 1973.
36. Parks, D.: Private Communication of March 9, 1980.

## APPENDIX A

## HARDENING PARAMETER RELATIONSHIPS

Take as the two deformation parameters the void volume fraction and the plastic work, or

$$\eta_1 = v \quad (A.1)$$

and

$$\eta_2 = W^P = \int_0^t \sigma_{ij} D_{ij}^P dt \quad (A.2)$$

In classical volume preserving plasticity theory using either the plastic work or the effective plastic strain produces exactly the same result. The plastic work, or equivalently the inelastic energy dissipation has been used previously to describe nonlinear material response, for example, in Refs. 15 and 16.

The quantities  $k_\alpha$ , Eq. (14) must now be determined from  $\eta_1$ . Parks, in Ref. 17 has shown that the void volume fraction rate from Eq. (14), can be described by considering a mass of powder  $m$ , occupying volume,  $V$  where

$$V = V_{\text{void}} + V_{\text{solid}} \quad (A.3)$$

Then the void volume fraction,  $v$ , is given by

$$v = \frac{V_{\text{void}}}{V} \quad (A.4)$$

The mass can be expressed as

$$m = \rho_v V = \rho_{\text{solid}} V_{\text{solid}} \quad (A.5)$$

where  $\rho_v$  is the apparent density,  
 $\rho_{\text{solid}}$  is the density of a powder particle.

Then the relative density (i.e., the bulk density to fully consolidated density ratio) is simply

$$\rho = \frac{\rho_v}{\rho_{\text{solid}}} \quad (A.6)$$

R80-944374-13

From Eqs. (A.4) and (A.5)

$$m = \rho_{solid} V(1-v) \quad (A.7)$$

Since

$$\dot{m} = 0$$

then in Eq. (A.5)

$$\dot{\rho} = -\rho D_{kk} \quad (A.8)$$

Also

$$D_{kk} = \frac{\dot{V}}{V} \quad (A.9)$$

Taking the derivative of Eq. (A.7) and using Eq. (A.8)

$$\dot{v} = (1-v) D_{kk} + \frac{\dot{\rho}_{solid}}{\rho_{solid}} \quad (A.10)$$

Note that

$$\frac{\dot{\rho}_{solid}}{\dot{\rho}_{solid}} = -D_{kk}^{solid} \quad (A.11)$$

and assume that

$$D_{kk} = D_{kk}^p + D_{kk}^e \quad (A.12)$$

Then substituting Eqs. (A.11) and (A.12) into Eq. (A.10)

$$\dot{v} = (1-v) [D_{kk}^p + (D_{kk}^e - D_{kk}^{solid})] \quad (A.13)$$

$$|D_{kk} - D_{kk}^{\text{solid}}| \ll |D_{kk}^P| \quad (\text{A.14})$$

by considering a sphere of outer radius  $b$ , containing a central void of radius  $a$ . The outward elastic displacement of the outer radius of the sphere when subjected to an external hydrostatic pressure,  $P$ , and no internal pressure is given by

$$u = -\frac{(1-2v)Pb}{E} \left[ 1 + \frac{(1+v)v}{2(1-2v)} \right] \quad (\text{A.15})$$

where  $v = \left(\frac{a}{b}\right)^3$  is the void volume fraction

$v$  = Poisson's Ratio of the solid material

$E$  = Young's Modulus of the solid material

The apparent elastic volume change per unit volume is then given by

$$\frac{\Delta V}{V} = \frac{4\pi b^2 u}{\frac{4}{3}\pi b^3} = \frac{-3(1-2v)P}{E} \left[ 1 + \frac{v}{2} \left( \frac{1+v}{1-2v} \right) \right] \approx D_{kk}^e \Delta t \quad (\text{A.16})$$

The volume change of the solid particles per unit volume is

$$\frac{\Delta V}{V} = \frac{-3(1-2v)P}{E} \approx D_{kk}^{\text{solid}} \frac{\Delta t}{\Delta t} \quad (\text{A.17})$$

then

$$D_{kk}^e - D_{kk}^{\text{solid}} = \left[ \frac{1-D_{kk}^{\text{solid}}}{\frac{D_{kk}^e}{\Delta t}} \right] D_{kk}^e$$

Substituting Eqs. (A.16) and (A.17) into Eq. (A.18)

$$D_{kk}^e - D_{kk}^{\text{solid}} = \left[ \frac{\left( \frac{1-2v}{2} + \frac{1+v}{2} \right)_v}{\left( \frac{1-2v}{2} + \frac{1+v}{2} \right)_v} \right] D_{kk}^e \quad (\text{A.19})$$

The term in the brackets is proportional to the void volume fraction and varies between zero and one. Therefore, for porous metal subjected to a hydrostatic pressure

$$\int_0^t (D_{kk}^e - D_{kk}^{\text{solid}}) dt \approx \frac{vP}{k} \quad (\text{A.20})$$

where  $K = \frac{E}{3(1-2v)}$  is the bulk modulus

The plastic part is

$$\int_0^t D_{kk}^p dt \approx v \quad (\text{A.21})$$

For a pressure of 15 ksi, and a bulk modulus of  $25 \times 10^6$  ksi. The ratio of the integrals in Eqs. (A.20) and (A.21) is about 0.0006 and therefore the error introduced by neglecting  $D_{kk}^e - D_{kk}^{\text{solid}}$  with respect to  $D_{kk}^p$  should be less than 0.1 percent.

Therefore assuming that

$$D_{kk}^e \approx D_{kk}^{\text{solid}} \quad (\text{A.22})$$

Eq. (A.13) becomes

$$\dot{\eta}_1 = \dot{v} = (1-v)D_{kk} = \lambda k_1 \quad (\text{A.23})$$

Applying the normality condition, Eq. (14)

$$\dot{\eta}_1 = \dot{v} = \dot{\lambda} (1-v) \frac{2}{3} \beta^2 (I_1 + \alpha) \quad (\text{A.24})$$

and therefore

$$k_1 = \frac{2}{3} (1-v) \beta^2 (I_1 + \alpha) \quad (\text{A.25})$$

The second deformation measure, plastic work rate,  $w^p$ , is simply given by

$$\dot{\eta}_2 = \dot{w}^p = \sigma_{ij} D_{ij}^p = \dot{\lambda} k_2 \quad (A.26)$$

and from Eq. (14)  $\dot{\eta}_2 = \dot{w}^p = \dot{\lambda} \left( \frac{2}{3} \sigma_o^2 \right)$

$$k_2 = \frac{2}{3} \sigma_o^2 - \frac{2}{9} \beta^2 \alpha (I_1 + \alpha) \quad (A.27)$$

The total observed volume change rate is

$$D_{kk} = D_{kk}^p + D_{kk}^e \quad (A.28)$$

and the response due to the solid material is simply

$$D_{kk}^s = \frac{(1-2\nu_s)}{E_s} \dot{\sigma}_{kk} \quad (A.29)$$

where  $E_s$  and  $\nu_s$  are the elastic constants of the solid particles.

Substituting Eqs. (A.28) and (A.29) into Eq. (A.13) gives

$$\dot{v} = (1-v) [D_{kk} - \frac{(1-2\nu)}{E_s} \dot{\sigma}_{kk}] \quad (A.30)$$

Equation (A.30) is used in MARC code modifications so that the void volume fraction rate will decrease as the hydrostatic yield increases.

TABLE 1

TASKS AND SUBTASKS FOR MODELING THE HOT ISOSTATIC  
PRESSING PROCESS

Task 1:	Constitutive Model Development
1.1	Yield Surface Determination
1.2	Deformation and Time Hardening
1.3	Flow Rule Development
1.4	Creep Effects
-----	-----
Task 2:	Code Modifications
2.1	Code Familiarization
2.2	Numerical Strategy Definition
2.3	Code Modifications
2.4	Code Modification Verification
-----	-----
Task 3:	Material Properties Determination
3.1	Partial HIP Experiments
3.2	Mechanical Tests
3.2.1	Elevated Temperature Compression Testing
3.2.2	Elevated Temperature Tension Testing
3.2.3	Creep Testing
-----	-----
Task 4:	Constitutive Theory Verification
4.1	Verification Design and Analysis
4.2	Verification Experiment
4.3	Correlation
-----	-----
Task 5:	HIP Process Sensitivity Study
Annual Report	
Final Report	

TABLE 2

VALUES OF  $f(x)$ , Eq. (63)

$x$	$f(x)$
0.00	0.000
0.50	0.051
0.10	0.103
0.15	0.156
0.20	0.211
0.25	0.268
0.30	0.326
0.35	0.387
0.40	0.449
0.45	0.514
0.50	0.582

$x$	$f(x)$
0.50	0.582
0.55	0.653
0.60	0.728
0.65	0.806
0.70	0.889
0.75	0.979
0.80	1.075
0.85	1.181
0.90	1.300
0.95	1.441
1.00	1.645

TABLE 3  
POTENTIAL STRUCTURAL ANALYSIS CODES

Code Name	Author	Analysis Capabilities					
		Static	Plastic	Creep	Axisymmetric Continuum	Axisymmetric Shell	Large Strain Updated Lagrangian
ADINA	Bathe	Yes	Yes	Yes	Yes	Yes	No
HONDO	Key	No	Yes	Yes	Yes	No	Yes
FIPAX	Osias	Yes	Yes	No	Yes	No	Yes
PLANS	Armen	Yes	Yes	Yes	Yes	No	No
MARC	MARC Corporation	Yes	Yes	Yes	Yes	Yes	Yes
ANSYS	Swanson Analysis Systems, Inc.	Yes	Yes	Yes	Yes	Yes	No
NON-NISA	Engineering Mechanics Research Corporation	Yes	Yes	No	Yes	No	No*
NERSAP	Lockheed	Yes	Yes	Yes	Yes	Yes	No*

\*Total Lagrangian Formulation

TABLE 4  
TEST CONDITIONS FOR  
PARTIAL HIP EXPERIMENTS

All specimens preheated for 12 hrs at 2000 F and 1 atm

Exp. No.	Specimen No.	Conditions			Final Relative Density
		Temp., F	Time, min.	Pressure, ksi	
1	-	2135	20	5	1.000
2	-	2135	10	2.5	0.994
3	-	2135	10	1	1.000
4	-	1800	10	1	0.746
5	-	1600	10	15	0.706
6	-	1600	10	1	0.719
7	1002,03	1800	10	4	0.794,0.798
8	1004,05	2000	10	15	0.990,0.984
9	1006,07	1800	10	8	0.891,0.822
10	1008,09	1800	10	6	0.809,0.861
11	1010,11	1800	10	10	0.902,0.909
12	1012,NG	2000	10	4	0.984,leaked
13	1017,18	1800	10	15	0.863,0.922
14	1019,20	2000	10	2	0.852,0.934
15	1021,NG	2000	10	4	0.955,leaked
16	1031,32	2000	10	3	0.819,0.949
17	1043,44	1900	10	4	0.894,0.905
18	1059,60	1800	60	4	0.887,0.933
19	1061,62	1600	10	10	0.758,0.743
20	1067,68	1600	10	8	0.756,0.756
21	1068,70	1900	10	2	0.767,0.832
22	1071,72	1800	30	8	0.912,0.817
23	1073,74	1800	30	4	0.881,0.883
24	1089,90	1600	60	10	0.806,0.812
25	1091,92	1600	60	8	0.800,0.763
26	1098,99	1800	120	4	0.900,leaked
27	1100,01	1600	120	8	0.765,0.811
28	1102,0	1800	240	4	0.881,0.963
29	1106,07	2000	30	2	1.000,0.936
30	1108,09	2000	60	2	1.000,1.000
-	NG,NG	1600	10	15	both leaked
-	NG,NG	1600	10	15	both leaked
-	NG,NG	1600	120	8	both leaked
-	Sintered Only	-	-	-	0.707,0.686, 0.705

TABLE 5  
RESULTS OF COMPRESSION TESTS

Specimen No.	HIP Conditions			Initial			Geometry		Final Vol.	
	Maximum Pressure, ksi	Temp., F	Max., Min.	Height, in.	Dia., in.	Height, in.	Dia., in.	Dia., in.	Initial Vol.	
1002	4	1800	10	0.503	0.202	0.438	0.215	0.210	0.986	0.941
1004	15	2000	10	0.502	0.204	0.475	0.212	1.021		
1006	8	1800	10	0.5025	0.204	0.475	0.208		0.982	
1009	6	1800	10	0.503	0.204	0.477	0.210	1.005		
1011	10	1800	10	0.502	0.2045	0.478	0.209		0.995	
1018	15	1800	10	0.503	0.2045	0.4595	0.212		0.984	
1020	2	2000	10	0.503	0.2025	0.466	0.210	0.996		
1021	4	2000	10	0.5025	0.204	0.469	0.212	1.008		
1032	3	2000	10	0.503	0.203	-	-	-		
1044	4	1800	10	0.503	0.2025	0.473	0.208	0.992		
1060	4	1800	60	0.502	0.203	0.454	0.214	1.005		
1061	10	1600	10	0.503	0.200	0.475	0.205	0.992		
1067	8	1600	10	0.503	0.199	0.485	0.203	1.003		
1071	8	1800	30	0.502	0.203	0.475	0.210	1.012		
1074	4	1800	30	0.502	0.203	0.478	0.209	1.009		

R80-944374-13

TABLE 6

STATISTICAL GEOMETRY CHANGES FOR  
COMPRESSION TESTS

<u>Ratio, Final/Initial</u>	Mean <u>m</u>	Std. Dev. <u>s</u>	<u><math>\frac{m-1}{s}</math></u>
Height	0.9345	0.029	-2.25
Diameter	1.0330	0.010	3.31
Volume	0.9975	0.015	-0.17

TABLE 7  
YIELD STRESS RESULTS

Spec. No.	Rel. Density	Temp F	HIP Press. (ksi)	Time (m)	Yield Stress (ksi)			$\dot{\epsilon} = 0.005/\text{m}$	$\dot{\epsilon} = 0.010/\text{m}$
					Tension	Compression	Tension		
1002	0.794	1800	4	10	6.470	10.94	12.580	13.12	
1004	0.990	2000	15	10	.022	3.82	.036	5.19	
1006	0.891	1800	8	10	11.860	15.29		18.20	
1009	0.809	1800	6	10		36.70	13.120	39.76	
1011	0.909	1800	10	10		9.14		10.98	
1018	0.922	1800	15	10	2.875	17.38	4.960	20.73	
1020	0.934	2000	2	10	.029	2.32	.208	3.57	
1021	0.955	2000	4	10		2.59		3.97	
1032	0.949	1900	3	10	.252	9.10	.395	11.57	
1044	0.905	1900	4	10	.298	5.59	.521	7.76	
1060	0.933	1800	4	60	1.024	18.52	-	22.84	
1061	0.758	1600	10	60	> 7.979	24.52	-	26.75	
1067	0.756	1600	8	10		23.15		25.08	
1070	0.832	1900	2	10		6.40		7.96	
1071	0.912	1800	8	30	2.228	18.83	3.666	22.22	
1074	0.883	1800	4	30		13.58		16.66	
1090	0.812	1600	10	60		44.72		48.75	
1091	0.800	1600	8	60		40.36		47.70	
1098	0.900	1800	4	120	.126	11.89	.180	15.24	
1101	0.811	1600	8	120		47.70		50.15	
						{ 39.38		{ 42.46	
						{ (43.07)		{ (47.38)	
1103	0.963	1800	4	240		3.23	-	6.15	
1106	1.000	2000	2	30	.036	3.60	.341	5.13	
1108	1.000	2000	2	60	.252		-		
1112	0.988	1800	8	120	7.908				
1115	0.984	1800	8	240		{ 40.74		{ 44.44,	
						{ (41.35)		{ (45.67)	

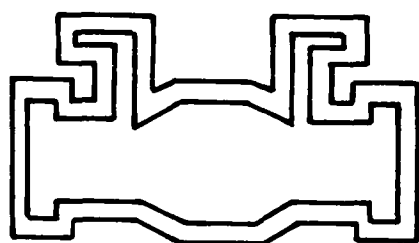
TABLE 8

## RESULTS OF ROOM AND HIGH TEMPERATURE TENSILE TESTS

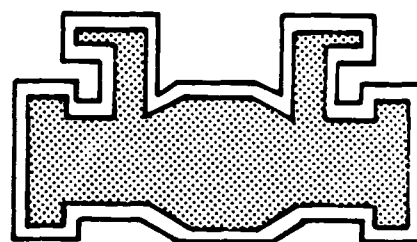
Specimen No.	Relative Density	Room Temperature Yield Stress (ksi) 0.2 Percent	Room Temperature Ultimate Stress (ksi)	Yield Stress (ksi) at 1800 deg. F
1004	0.990	144	168	0.022
1098*	0.900	-	82.4	0.126
1114	0.977	102	156	2.30
1115	0.984	138	164	-

\* Failed in grip

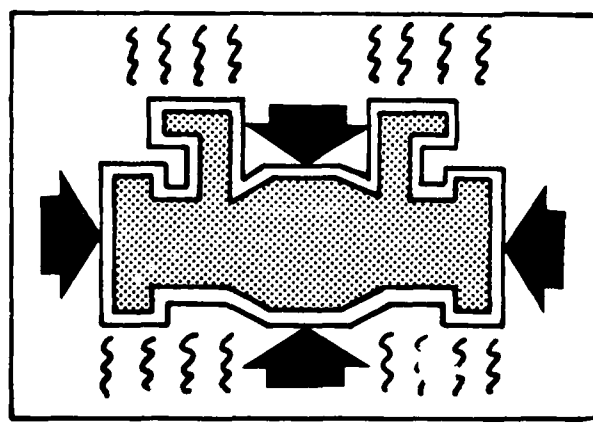
SCHEMATIC OF HIP PROCESS



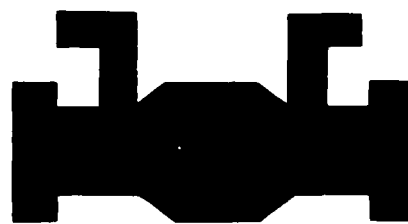
FABRICATED MOLD



FILL WITH POWDER, EVACUATE



HOT ISOSTATIC PRESS



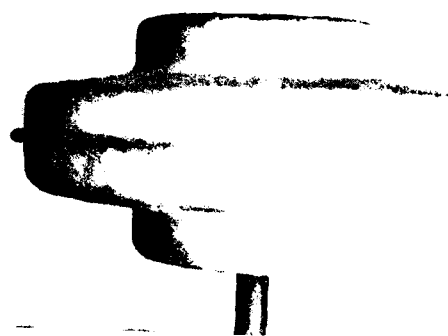
FINISHED PART

R80-944374-13

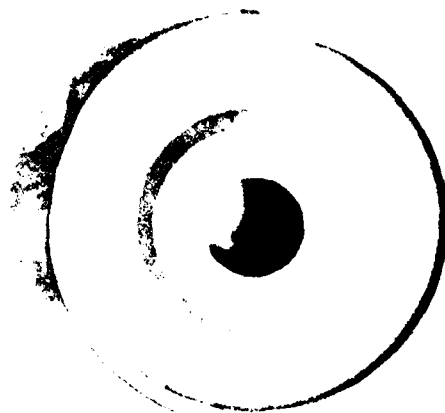
FIG. 2

### SAMPLE HIP COMPONENT

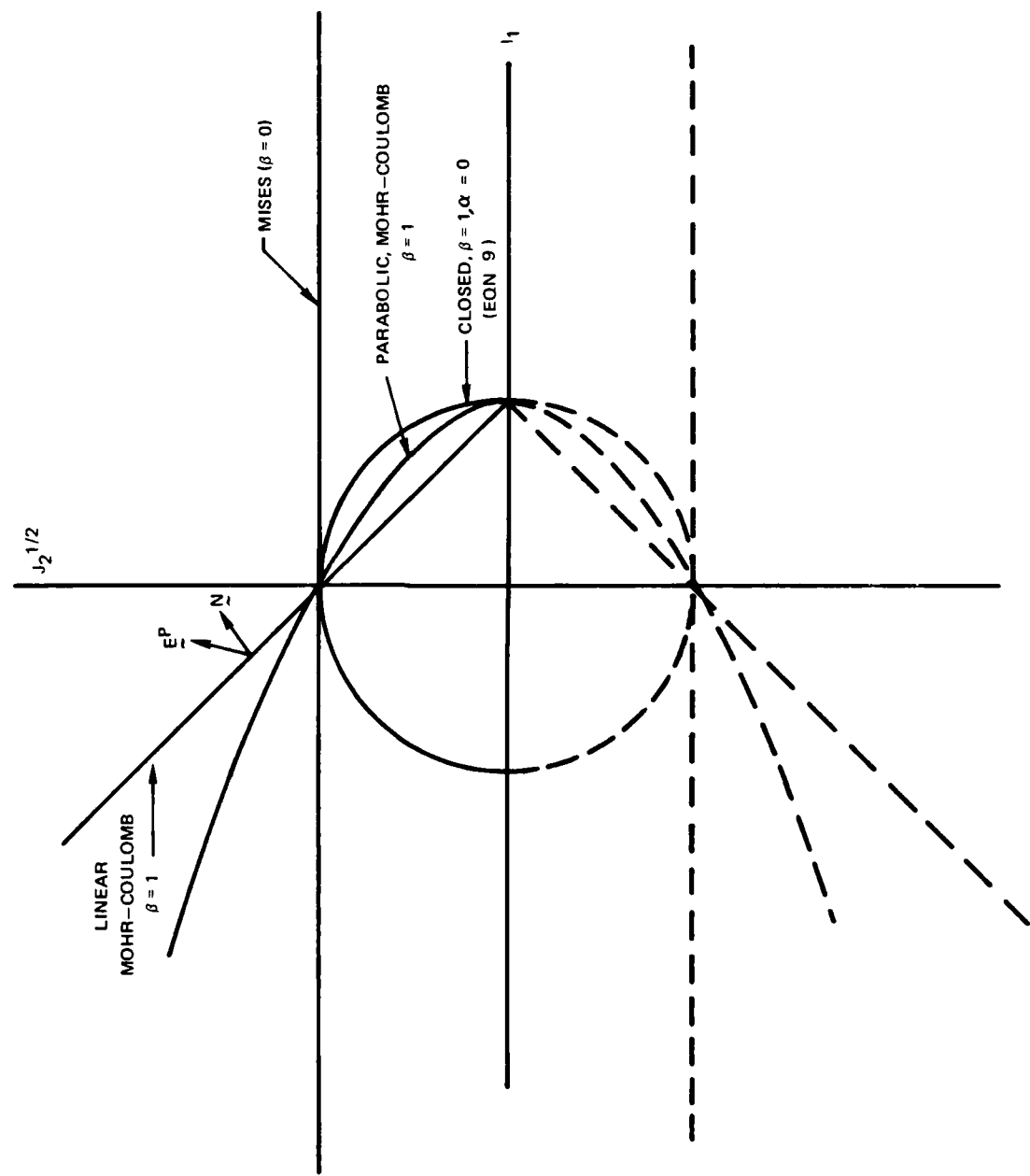
a) SAMPLE HIP CONTAINER



b) FINAL PART



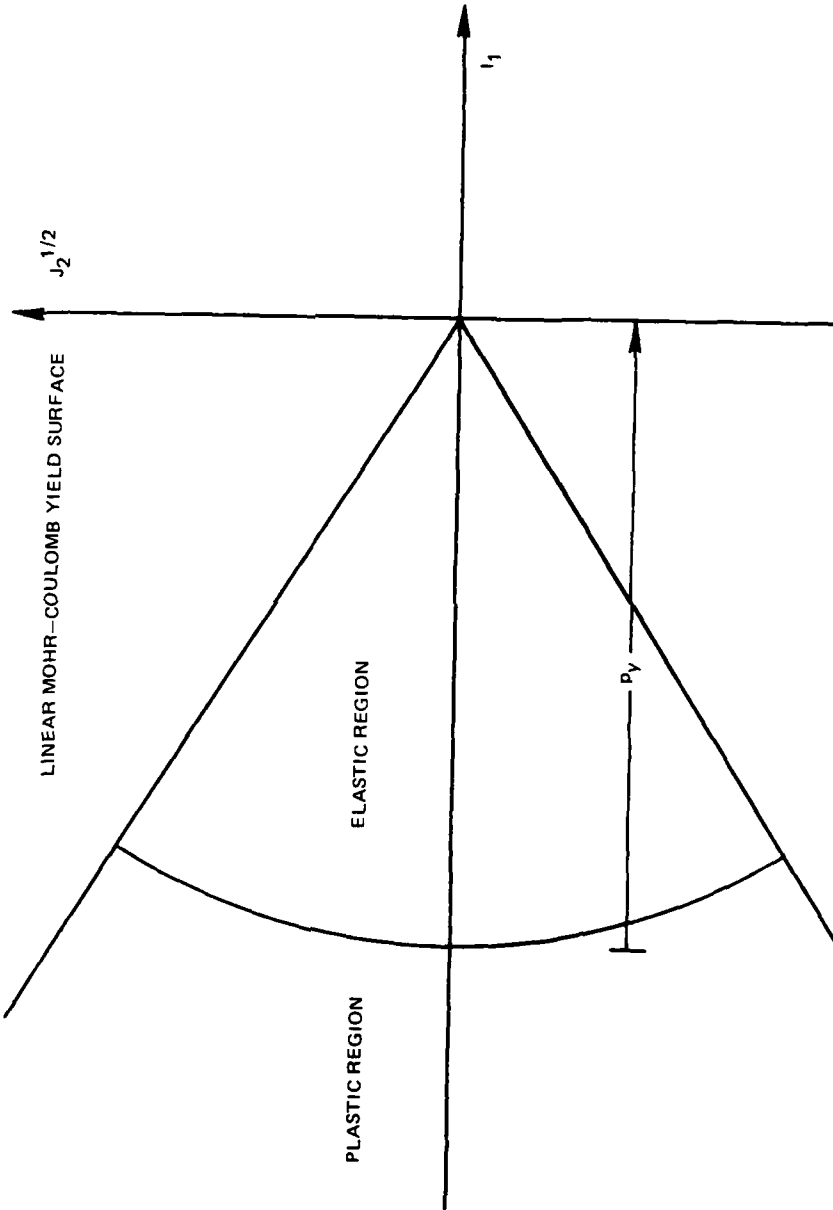
79-08-76-10

COMPARISON OF YIELD SURFACES IN  $I_1, J_2^{1/2}$  SPACE

R80-944374-13

FIG. 4

LINEAR MOHR-COULOMB YIELD ENVELOPE MODIFIED  
TO INCLUDE YIELD UNDER HYDROSTATIC PRESSURE



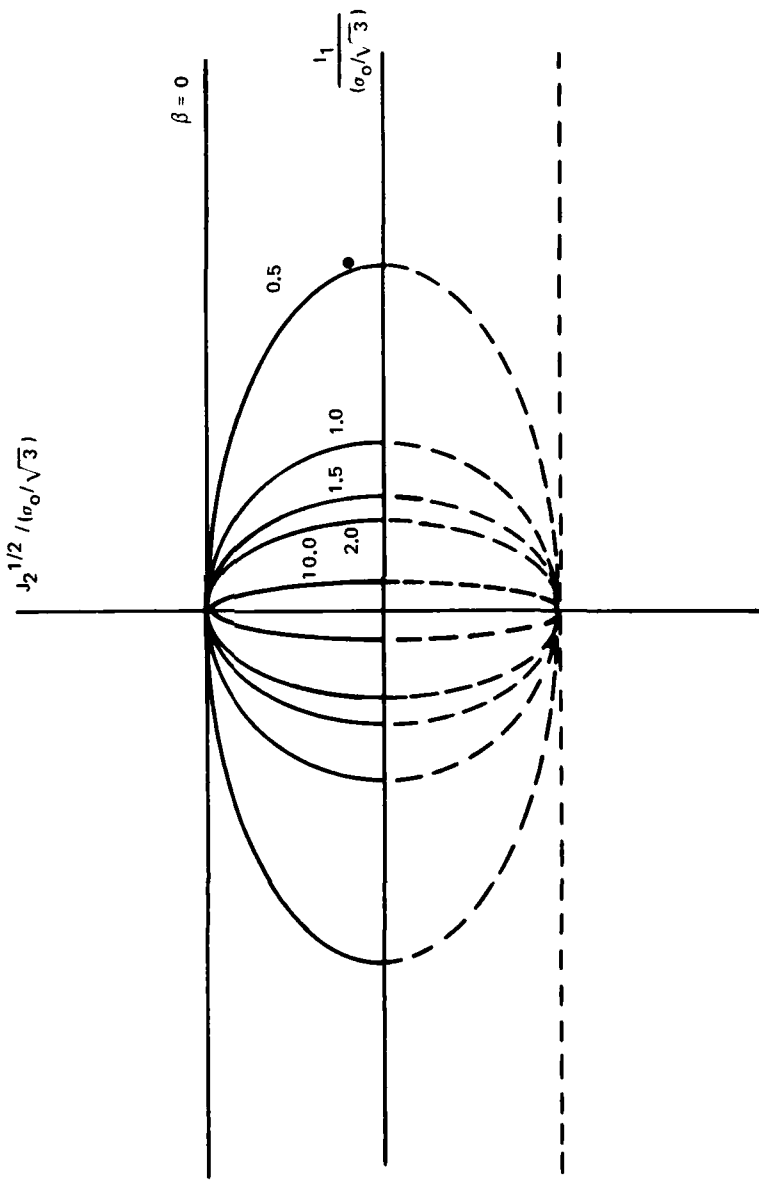
78-01-200-3

R80-944374-13

FIG. 5

ASSUMED YIELD SURFACE IN  $I_1, J_2^{1/2}$  STRESS SPACE FOR  $\alpha = 0$

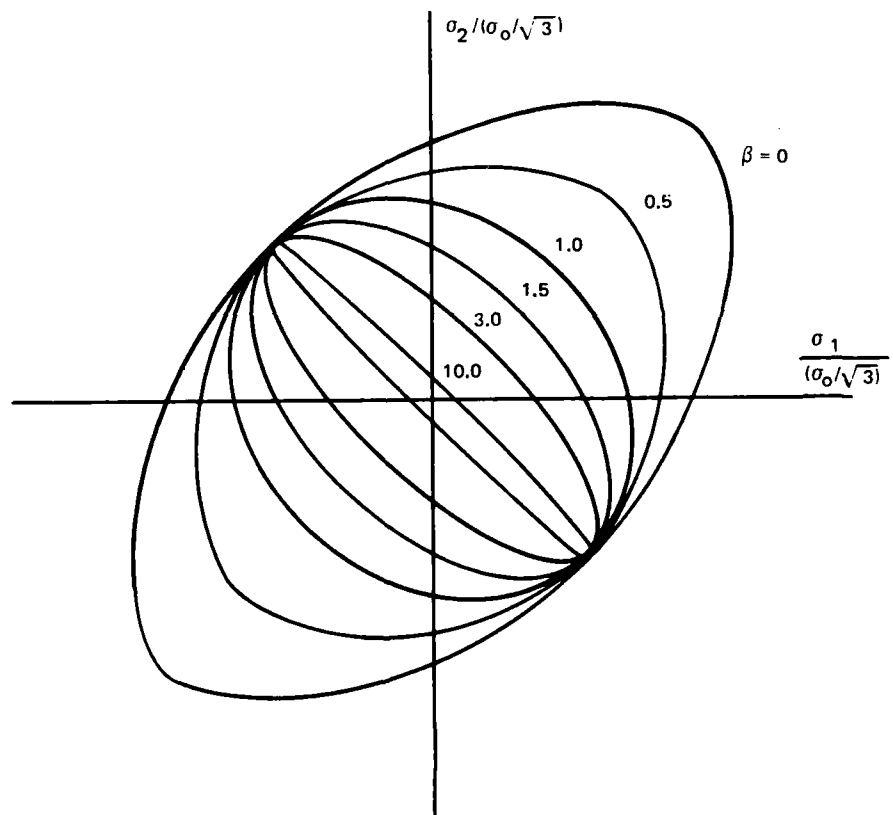
$$\beta^2 \left( \frac{I_1 + \alpha}{3} \right)^2 + J_2 = \frac{\sigma_0^2}{3}$$



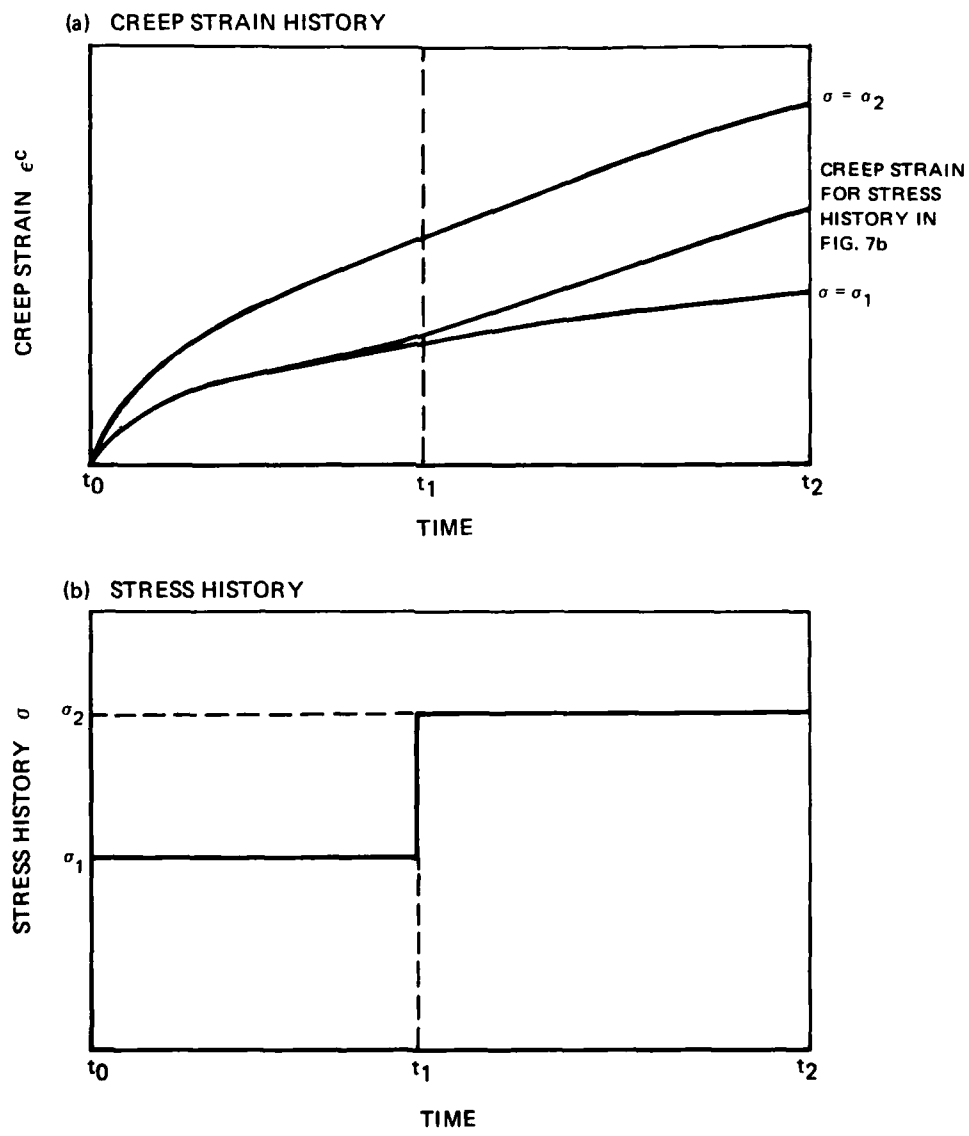
7B-01-200-1

ASSUMED YIELD SURFACE IN PRINCIPAL STRESS SPACE FOR  $\sigma_3 = 0, \alpha = 0$ 

$$\beta^2 \left( \frac{\sigma_1 + a}{3} \right)^2 + J_2 = \frac{\sigma_0^2}{3}$$

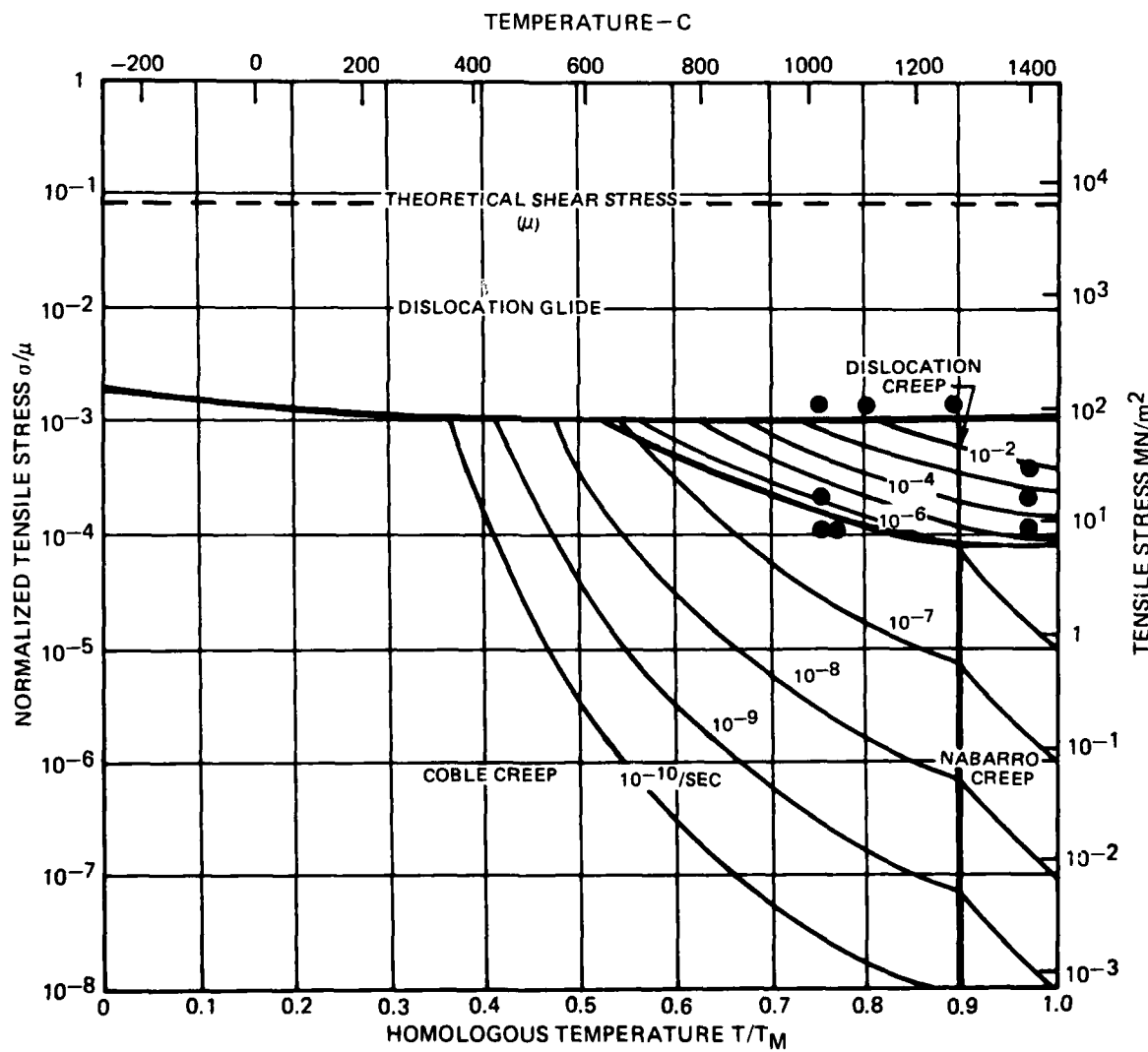


## TIME HARDENING MODEL OF CREEP STRAIN PREDICTION



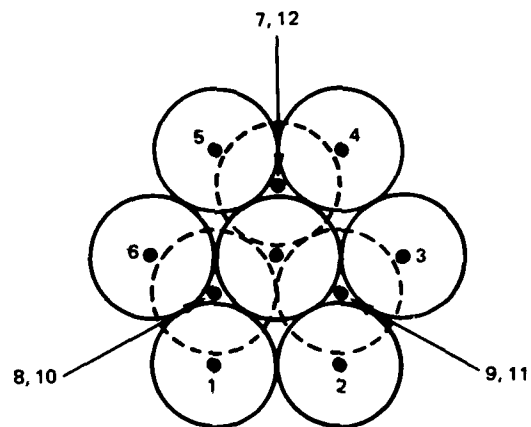
**LOCATION OF MERL 76 PARTIAL HIP CONDITIONS  
ON CREEP DEFORMATION MAP FOR NICKEL**

● MERL 76 PARTIAL HIP EXPERIMENTS



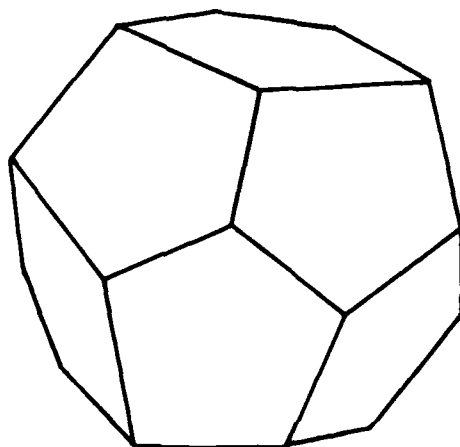
**HEXAGONALLY CLOSE PACKED SPHERES MODEL**

## (a) GEOMETRIC CONFIGURATION

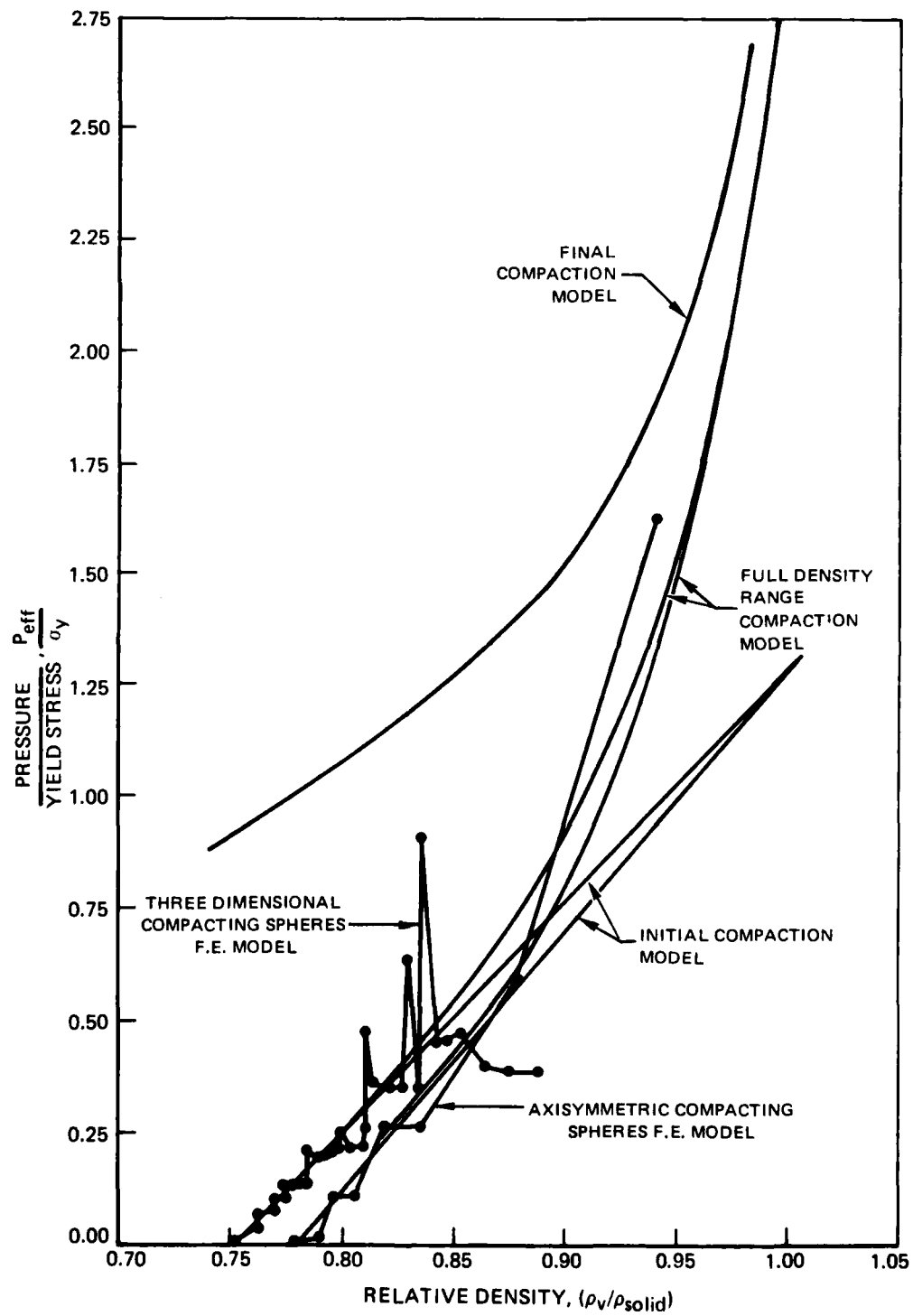


SPHERES 1 – 12 ALL CONTACT THE CENTRAL SPHERE  
SPHERES 1 – 6 LIE IN THE PLANE OF THE CENTRAL SPHERE  
SPHERES 7 – 9 ARE BELOW THE CENTRAL SPHERE  
SPHERES 10 – 12 ARE ABOVE THE CENTRAL SPHERE

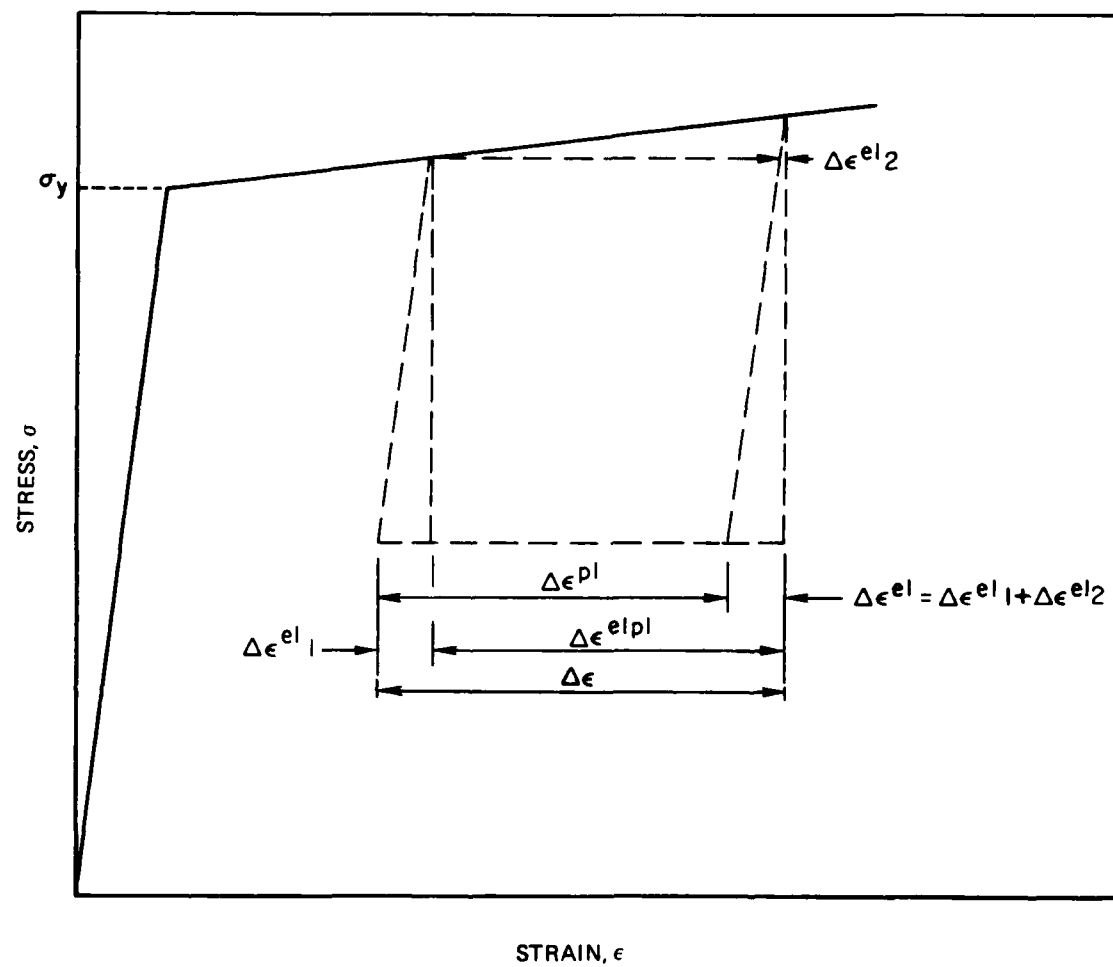
## (b) SPHERICAL PARTICLE DEFORMED INTO A REGULAR DODECAHEDRON



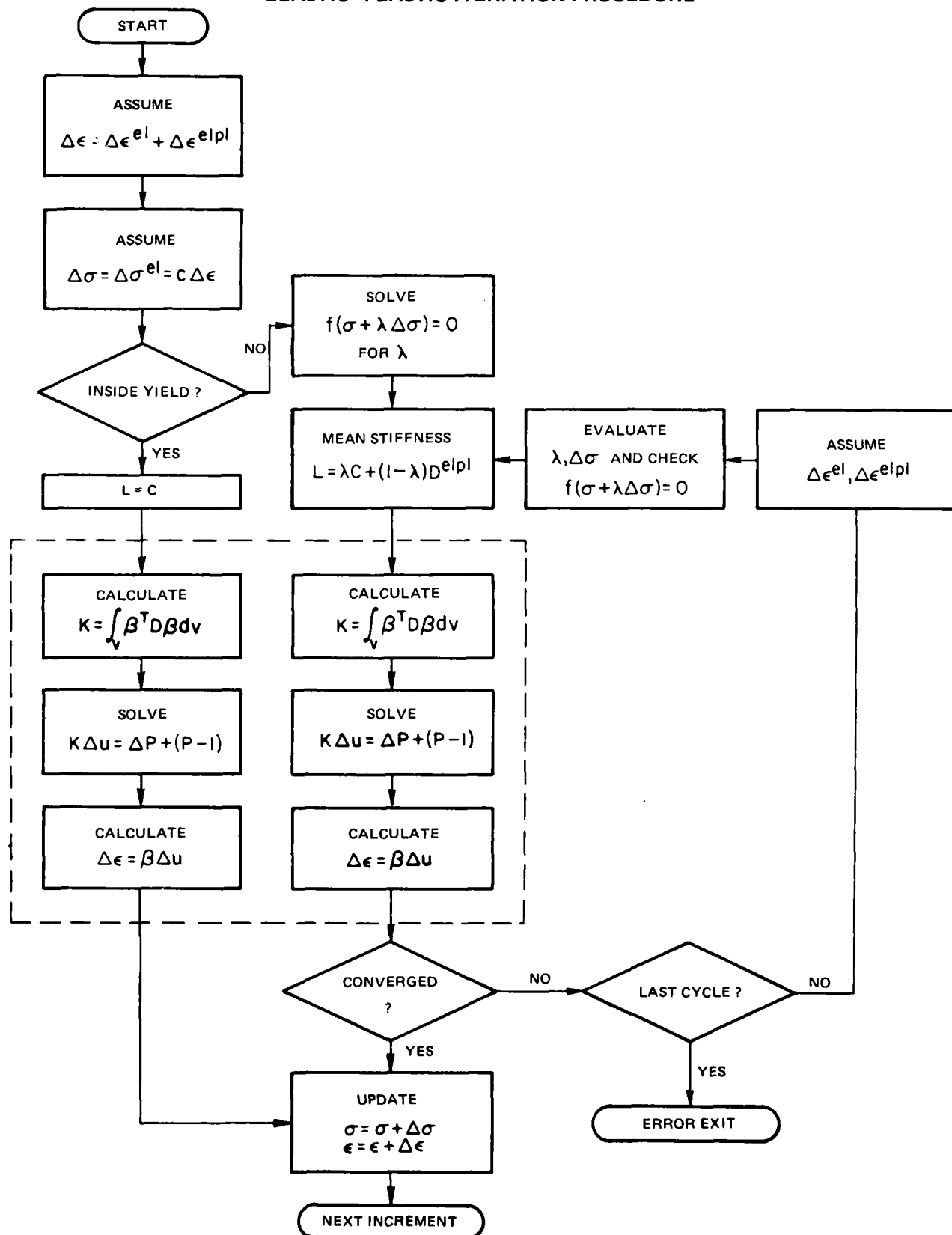
## COMPARISON OF POWDER COMPACTION FORMULAE WITH FINITE ELEMENT RESULTS



ELASTIC-PLASTIC STRAIN DECOMPOSITIONS  
FOR BILINEAR STRESS-STRAIN LAW

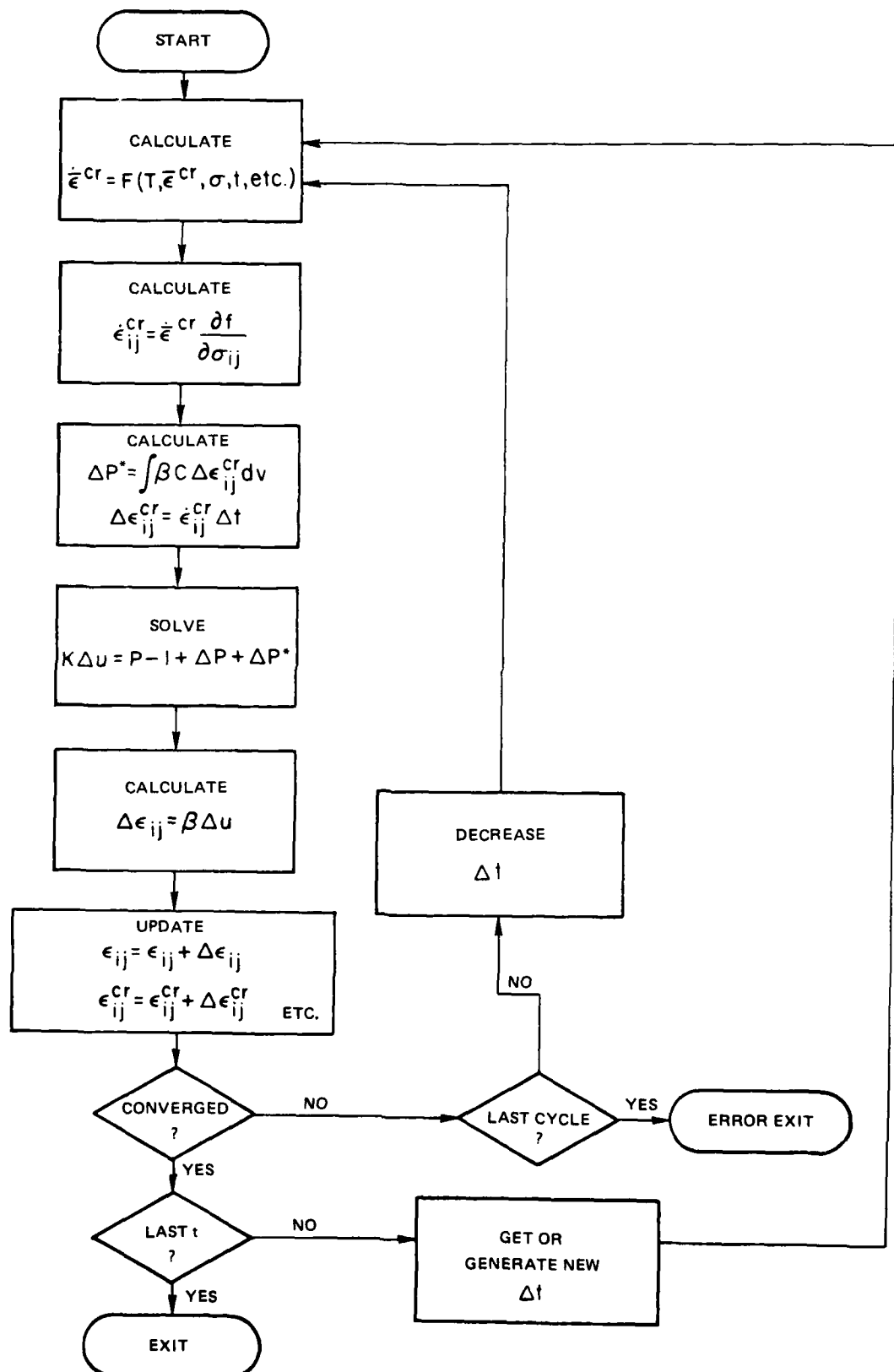


## ELASTIC-PLASTIC ITERATION PROCEDURE

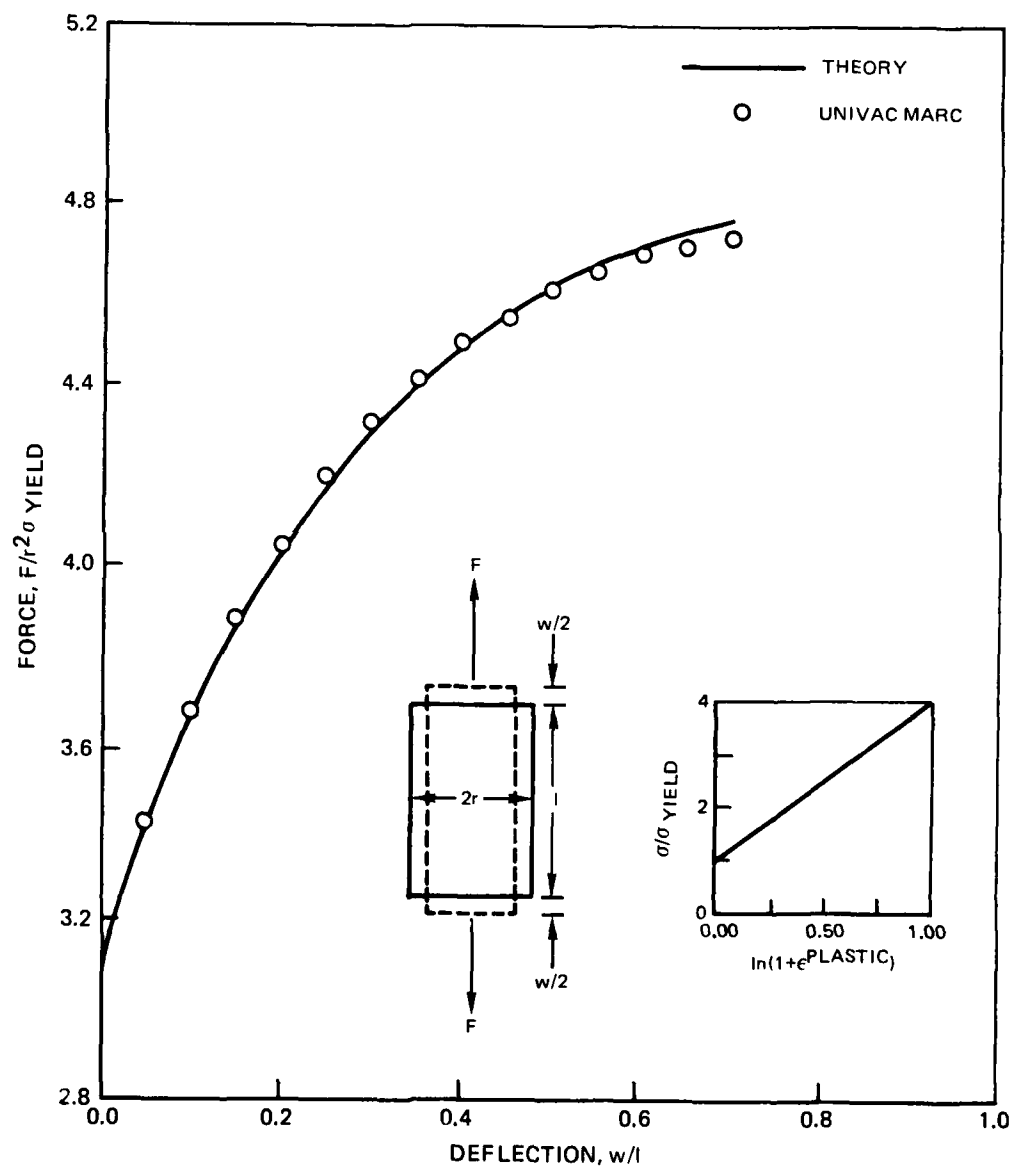


## CREEP ITERATION PROCEDURE

FIG. 13



## AXISYMMETRIC LARGE STRAIN MARC TEST CASE



AD-A088 208 UNITED TECHNOLOGIES RESEARCH CENTER EAST HARTFORD CONN F/6 13/8  
ANALYTICAL MODELING OF THE HOT ISOSTATIC PRESSING PROCESS. (U)  
JUL 80 B N CASSENTI, K J CHEVERTON F49620-78-C-0090

CLASSIFIED

R80-944374-13

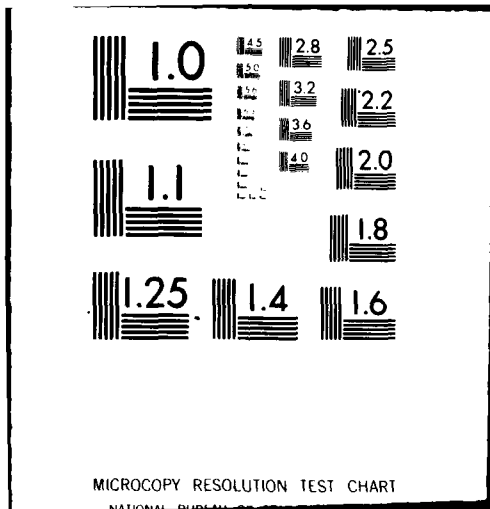
AFOSR-TR-80-0592

NL

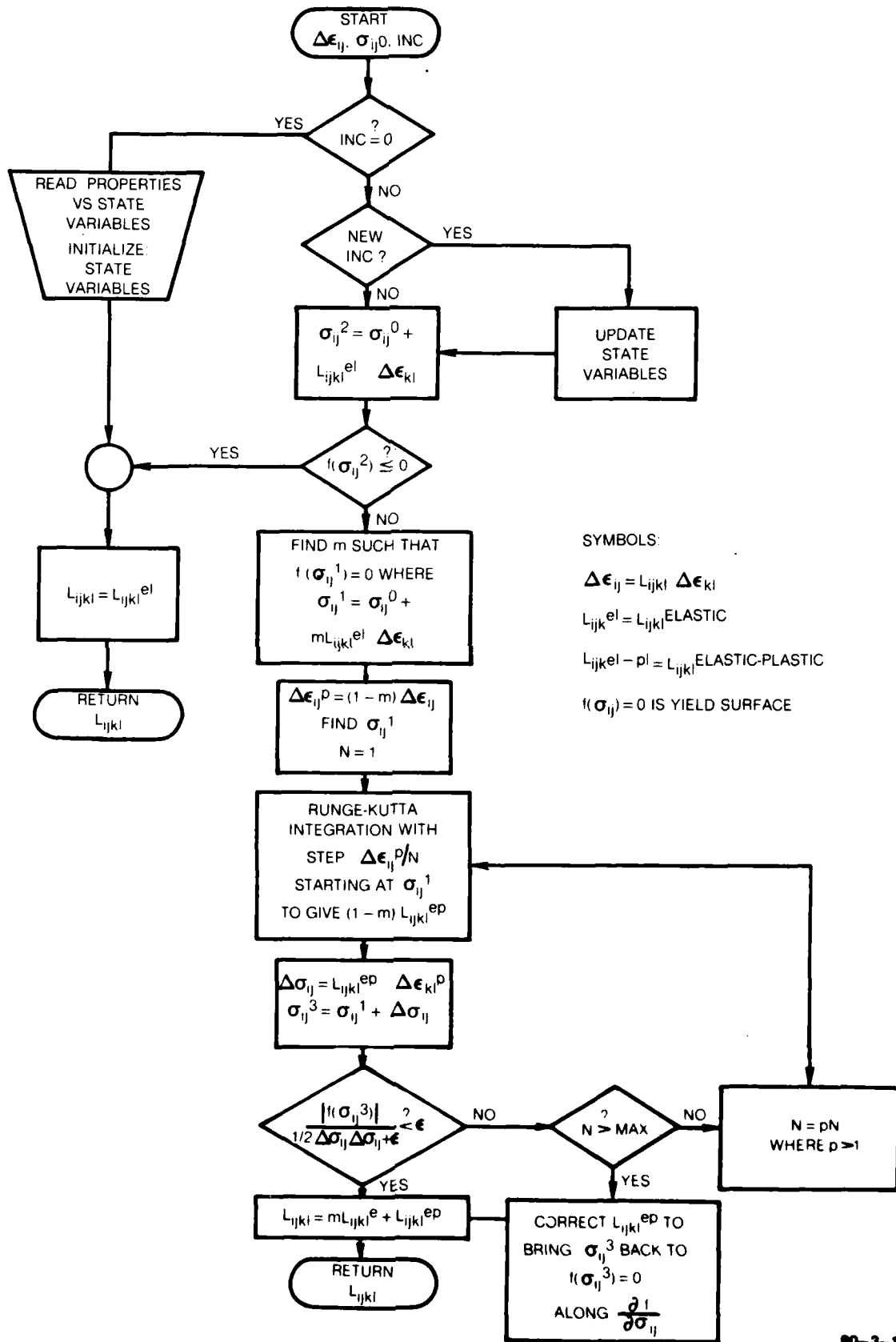
2.2

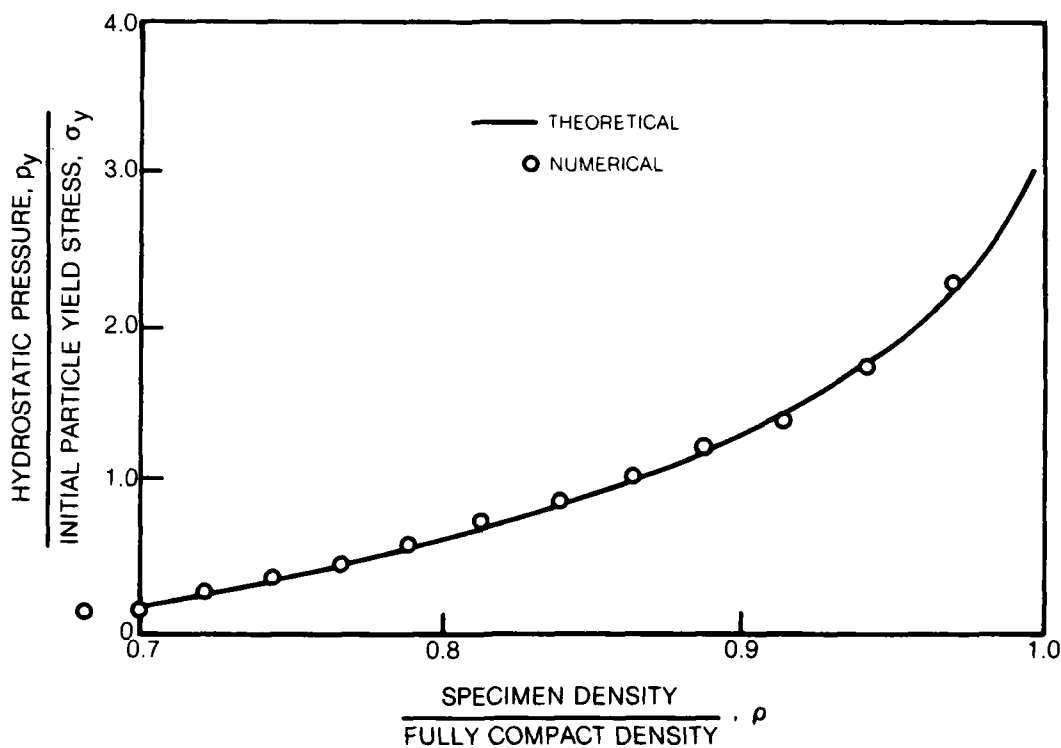
REF ID: A61004

END  
DATE FILMED  
9-80  
OTIC

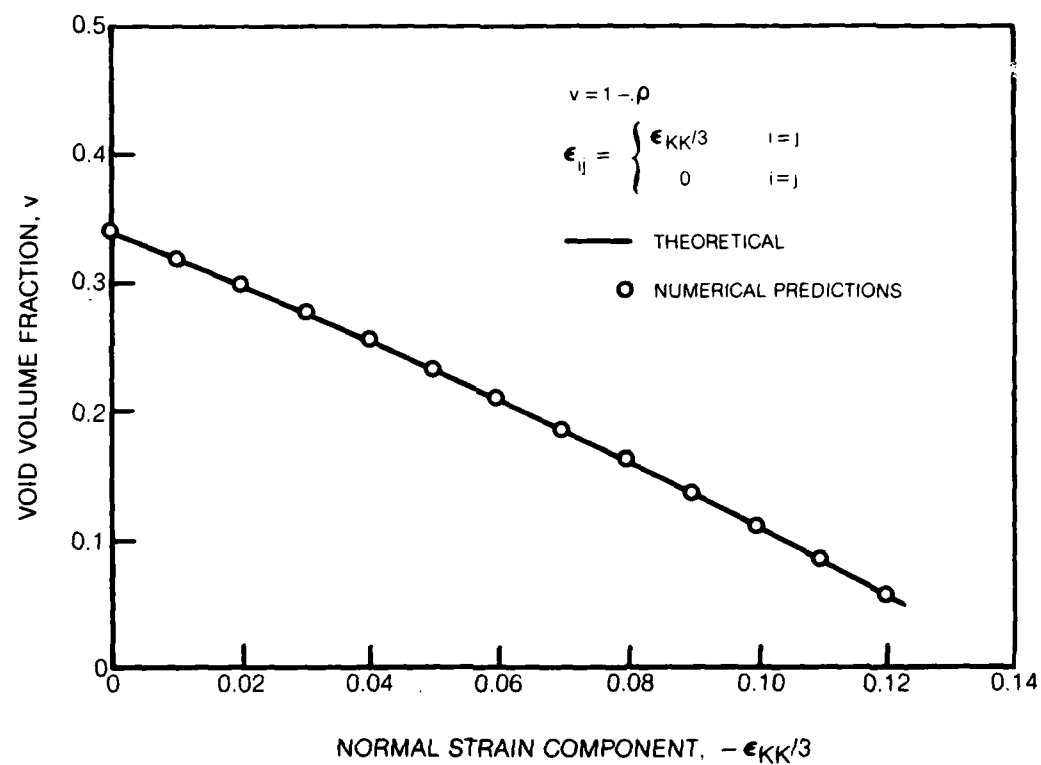


## FLOW CHART FOR CALCULATING MATERIAL STIFFNESS MATRIX

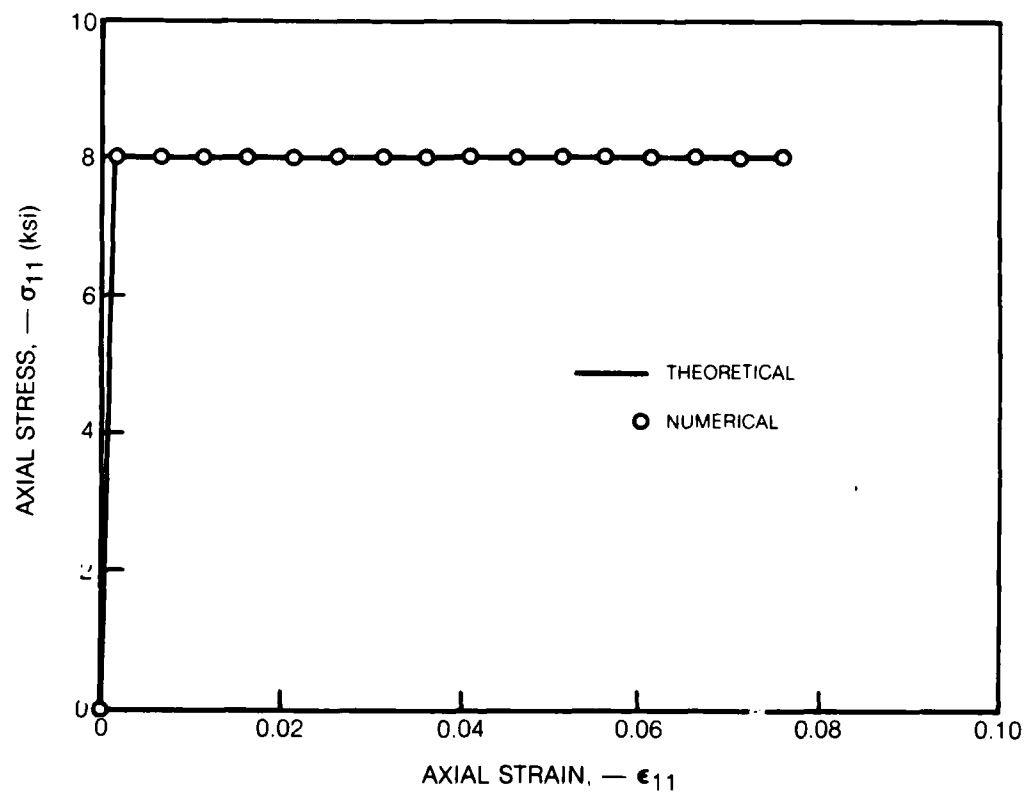


**HYDROSTATIC PRESSURE NUMERICAL TEST CASE RESULTS**

## VOID VOLUME FRACTION FOR HYDROSTATIC PRESSURE NUMERICAL TEST CASE RESULTS



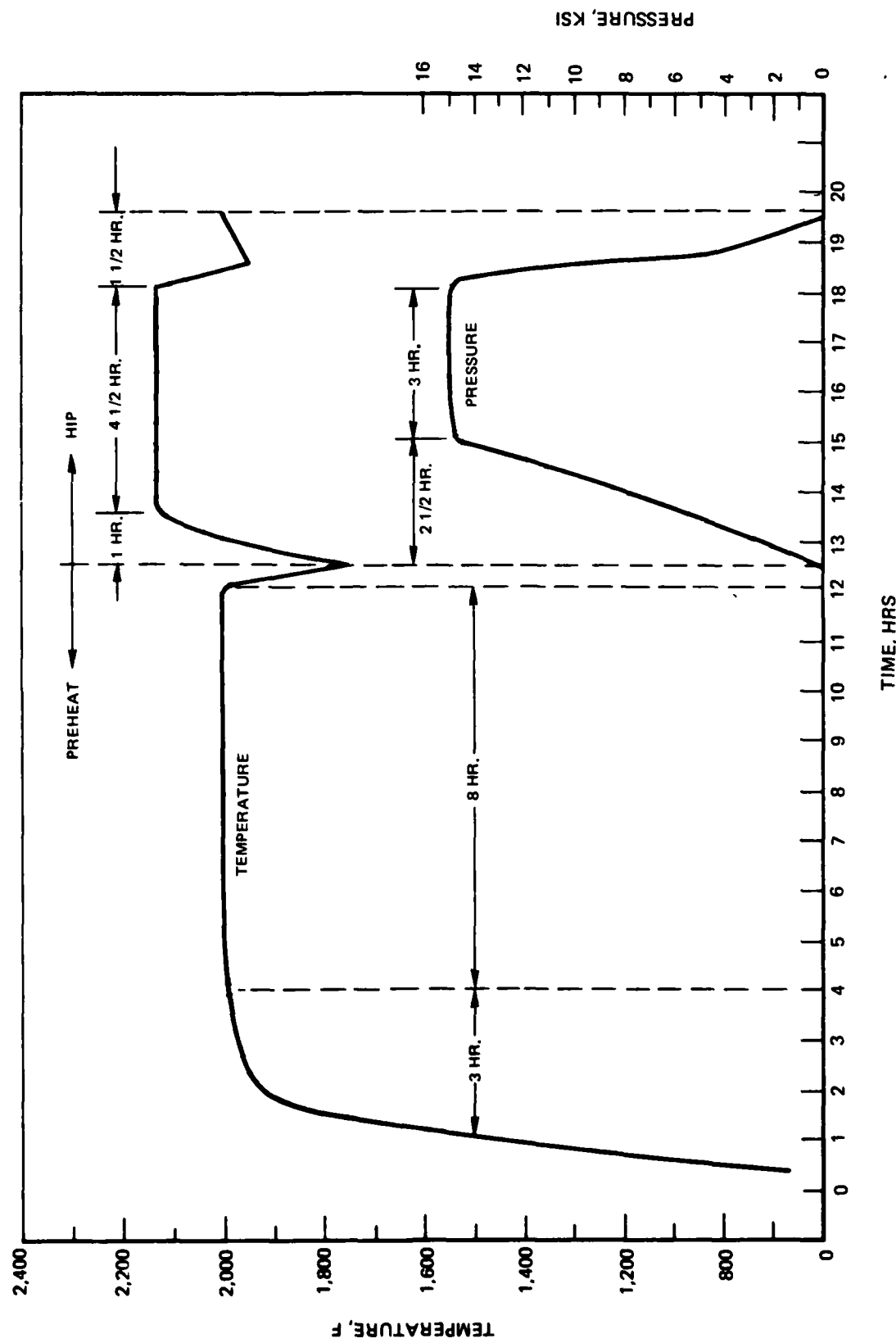
## UNIAXIAL COMPRESSION NUMERICAL TEST CASE RESULTS



R80-944374-13

FIG. 19

TYPICAL HIP PROCESS  
TEMPERATURE-PRESSURE-TIME PROFILE

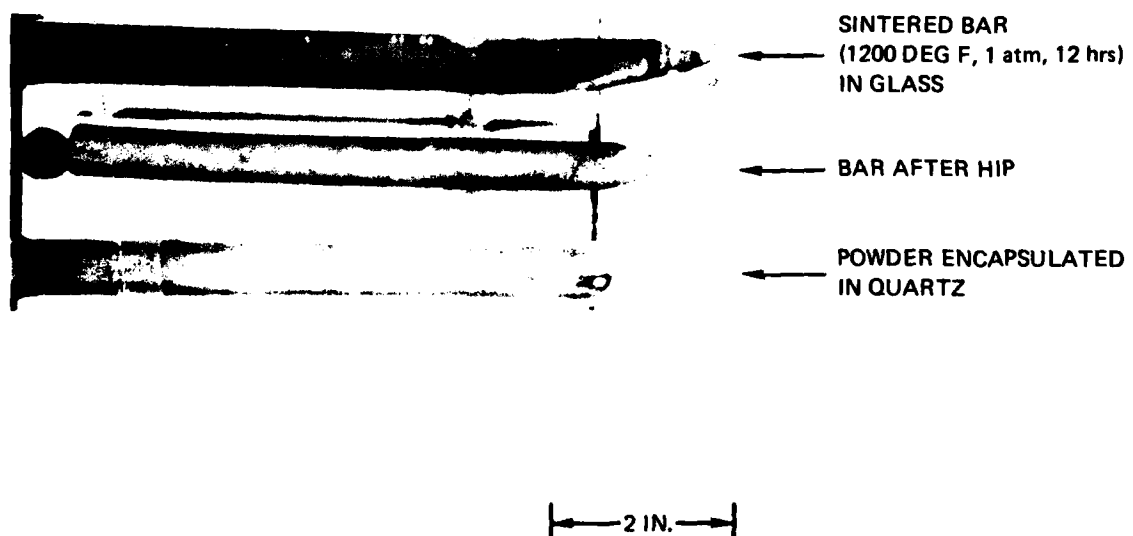


78-01-212-1

R80-944374-13

FIG. 20

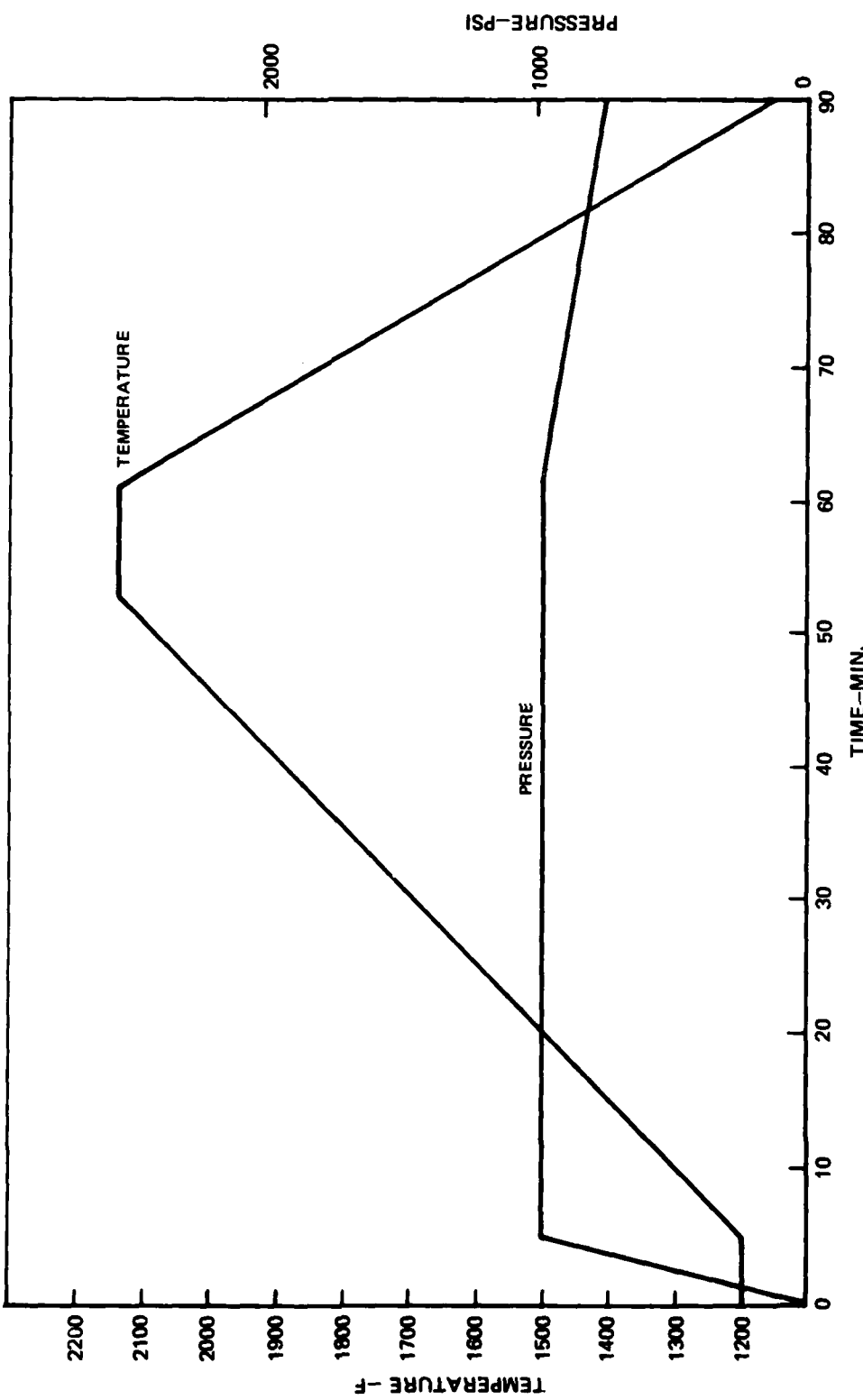
PARTIAL HIP SPECIMENS AT VARIOUS PROCESSING STAGES



R80-944374-13

FIG. 21

HIP UNIT PRESSURE AND TEMPERATURE CYCLE FOR SPECIMEN 3

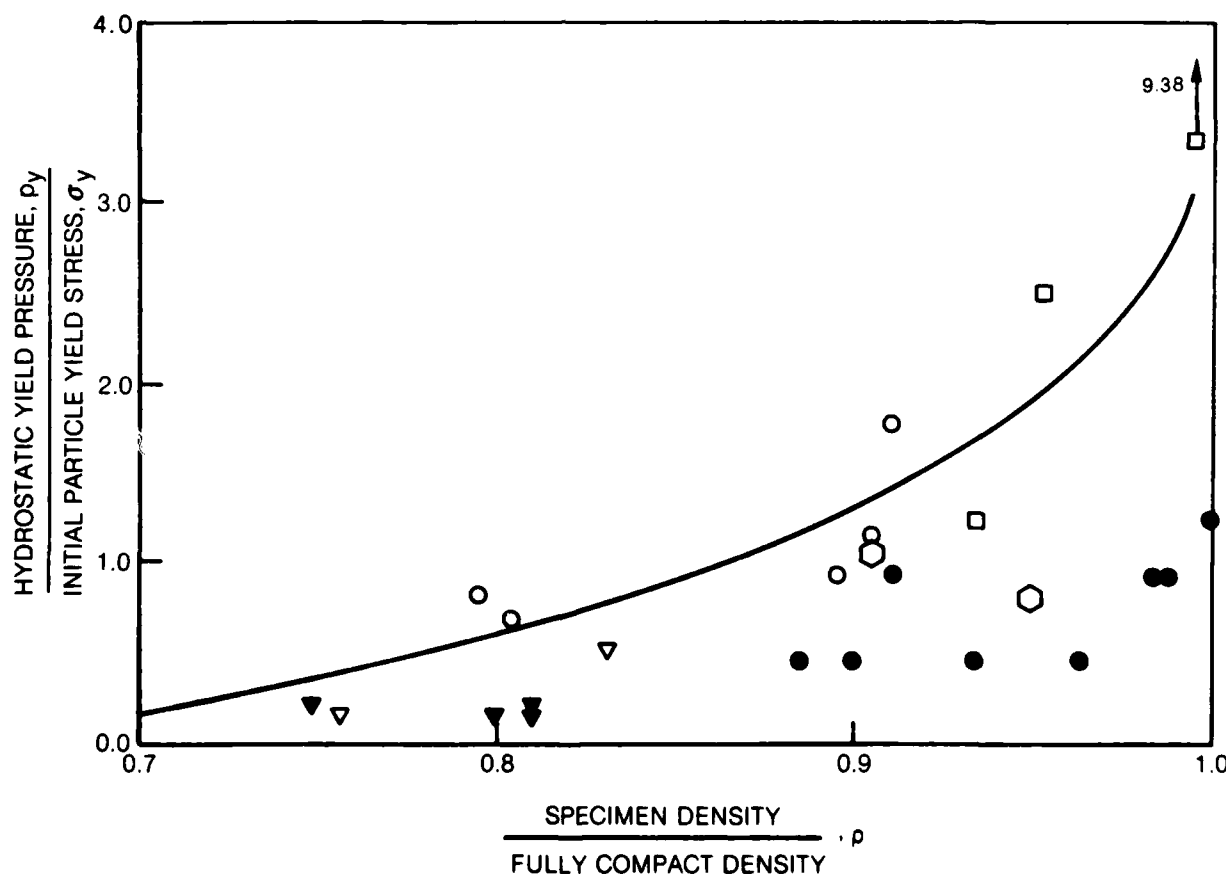


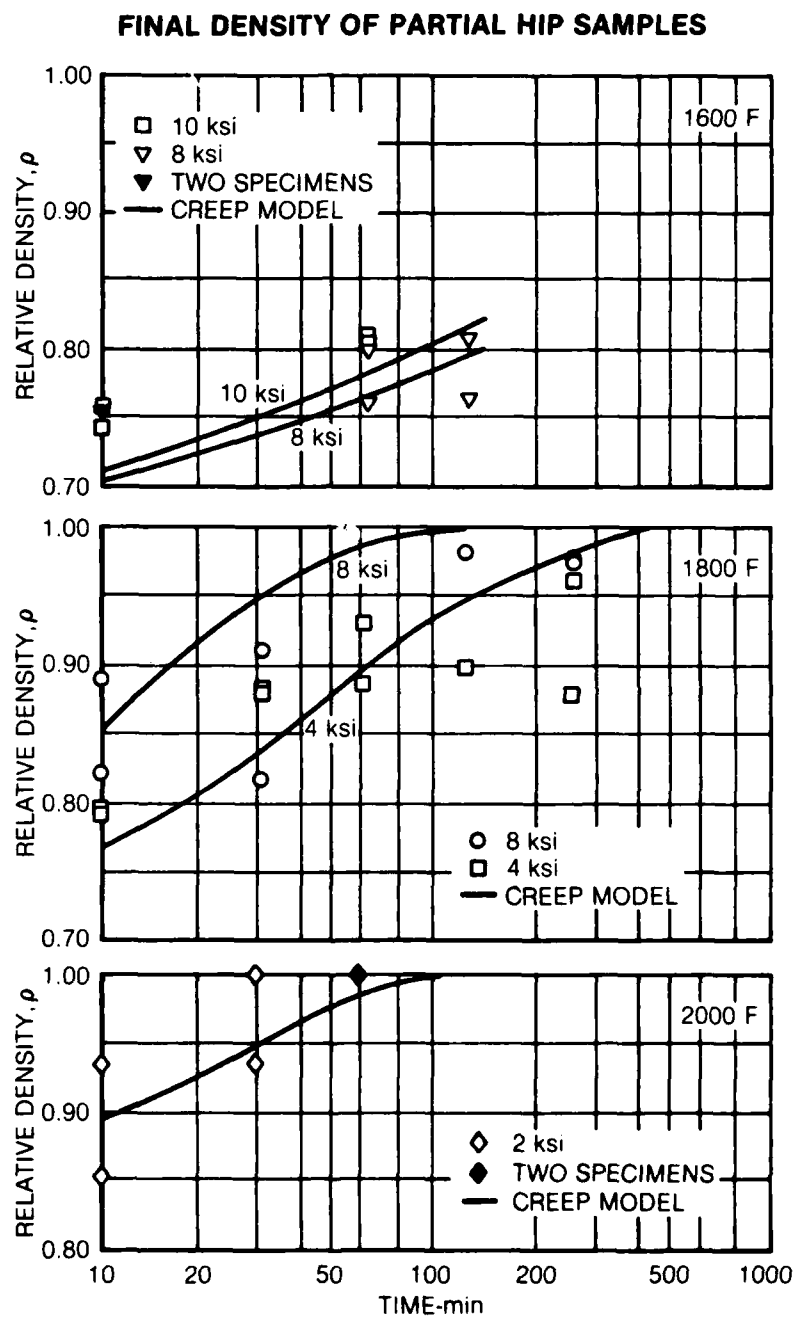
79-08-78-3

### HYDROSTATIC YIELD PRESSURE TEST RESULTS

MERL 76

SYMBOL	TEMP. F	TIME, m
▽	1600	10
○	1800	10
○	1900	10
□	2000	10
▼	1600	>10
●	1800	>10
○	1900	>10
■	2000	>10
THEORY		

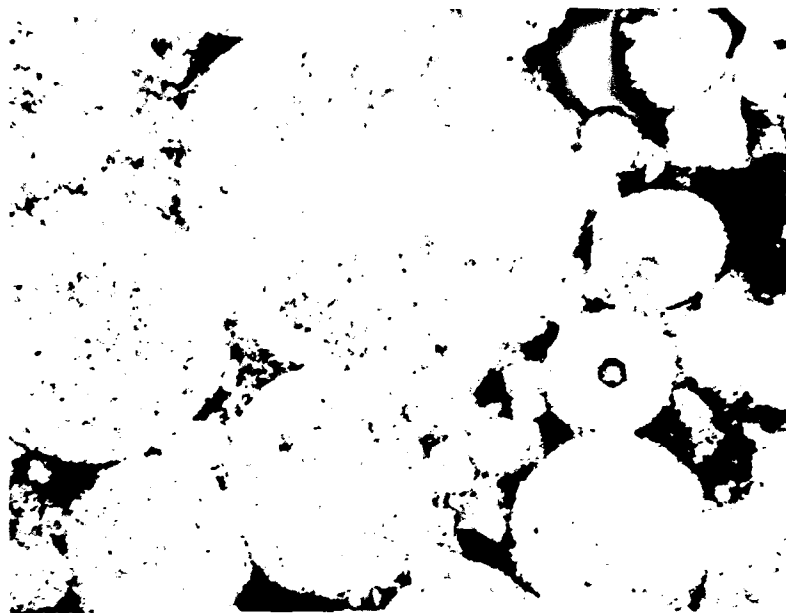




R80-944374-13

FIG. 24

**MICROGRAMS OF PARTIALLY COMPACTED MERL76 POWDER**



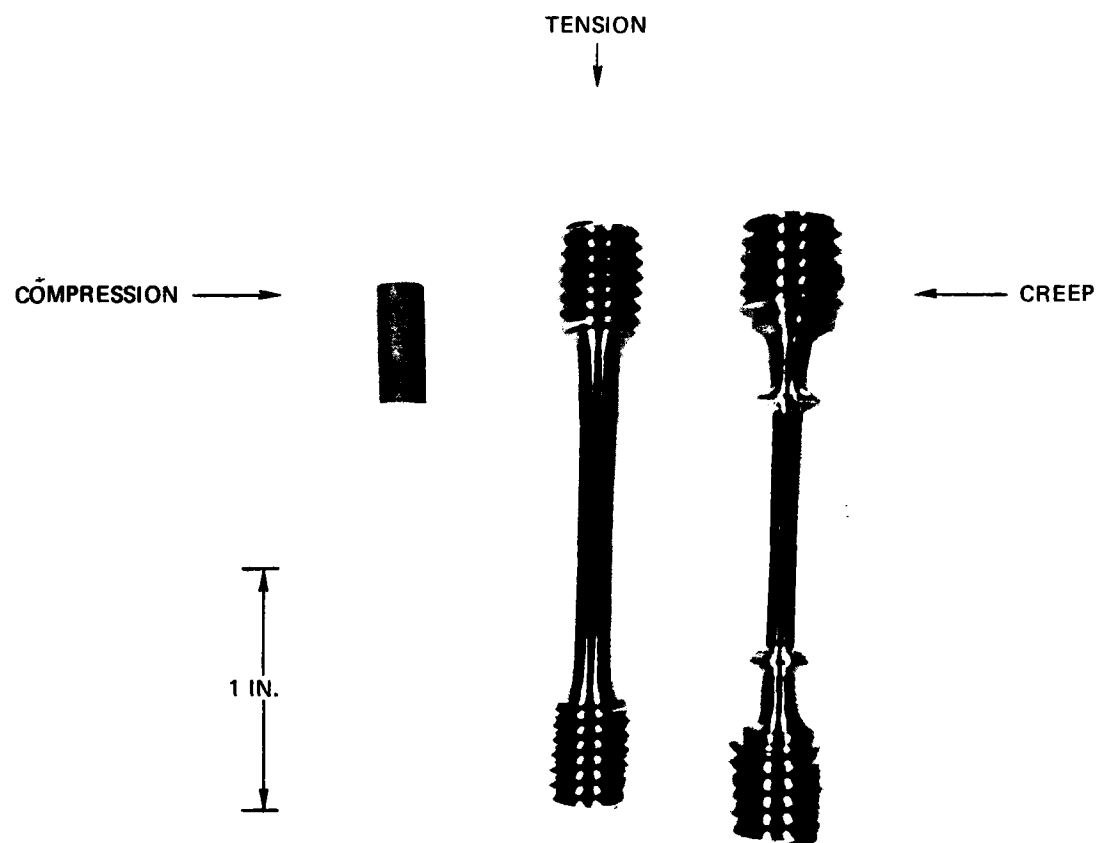
b) 10 MIN. AT 1800 DEG. F AND 8 ksi; RELATIVE DENSITY 0.89, 500X



R80-944374-13

FIG. 25

**TEST SPECIMENS**



R80-944374-13

SAMPLE COMPRESSION TEST DATA  
SPECIMEN NO. 1006, 1800 F (REF. 3)

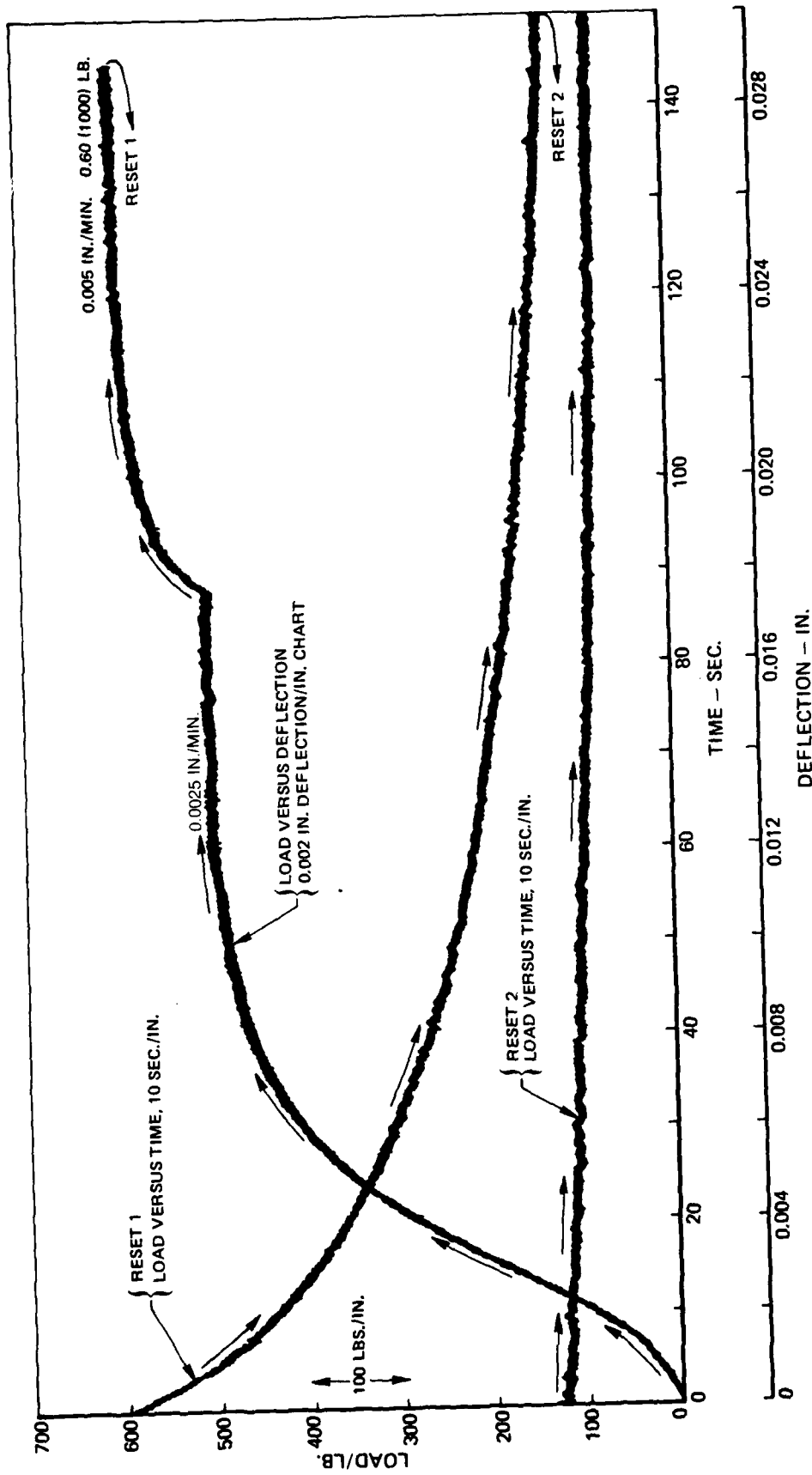
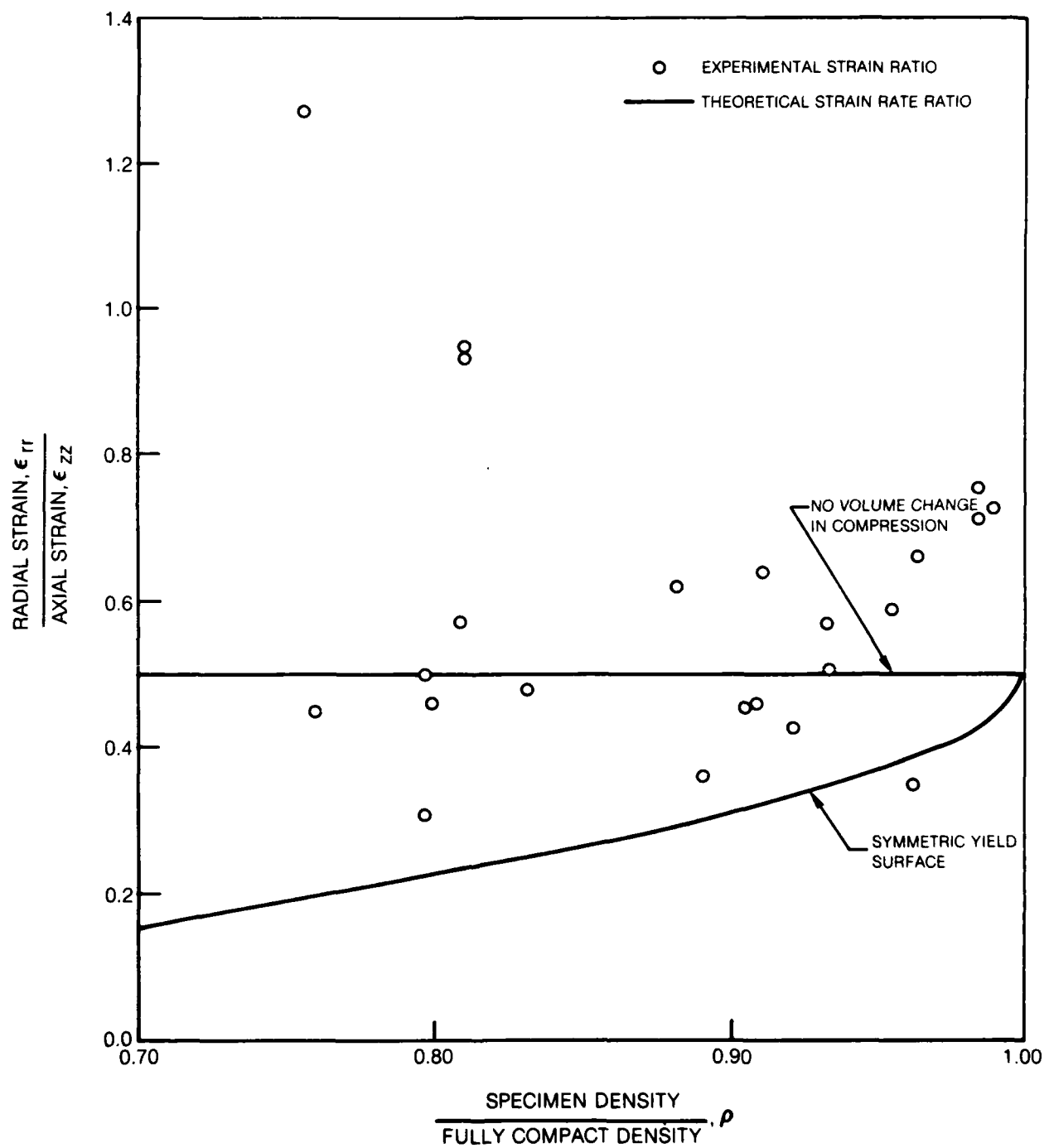
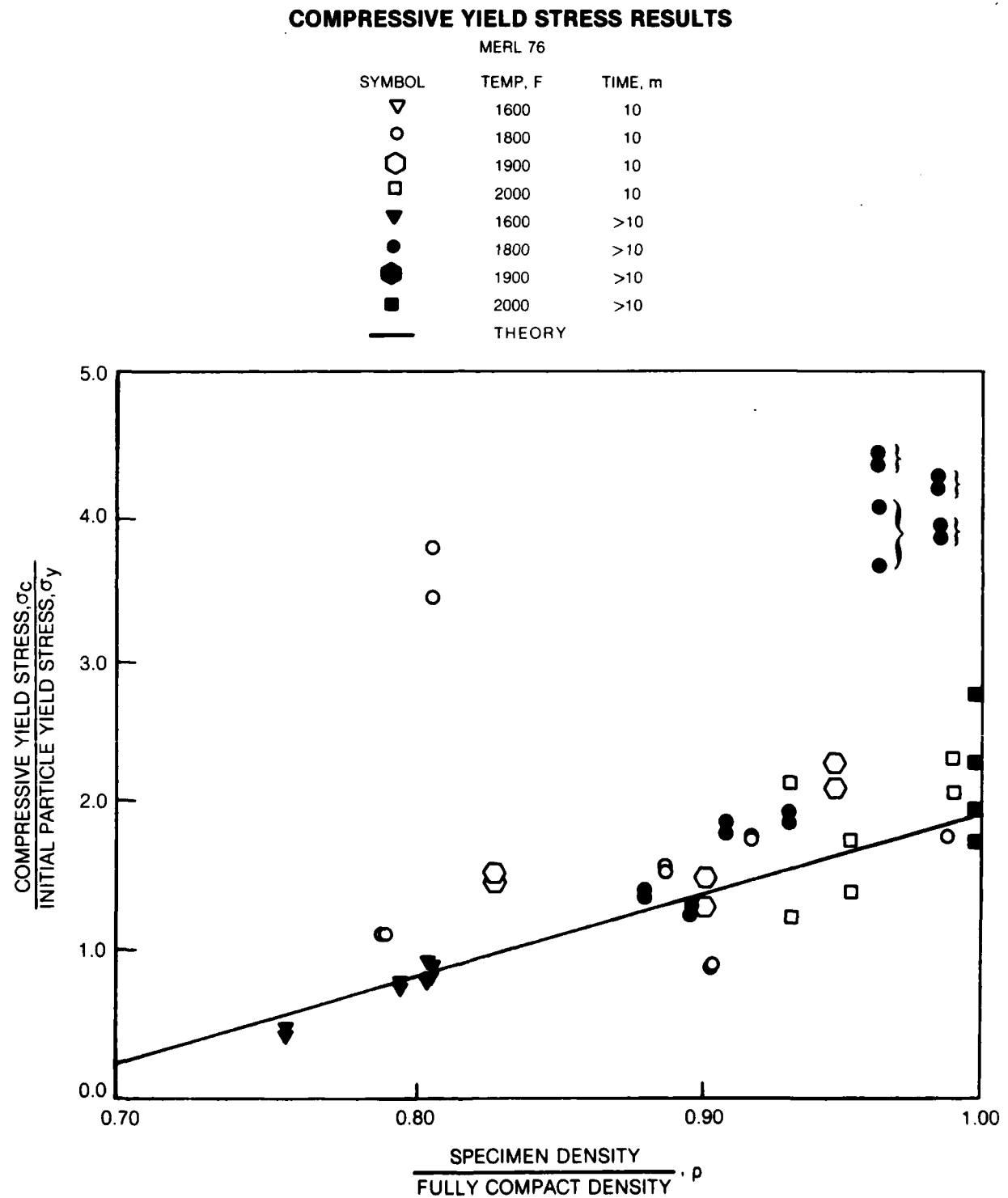


FIG. 26

## THEORETICAL STRAIN RATE RATIO CORRELATION

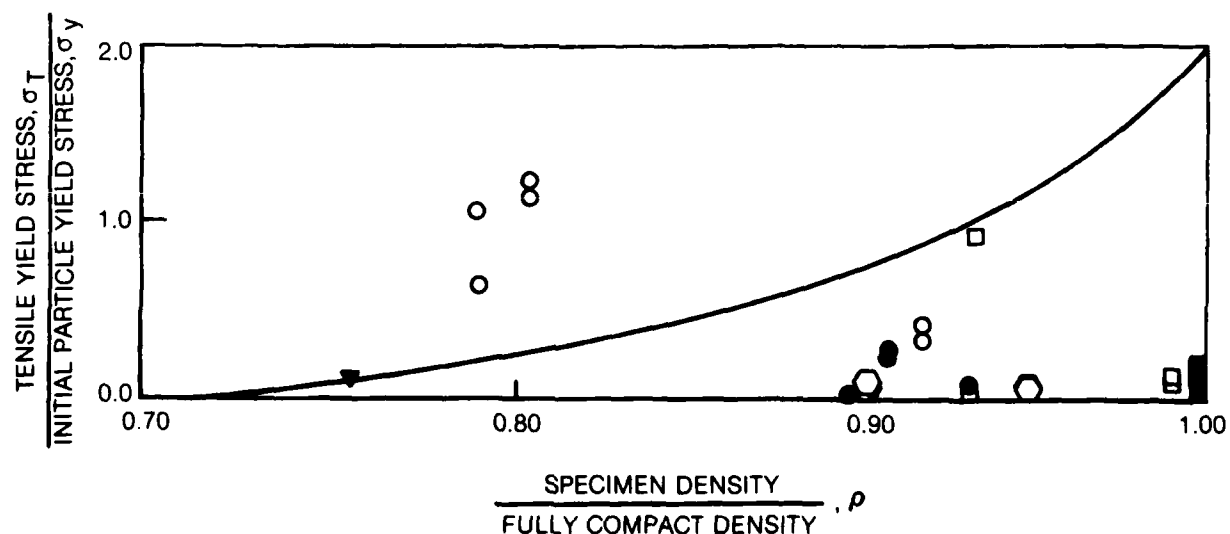




### TENSILE YIELD STRESS RESULTS

MERL 76

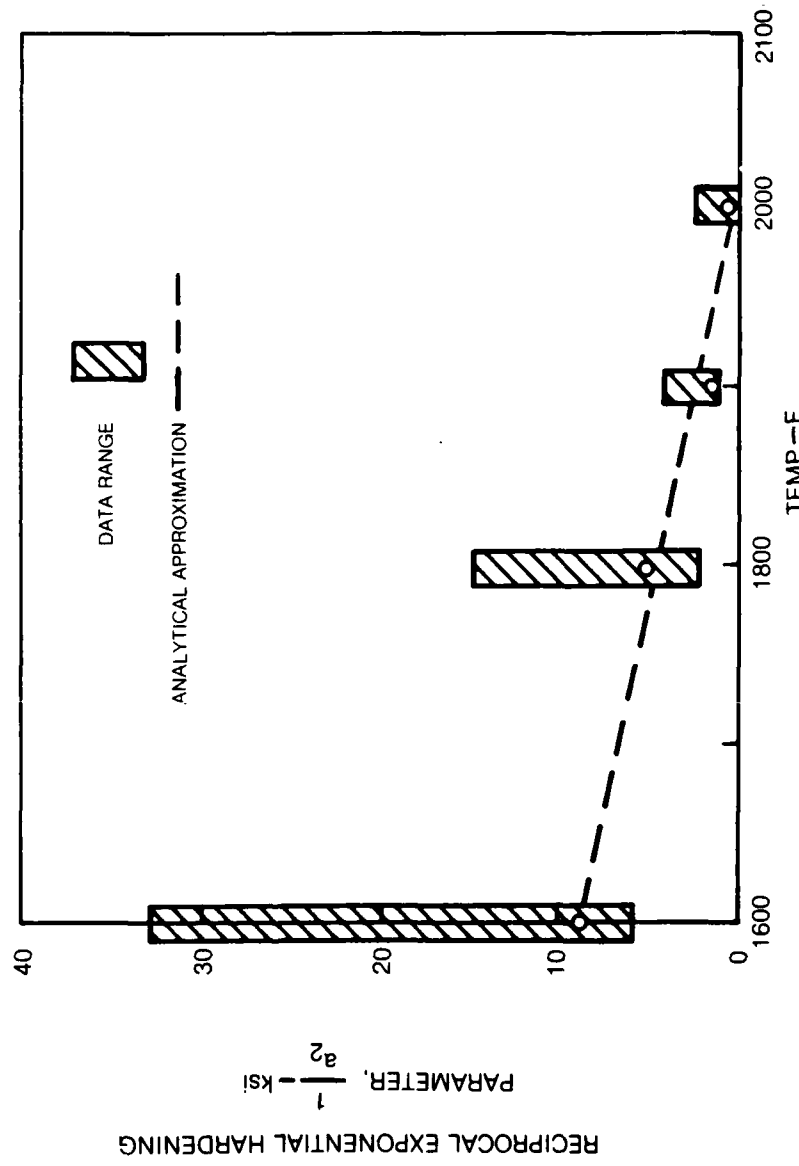
SYMBOL	TEMP. F	TIME, m
▽	1600	10
○	1800	10
○	1900	10
□	2000	10
▼	1600	>10
●	1800	>10
○	1900	>10
■	2000	>10
THEORY		



R80-944374-13

FIG. 30

EXPONENTIAL HARDENING PARAMETER FOR MERL 76

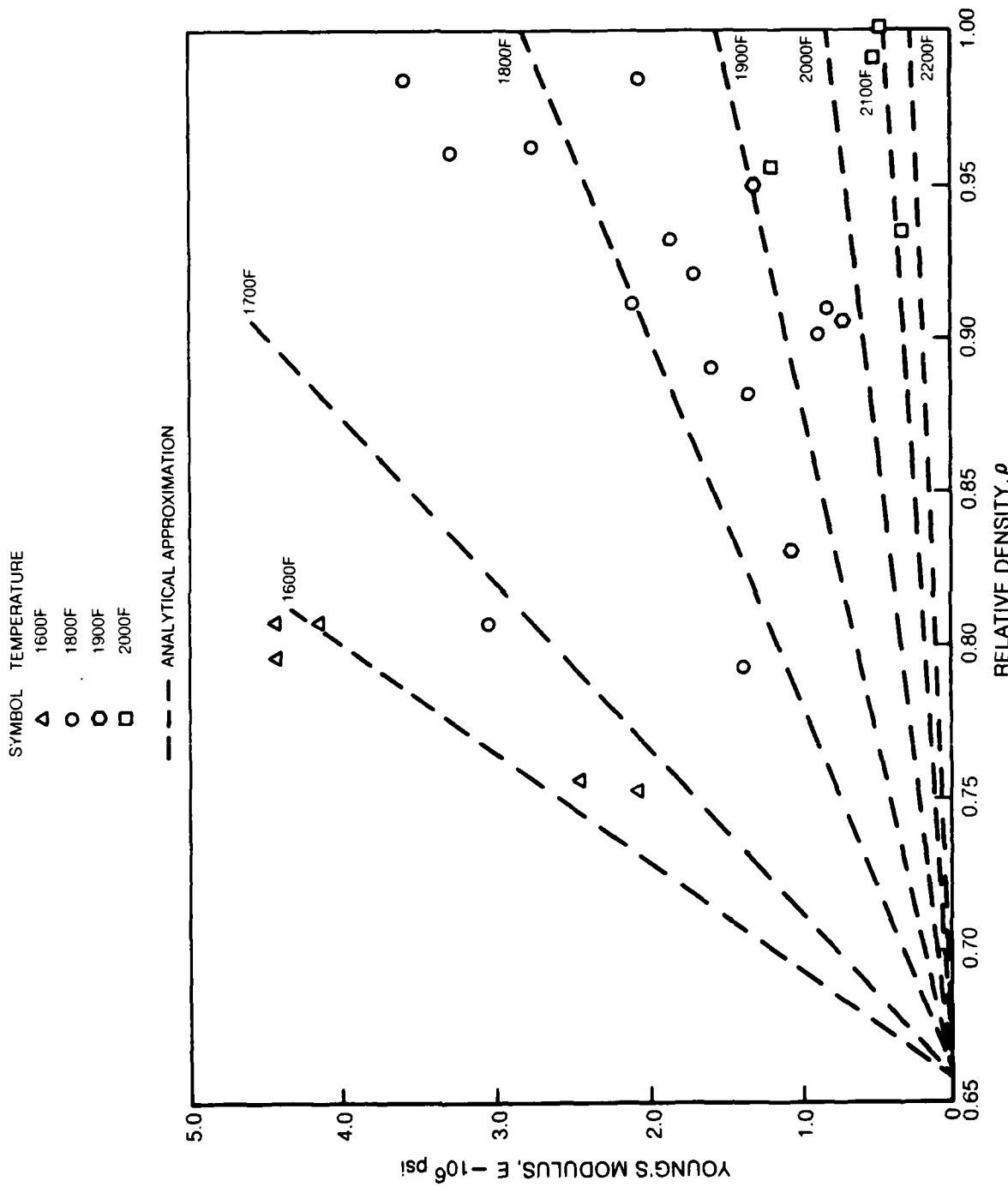


80-06-18-12

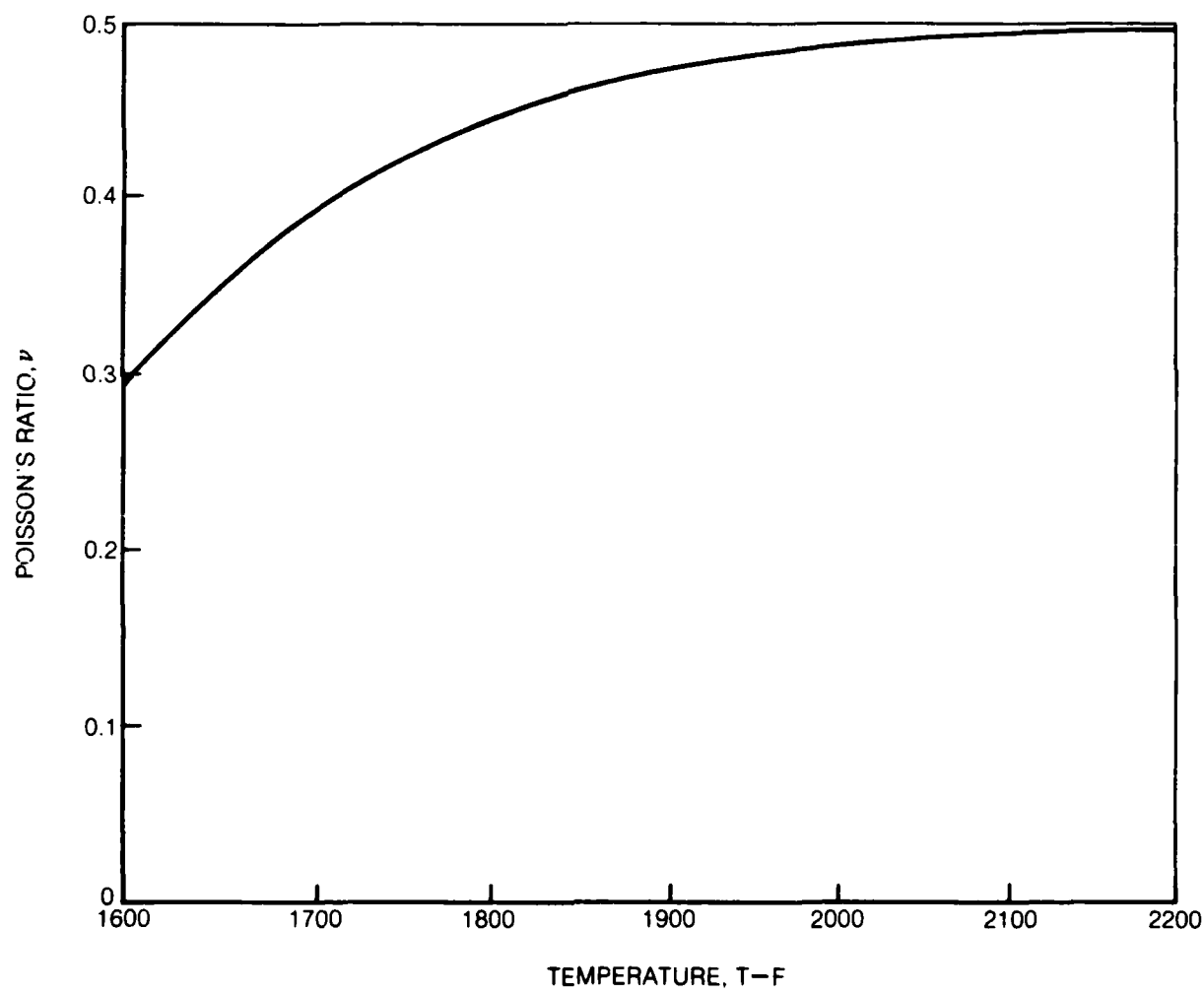
R80-944374-13

FIG. 31

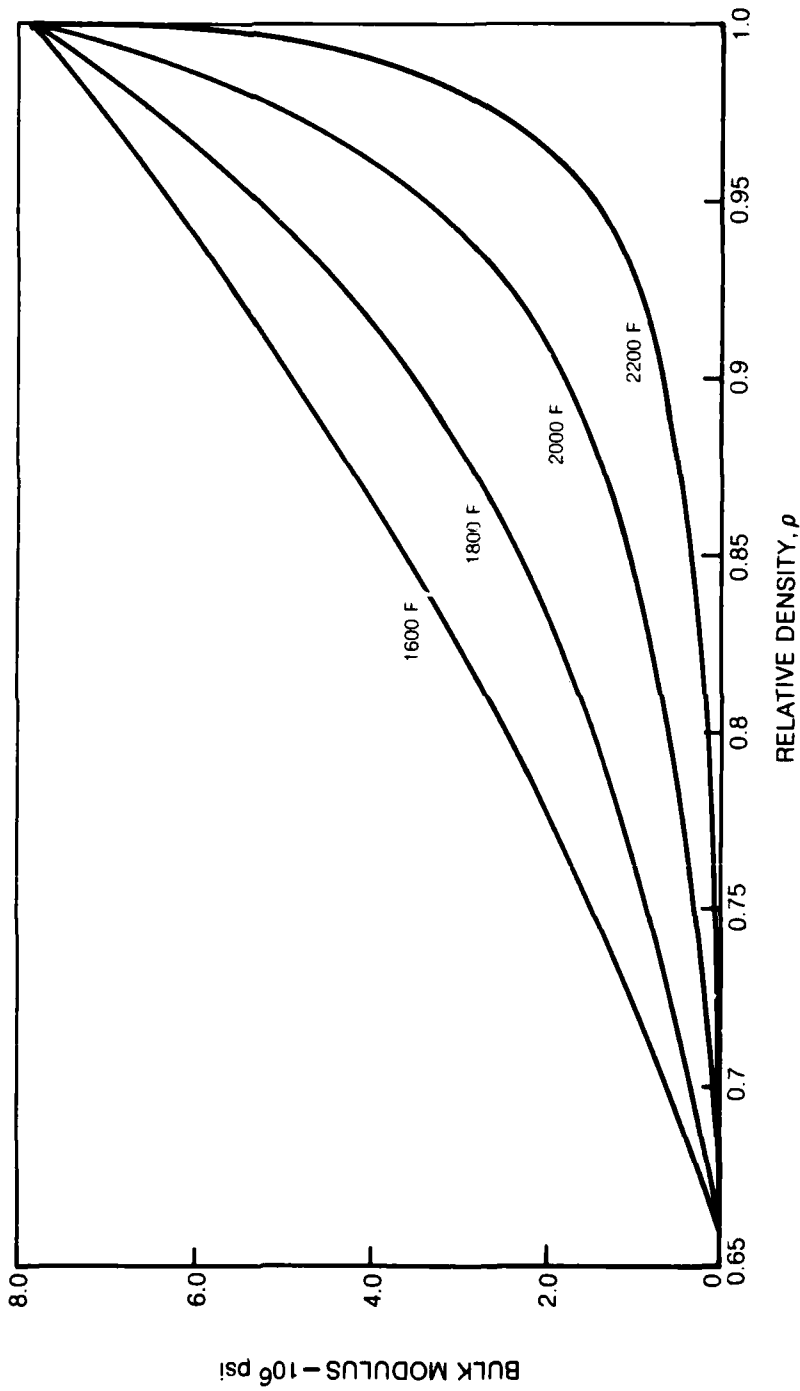
YOUNG'S MODULUS FOR PARTIALLY DENSE MERL 76



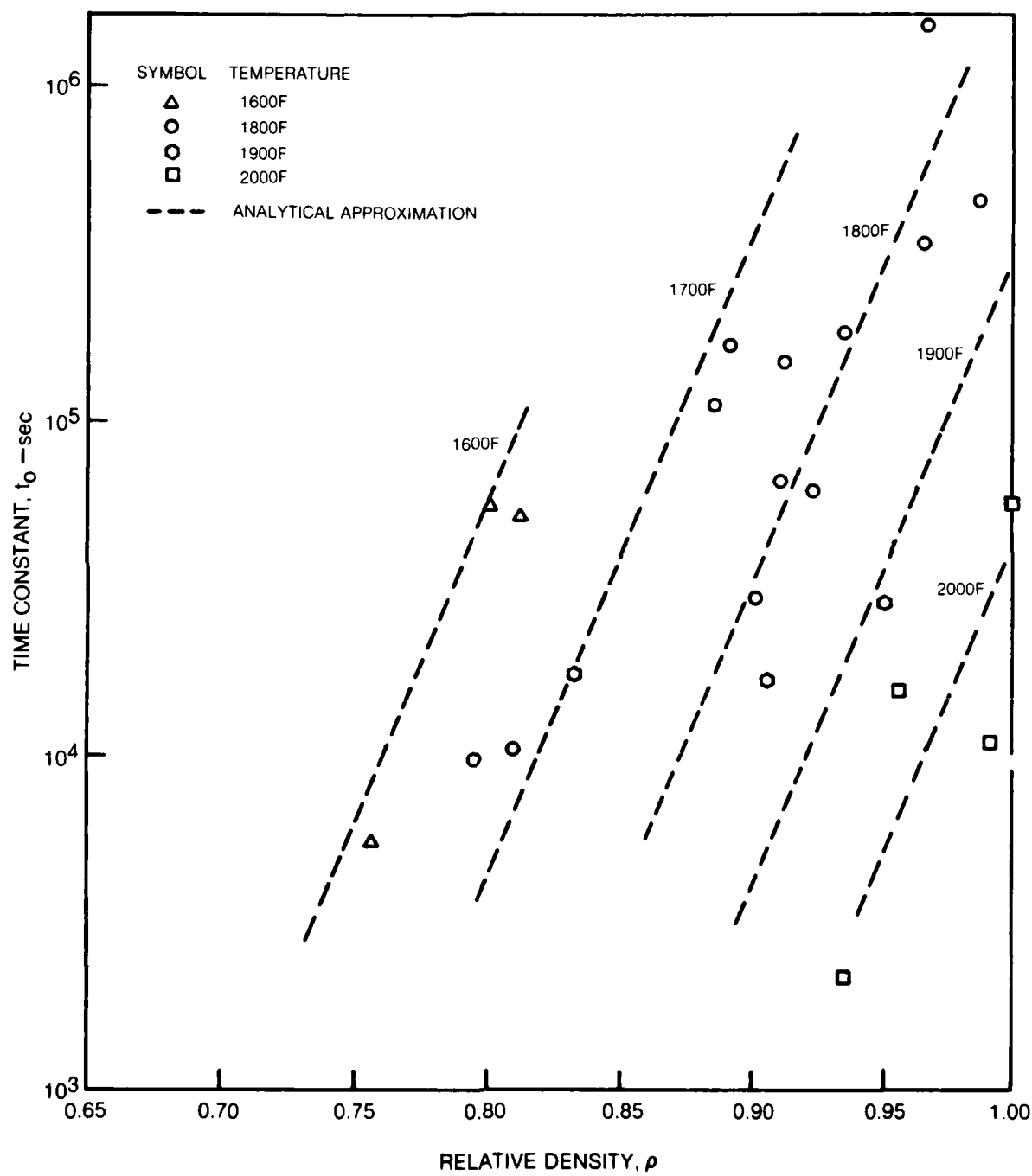
80-06-18-7

**ASSUMED POISSON'S RATIO FOR MERL 76**

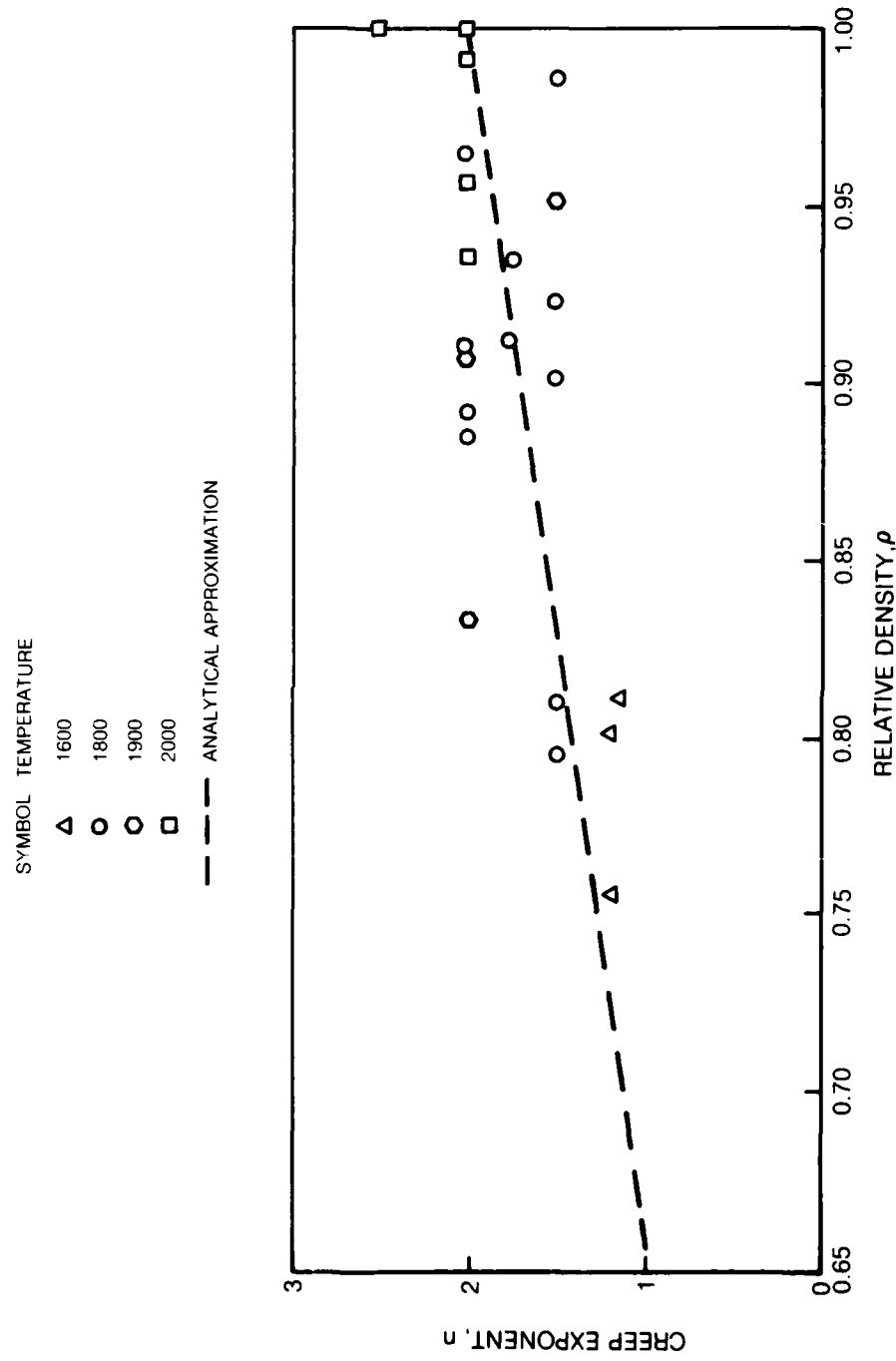
## ASSUMED BULK MODULUS FOR PARTIALLY DENSE MERL 76



## DEVIATORIC CREEP TIME CONSTANT FOR PARTIALLY DENSE MERL 76



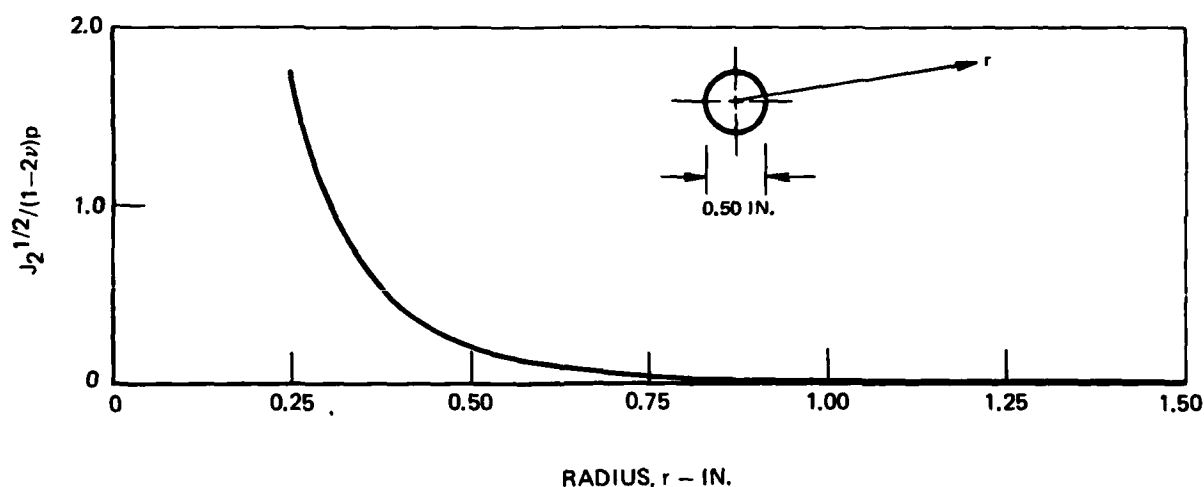
## DEVIATORIC CREEP EXPONENT FOR PARTIALLY DENSE MERL 76



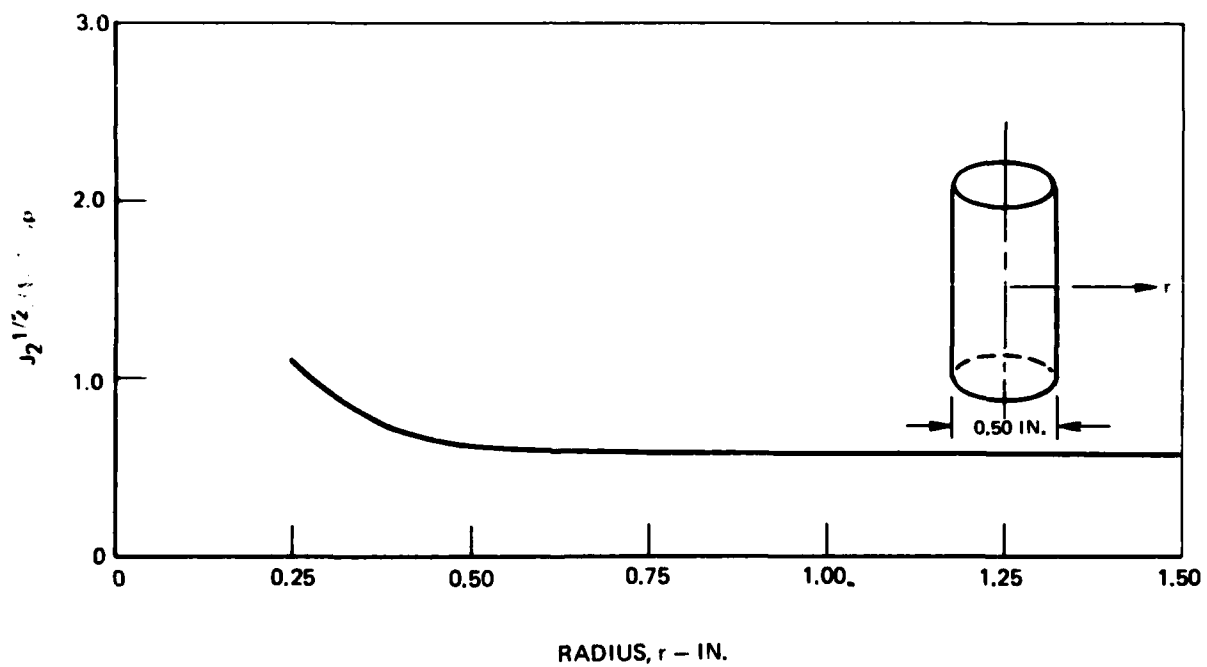
R80-944374-13

FIG. 36

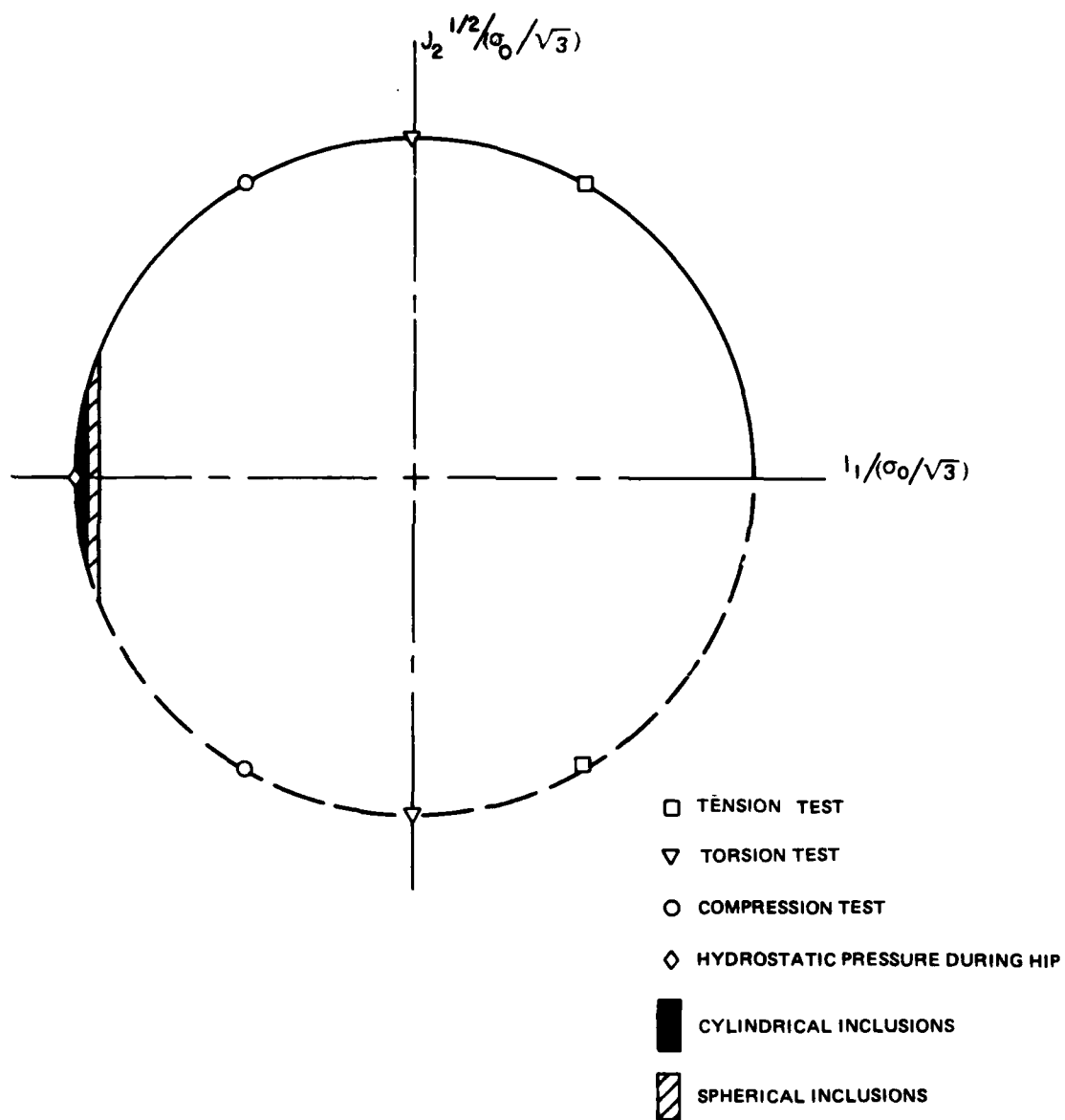
SECOND DEVIATORIC STRESS INVARIANT FOR RIGID SPHERICAL  
INCLUSION EMBEDDED IN AN INFINITE ELASTIC SOLID



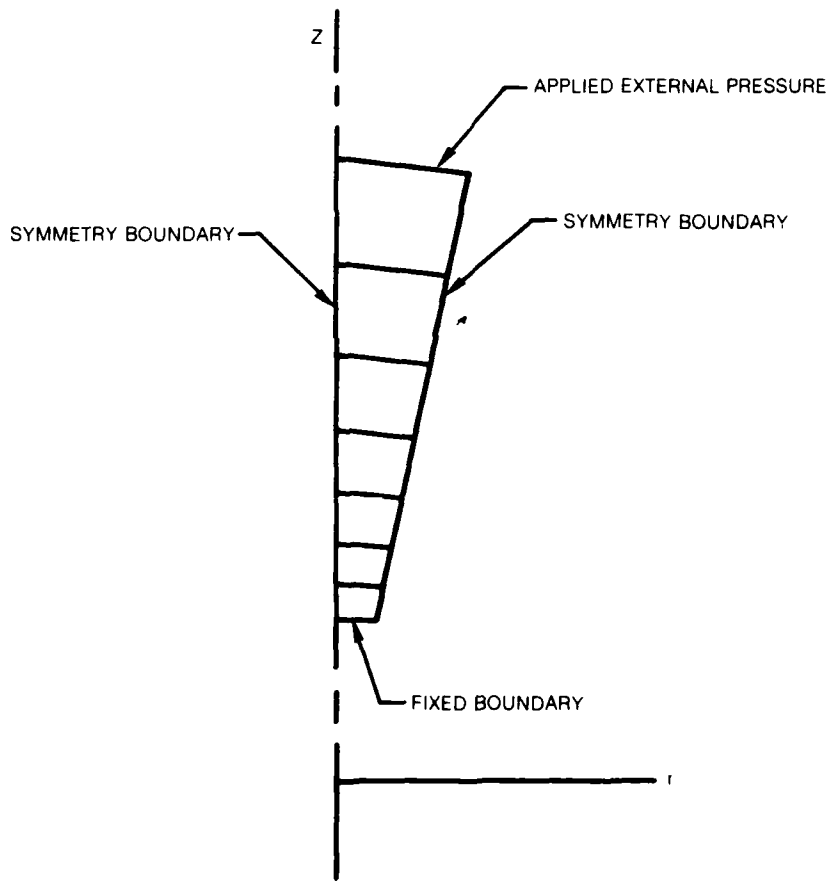
**SECOND DEVIATORIC STRESS INVARIANT FOR RIGID CYLINDRICAL INCLUSION  
EMBEDDED IN AN INFINITE ELASTIC SOLID**

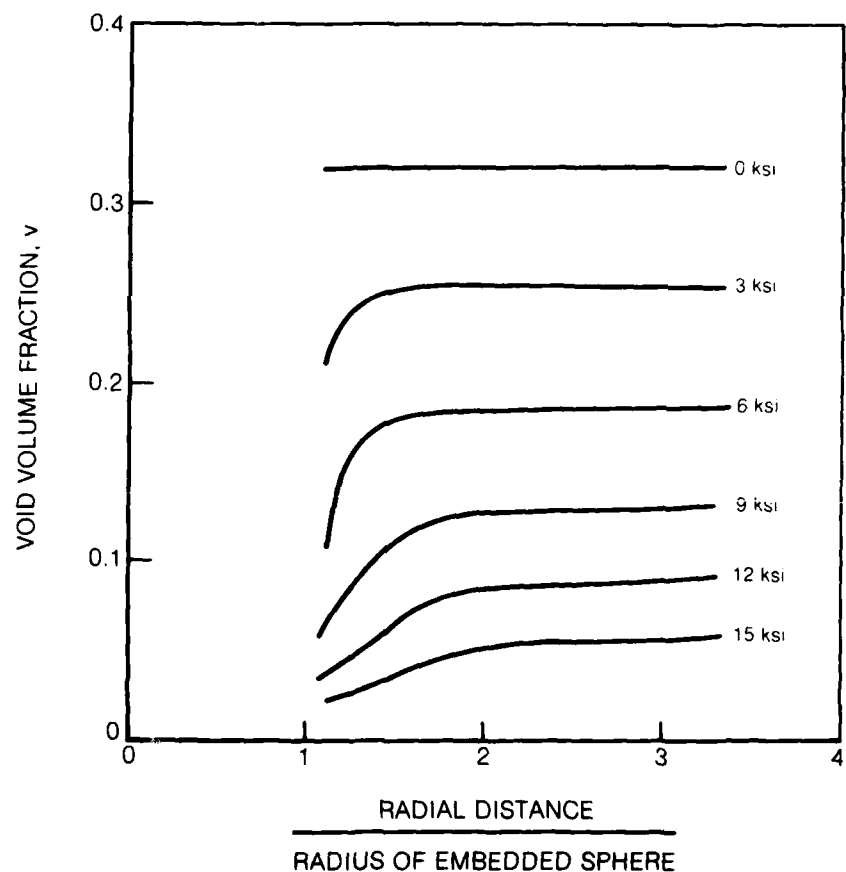


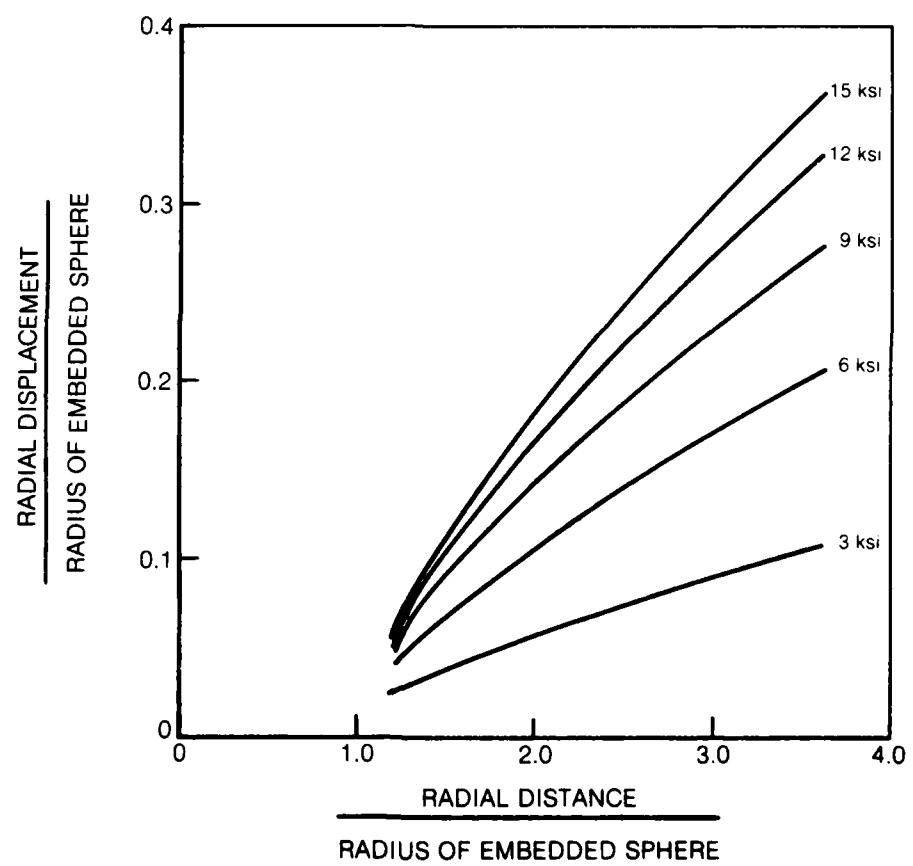
## LOCATION OF VALIDATION EXPERIMENTS ON YIELD SURFACE



**VERIFICATION EXPERIMENT FINITE ELEMENT MODEL**



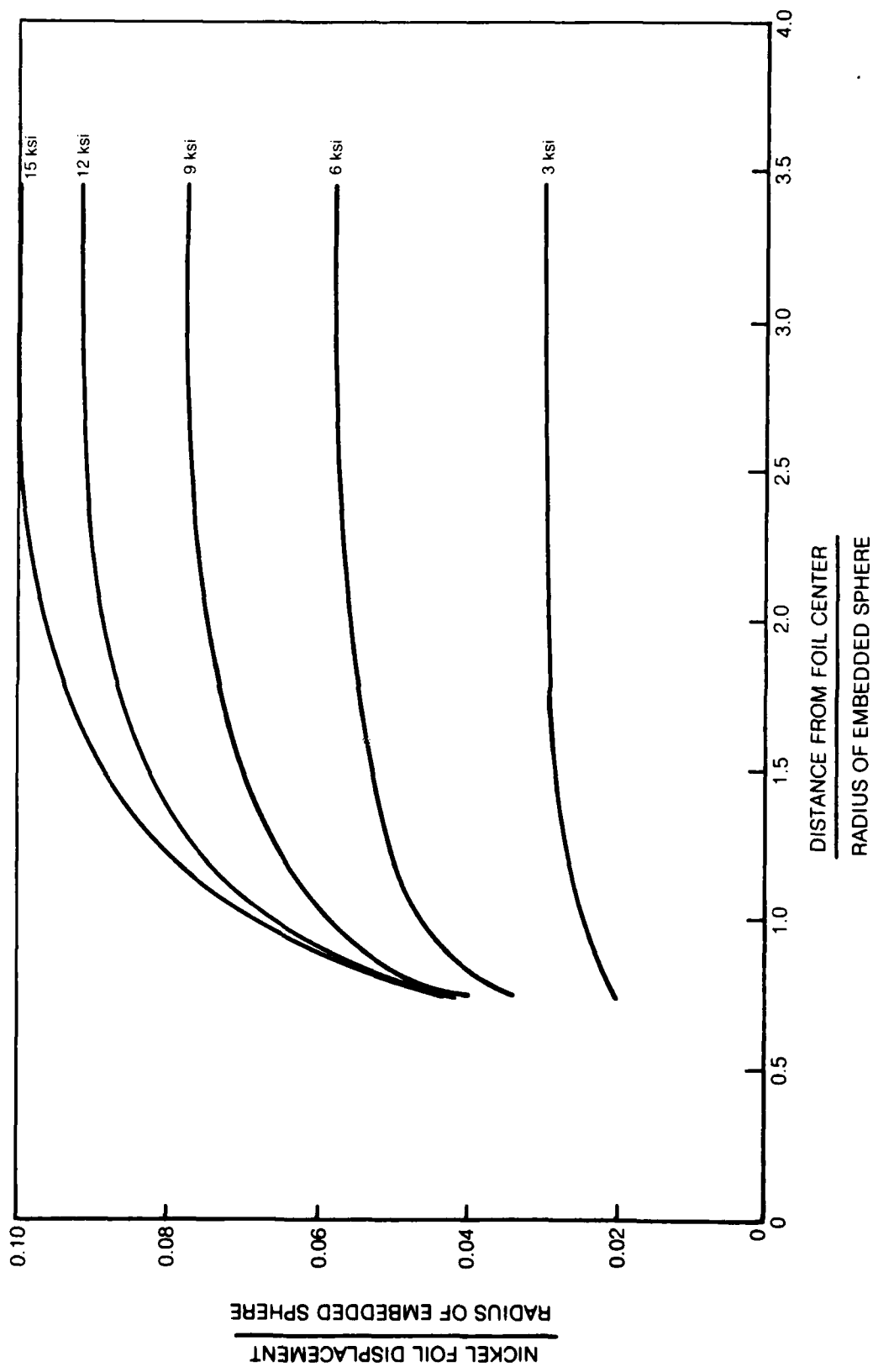
**PREDICTED VOID VOLUME FRACTION FOR VERIFICATION EXPERIMENT**

**PREDICTED RADIAL DISPLACEMENTS FOR VERIFICATION EXPERIMENT**

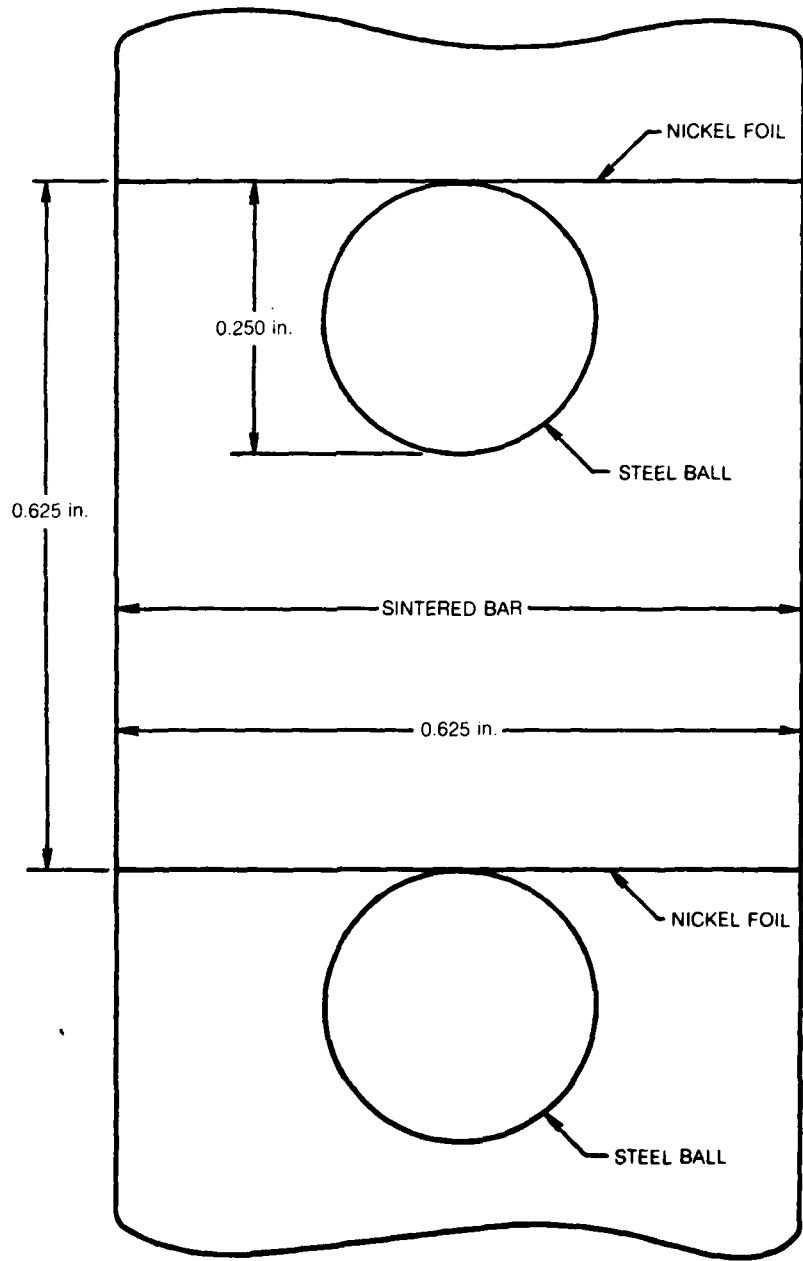
R80-944374-13

FIG. 42

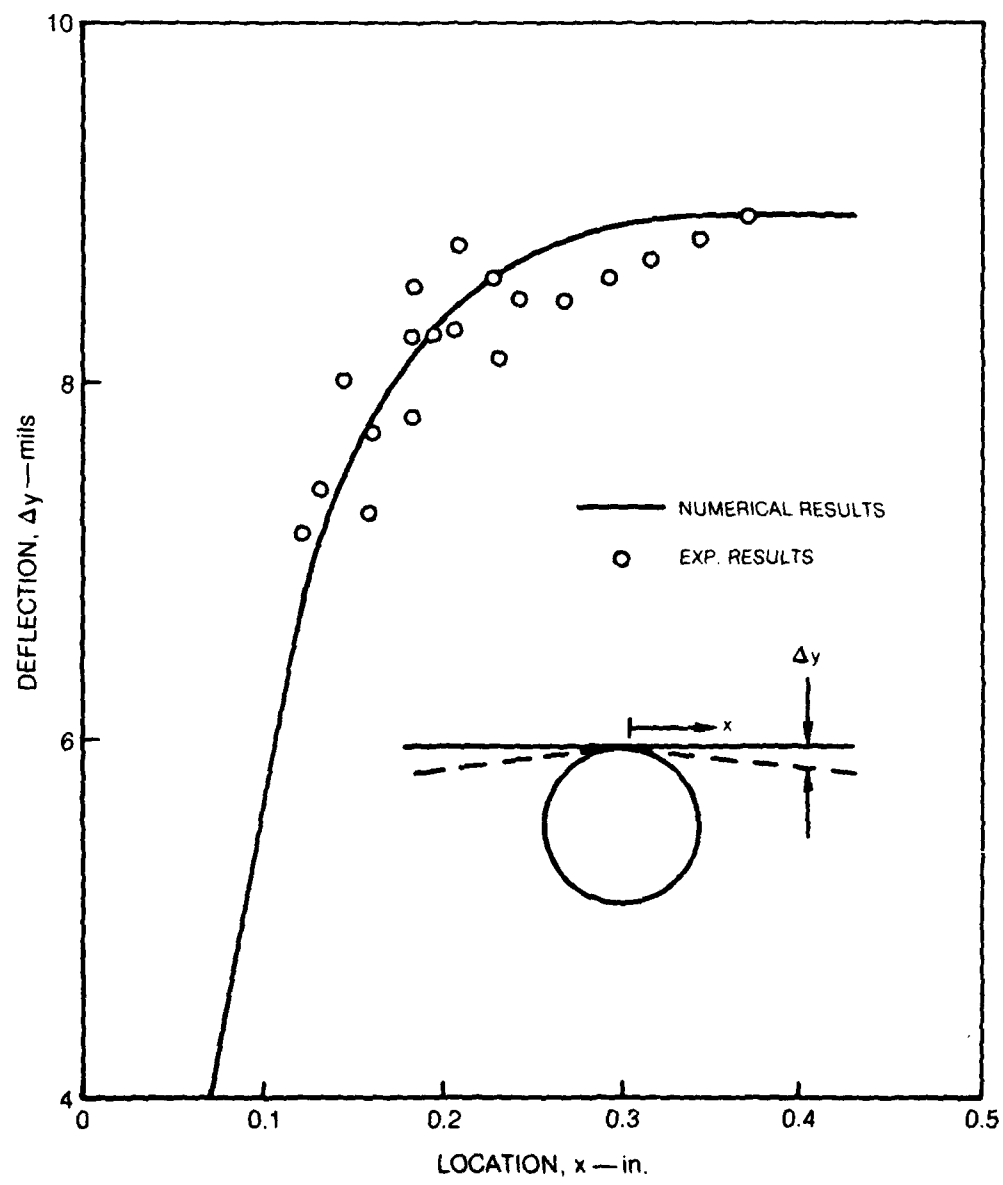
PREDICTED NICKEL FOIL DISPLACEMENT FOR VERIFICATION EXPERIMENT



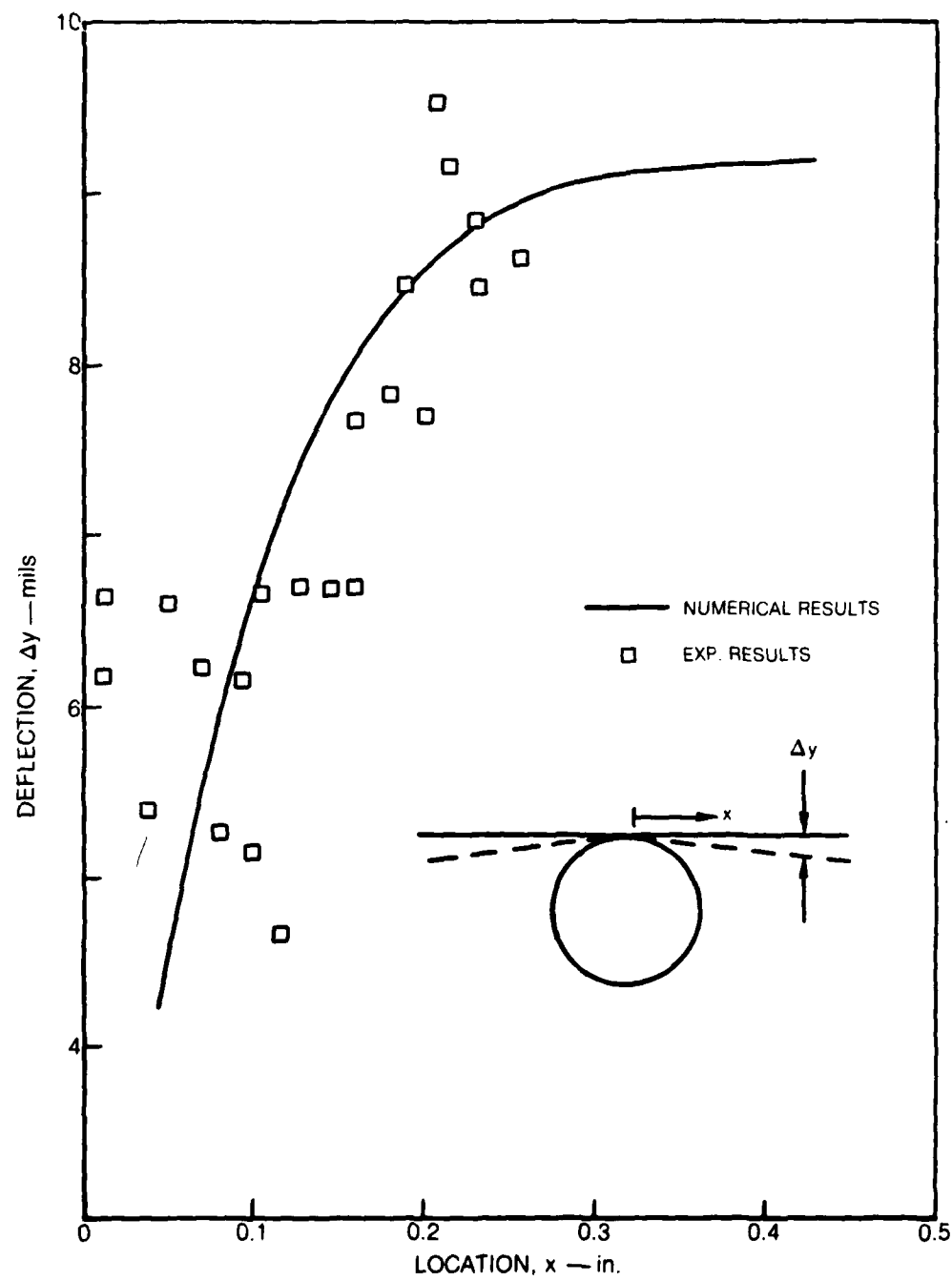
80-06-18-4

**TYPICAL CONFIGURATION OF VERIFICATION EXPERIMENT**

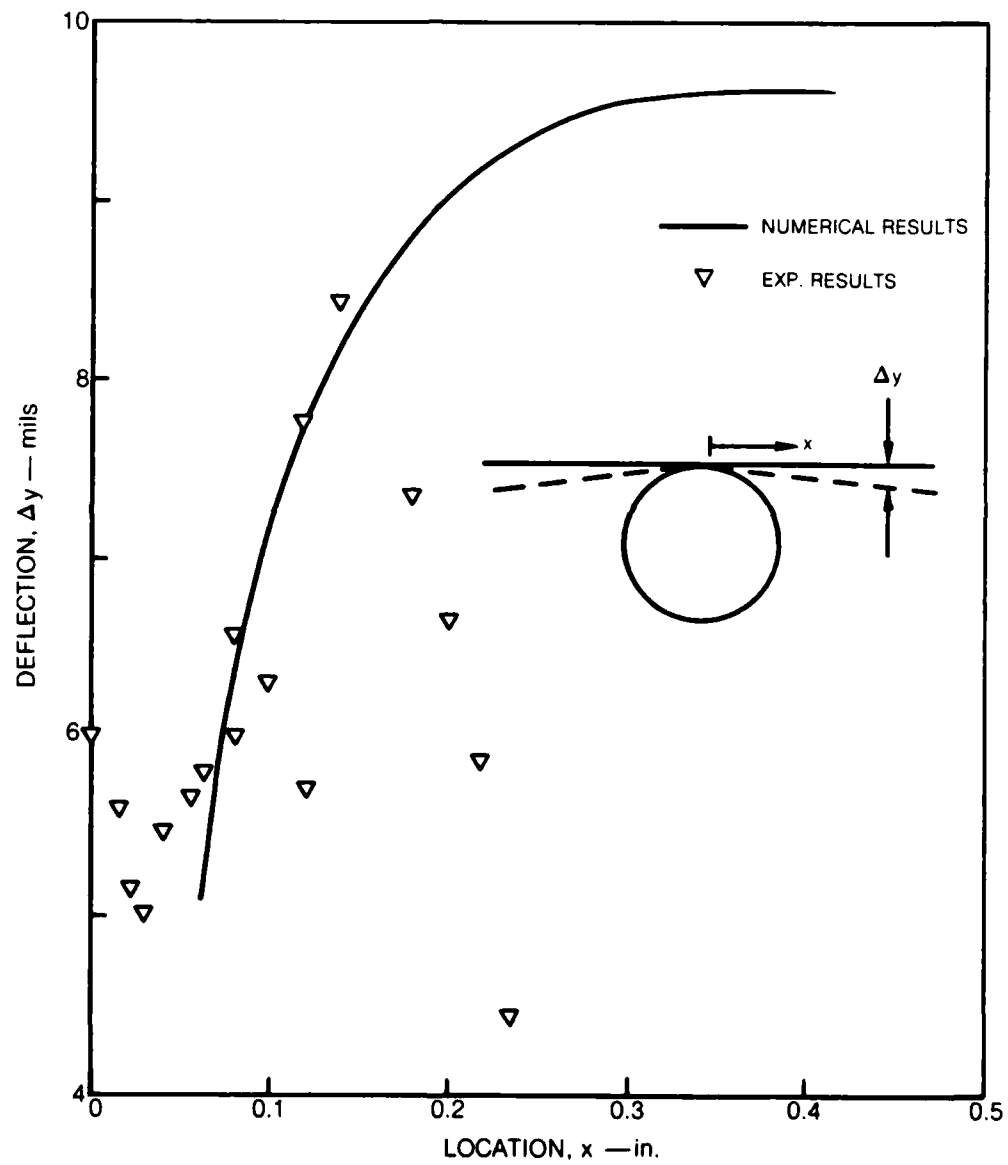
## RESULTS FOR VERIFICATION EXPERIMENT NO. 2



## RESULTS FOR VERIFICATION EXPERIMENT NO. 3



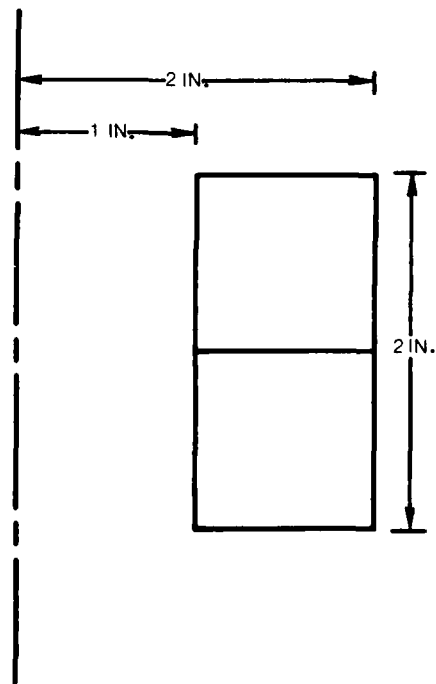
## RESULTS FOR VERIFICATION EXPERIMENT NO. 4



R80-944374-13

FIG. 47

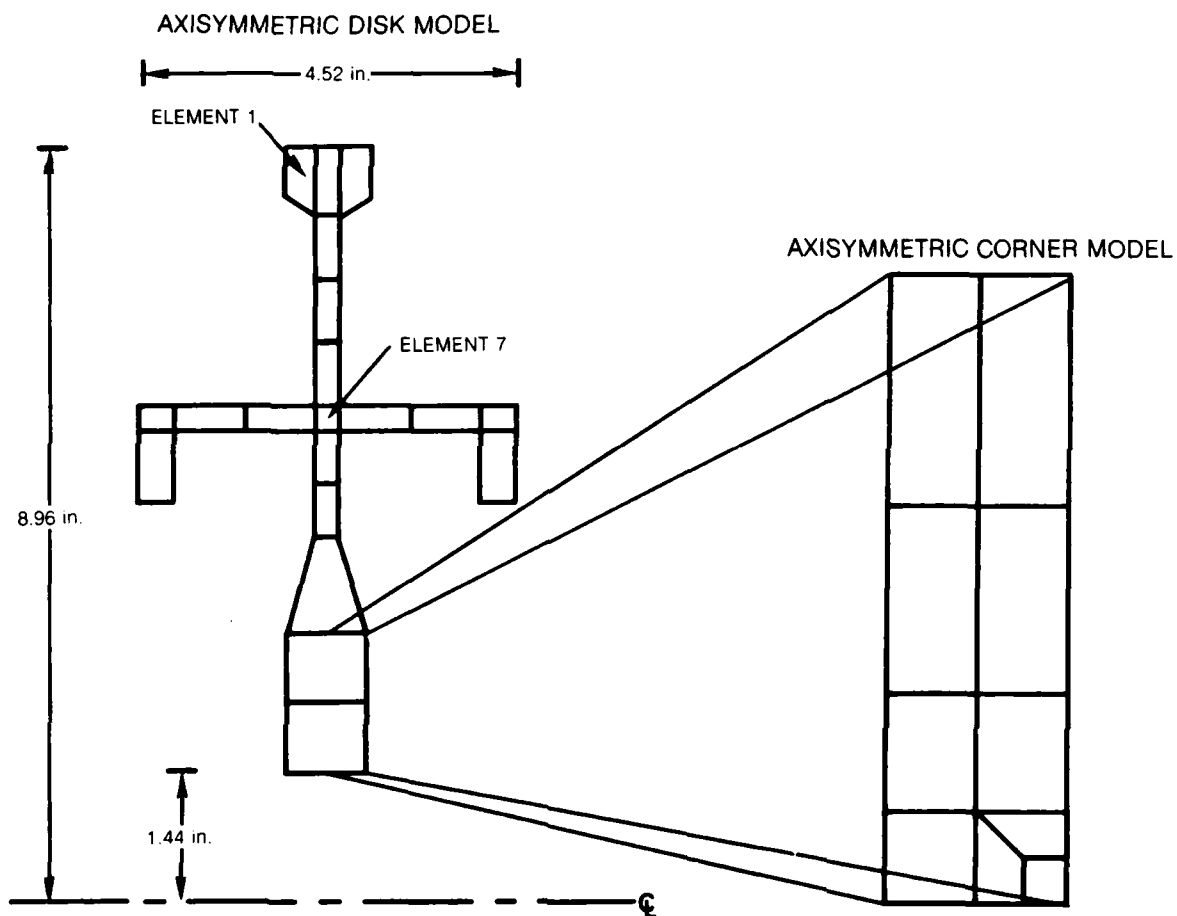
**PARAMETRIC STUDY FINITE ELEMENT MODEL**



R80-944374-13

FIG. 48

### DISK AND CORNER FINITE ELEMENT MODELS

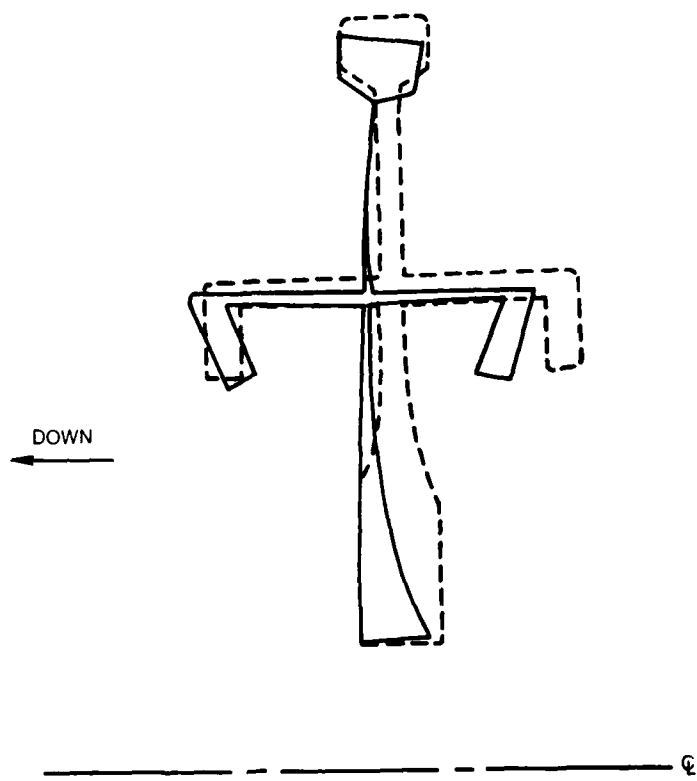


R80-944374-13

FIG. 49

**DEFORMED SHAPE OF F100 11th STAGE COMPRESSOR DISK**

— - - ORIGINAL SHAPE  
— MAGNIFIED DEFORMED SHAPE

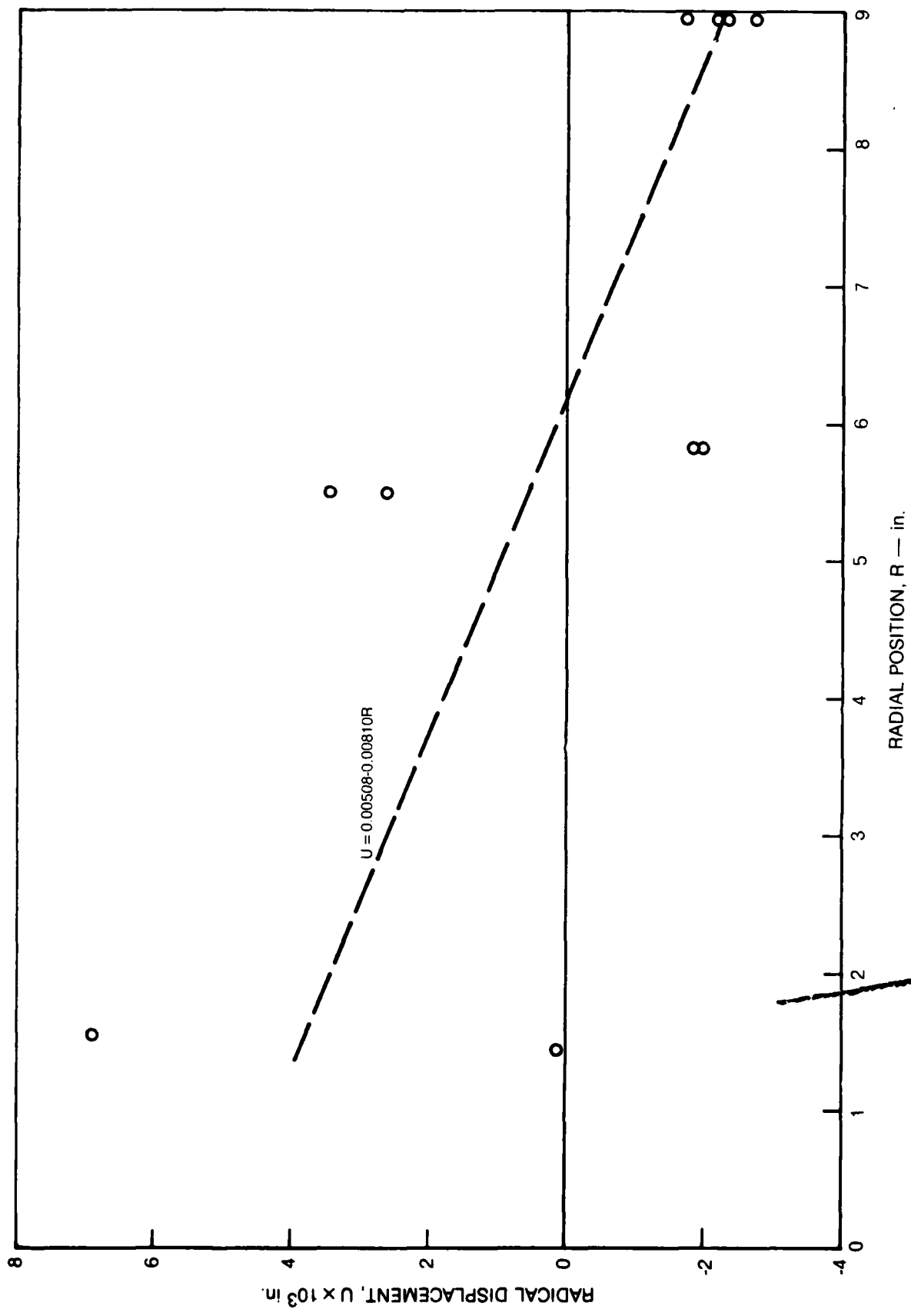


80-6-153-1

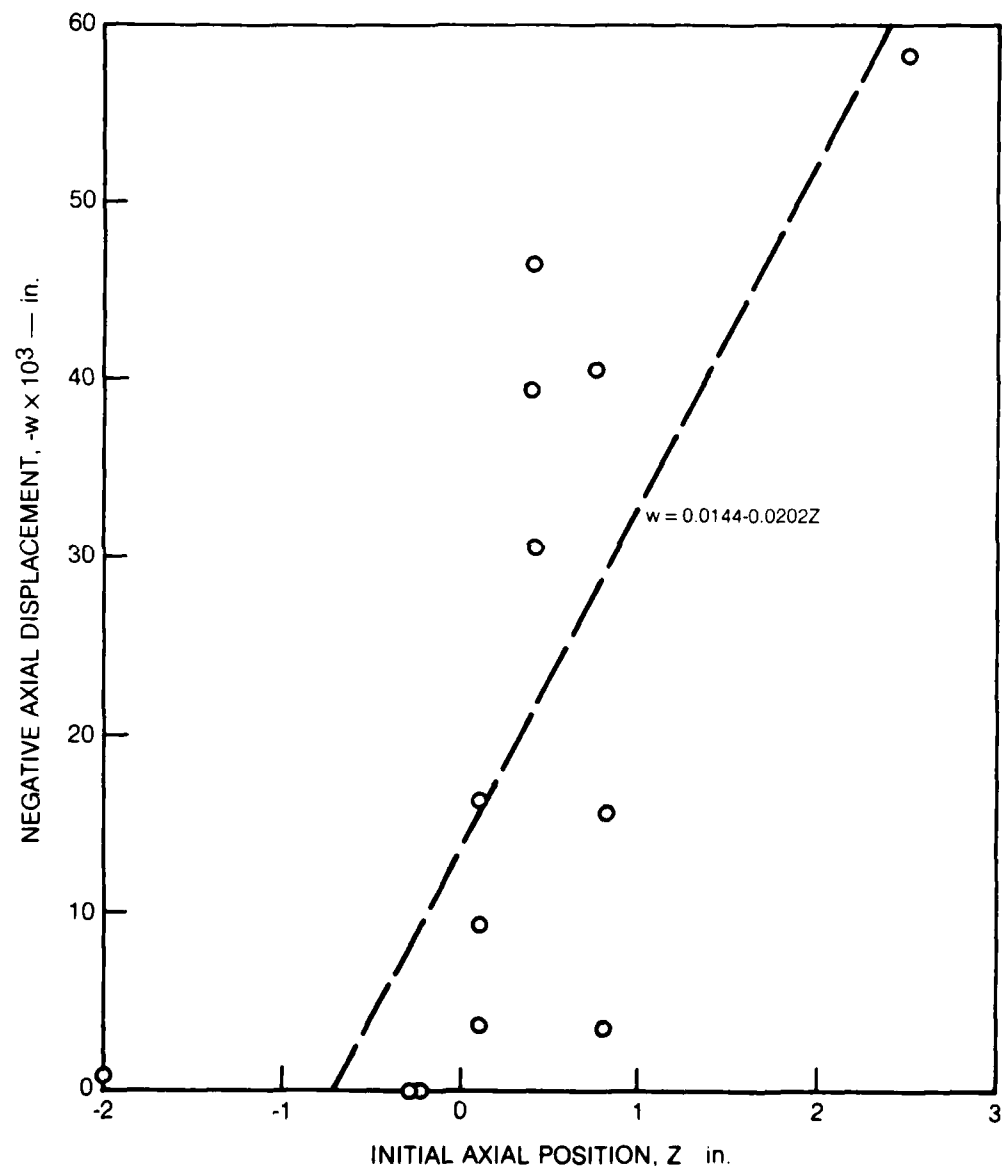
R80-944374-13

FIG. 50

RADIAL DISPLACEMENTS ON AXIAL SURFACES



80-6-153-2

**AXIAL DISPLACEMENTS ON RADIAL SURFACES**

R80-944374-13

DISTRIBUTION LIST

Director of Aerospace Sciences  
Air Force Office of Scientific Research  
United States Air Force  
Bolling Air Force Base  
Washington, D.C. 20332  
Attention: Lt. Co. J. D. Morgan III  
AFOSR/NA

(16 copies of Enclosure)

Dr. R. Dreschfield  
NASA Lewis Research Center  
21000 Brookpark Road  
Cleveland, Ohio 44135

(1 copy Enclosure)

Dr. H. Geigel  
Mail Stop AFWAL/LLM  
WPAFB, Ohio 45433

(1 copy Enclosure)

Dr. L. Berke  
NASA Lewis Research Center  
21000 Brookpark Road  
Cleveland, Ohio 44135

(1 copy Enclosure)